UNIVERSIDAD DE CHILE
FACULTAD DE CIENCIAS FÍSICAS Y MATEMÁTICAS
DEPARTAMENTO DE ASTRONOMÍA

PHYSICAL CONDITIONS AND KINEMATICS IN PROTOPLANETARY DISKS THROUGH LINE EMISSION

TESIS PARA OPTAR AL GRADO DE MAGÍSTER EN CIENCIAS, MENCIÓN ASTRONOMÍA

FELIPE MAURICIO ALARCÓN PEÑA

PROFESOR GUÍA:
SIMÓN CASASSUS MONTERO

PROFESOR CO-GUÍA:
SEBASTIÁN PÉREZ MÁRQUEZ

MIEMBROS DE LA COMISIÓN:
WLADIMIR LYRA
LAURA PÉREZ MUÑOZ

Este trabajo ha sido parcialmente financiado por Beca Magíster Nacional CONICYT, Millenium Nucleus "Protoplanetary Disks in ALMA Early Science" y por el Departamento de Postgrado y Postítulo de la Vicerrectoría de Asuntos Académicos, Universidad de Chile.

SANTIAGO DE CHILE
2019

RESUMEN DE LA MEMORIA PARA OPTAR
AL TÍTULO DE MAGÍSTER EN CIENCIAS, MENCIÓN ASTRONOMÍA
POR: FELIPE MAURICIO ALARCÓN PEÑA
FECHA: 2019
PROF. GUÍA: SR. SIMÓN CASASSUS MONTERO

PHYSICAL CONDITIONS AND KINEMATICS IN PROTOPLANETARY DISKS THROUGH LINE EMISSION

Las Ciencias Planetarias están constantemente progresando. Las infraestructuras actuales han permitido el descubrimiento de exoplanetas y un estudio más detallado de los discos protoplanetarios, que es donde se piensa que los planetas se forman. Entre los trazadores más importantes de la evolución de discos protoplanetarios está la medición de condiciones físicas de los mismos. Esta tesis se enfoca en dos partes principales; la primera trata el diagnóstico de líneas de emisión en el gas; mientras que la segunda explora discos durante etapas más tempranas en la formación planetaria, pasando a través de estallidos de acreción.

En el Capítulo 2, describimos un diagnóstico de líneas de emisión que permite la medición de temperatura, el ensanchamiento turbulento y la densidad de columna(número de partículas por unidad superficial) en discos portoplanetarios. Testeamos nuestro diagnóstico de línea a través de un análisis detallado de simulaciones hidrodinámicas post-procesadas de un disco protoplanetario con un planeta gigante incrustado. Nuestro diagnóstico podría potencialmente detectar huellas cinemáticas en la emisión de línea producida por interacciones planeta-disco, tales como los vórtices de onda Rossby asociados con formación de planetas gigantes. Pudimos concluir que nuestro diagnóstico de líneas de emisión mide una huella cinemática en el disco, aunque bastante pequeña. Cuando el diagnóstico de emisión de línea es aplicado a las simulaciones hidrodinámicas, la velocidad turbulenta medida muestra un pequeño incremento para transiciones moleculares ópticamente gruesas en la ubicación del vórtice y en la órbita del planeta.

En el Capítulo 3, exploramos un clase intrigante de objetos circumestelares, objetos FU Orionis. Objetos FU Ori se caracterizan por tener estallidos con altas tasas de acreción. Ellos pueden resolver el problema de baja luminosidad en la formación de estrellas de baja masa. Además se cree que las estrellas de baja masas pasan a través de este fenómeno más de una vez durante su formación. El Capítulo 3 aborda cómo los estallidos de acreción cambian la estructura radial del disco circumestelar en V883 Ori, un objeto FU Ori. Con nuestro acercamiento, medimos su temperatura y lo rápido que acreta. Usamos un algoritmo autoiterativo que recibe el perfil radial de una fuente circumestelar y retorna su forma y cuánto está acreatando, separando régimenes ópticamente delgados y gruesos. De nuestro análisis de V883 Ori, encontramos que los mecanismos de calentamiento en discos pasivos no reproducen el perfil termal inclinado de V883 Ori dentro de las treinta UA más cercanas a la estrella. Por lo tanto, concluimos que la disipación viscosa provee la cantidad de energía suplementaria necesaria para generar el perfil de emisión observado en V883 Ori.

Abstract

Planetary Sciences are constantly progressing. Current facilities have allowed the discovery of a considerable amount of exoplanets and a more detailed study of protoplanetary disks, which is where planets are thought to form. Among the important tracers of disk evolution is the measurement of physical properties of these protoplanetary disks. This thesis focuses in two main parts; the first one in the diagnostic of gas line emission; while the second explores disks during even earlier stages of planet formation going through outbursts of accretion.

In Chapter 2, we describe a line emission diagnostic that allows the measurement of temperature, turbulent broadening and the column density (particle number per unit surface) in protoplanetary disks. We test our line emission diagnostic through detailed analysis on post processed hydrodynamical simulations of a protoplanetary disk with an embedded giant planet. Our diagnostic could potentially allow the detection of kinematical signatures in line emission of planet-disk interactions, such as the Rossby wave (RWI) vortices associated with giant planet formation. We could conclude that our line emission diagnostic measures a kinematical signature in the disk, although very small. When the line emission diagnostic is applied to the hydrodynamical simulations, the measured turbulent velocity shows a small enhancement for optically thick molecular transitions at the location of the vortex.

In Chapter 3, we explored an intriguing class of circumstellar objects, FU Orionis objects. FU Ori objects have outbursts with high accretion rates. They could solve the low luminosity problem in the formation of low mass stars. It is believed that low mass stars go through this phenomenon more than one time during their formation. Chapter 3 addresses how accretion outbursts shape the radial structure of the circumstellar disk in V883 Ori, a FU Ori object. With our approach, we measure its temperature and how fast it accretes. We use a self-iterative algorithm that takes the radial profile of a circumstellar source and returns its shape and how much it is accreting, separating optically thin with optically thick regimes. From our analysis of V883 Ori, we find that passive disk heating mechanisms do not reproduce the steep thermal profile of V883 Ori within the inner 30 AUs. Thus, we conclude that viscous dissipation provides the supplemental amount of energy necessary to generate the emission profile observed in V883 Ori.

"We are all in the gutter, but some of us are looking at the stars."
Oscar Wilde

Agradecimientos

First of all, I must thank Simón Casassus and Sebastián Pérez, my two advisors. They have made me pushed my own limits in my pursue of science and astronomy. They have always been a support during this journey. I have always been amazed about their curiosity and passion for astronomy. I am also very grateful to the people I met at CSUN and JPL, particularly Wladimir Lyra who warmly received me at the US during my internship there. I have learnt a lot from all of them, not just about science, but about this track that I want to follow. They have made science enjoyable.

Me gustaría también agradecer a todas las personas que me han acompañado de alguna manera durante este último par de años, sin ellos, ésto no hubiera sido tan divertido como lo ha sido. A mis compañeros del postgrado, sobretodo a la gente de las mazmorras, por los almuerzos y la cotidiana entretención en Calán, los nombraría, pero son muchos, cada uno se ha ganado un espacio en mi corazón. A mis amigos de siempre a Seba, Peter, Gato, Matías por el apañe y las numerosas experiencias durante nuestra vida universitaria. No puedo no mencionar a mi amigo y odontólogo favorito Ivar, gracias por tanto :).

A la profesora María Angélica López, quien me introduje al mundo de la astronomía cuando tenía 16 años. Un lema que siempre llevaré conmigo, "Labor Omnia Vincit".

Por último quisiera agradecer a mi familia, tanto aquellos que están como los que no, mis hermanos, mis tíos, mis padres y abuelos. Desde que era pequeño, ellos siempre han sido mi principal motivación para perseguir mis sueños. Particularmente quiero agradecer a mi sobrina Carolina por alegrarme muchas tardes a veces solo con un abrazo y una sonrisa, también a mi papá, quien ha sido el motor de mi perseverancia, a lo largo de toda mi vida.

Contents

List of Tables

Chapter 1

Introduction

1.1 Current Context

After more than two thousands years of the first model of the Solar System, the knowledge known to Western science about the components of the Solar System and the Universe have made scientists reconsider previous theories. The different exoplanetary systems so far suggest that the Solar System is rather a particular system than a general rule [Winn and Fabrycky, 2015, Udry and Santos, 2007]. In that context the study of protoplanetary disks and in particular, their physical conditions contributes to a more general knowledge about the phenomenon.

So far, there has been more than 3869 exoplanets confirmed discoveries (29-10-2018). Studying these exoplanetary systems is how astronomers are able to do statistics about planetary formation outcomes. Previous studies and theories were mainly based only on the Solar System, because of that, there was a bias present. Ongoing research about exoplanetary architecture and configuration shows that there is a great amount of diverse possible configurations. There have been detections of exoplanetary systems with compact distributions. More than six planets in the same system at distances closer than the orbit of Venus, being Trappist one of them (Luger et al. [2017]), or giant planets ten times bigger than Jupiter that are very close o very far from their star. To understand all of these possible outcomes it is necessary to understand their origins and how they affected their current architecture. In other words, the study of circumstellar and protoplanetary disks have become important, giving their role in the planet formation process.

1.1.1 Observational Facilities Breakthroughs

Planet formation and the architecture of exoplanetary systems is an evolution of different stages. The different stages need to be studied at as many different wavelengths or bands as possible. Each one of them provides us different insights on the entire process.

Among the ground based telescope, facilities such as: the the Atacama Desert like the Atacama Large Millimeter and sub-millimeter Array (ALMA) and the Very Large Telescope (VLT) among many others, have allowed to push the frontier of planetary sciences and astronomy to unknown limits. The first observations using ALMA, with 16 out of 66 antennas, already showed interesting features in protoplanetary disks that have not been observed before. The image of HL Tau [ALMA Partnership et al., 2015] was the first protoplanetary disk observed with ALMA at such detail, showing multiple rings and gaps. A lot of different features present in protoplanetary disks could be observed and studied with the current facilities. Features such as: spirals, gaps, rings or dust traps. Now, at almost full capacity, ALMA probably have already been able to detect protoplanets (planets starting to form). Despite that its main focus has been the study of disks at an intermediate stage in the planet formation process (Class II sources), it also has been helpful in the study of disks at early stages, detecting snow lines in Class I objects (younger than transition disks). It will also help to study other important condition such as chemical abundances, gas surface profiles or disk masses. The early stages in planet formation will be much better constrained than they were before. In the optical and near infrared(NIR) part pf the spectrum, the VLT with its instrument SPHERE has been able to imagine planets inside the gap of protoplanetary disks [Keppler et al., 2018]

Spatial telescopes and satellites have also contributed to the planetary science community. The Kepler spacecraft only has discovered more than 2000 exoplanets using transits (Borucki et al. [2010], Howell et al. [2014], Lissauer et al. [2011], Batalha et al. [2013]). TESS [Ricker et al., 2015], Kepler's successor, with higher sensitivity will be able to detect planet around brighter stars. It already has its first Super Earth candidate [Huang et al., 2018]. Additionally, over 900 exoplanets have been found using other exoplanet detection techniques, such as: radial velocities, direct imaging, or microlensing. In the near future, James Webb Space Telescope(JWST) will also allow to characterize planet composition through the study of the spectroscopy of detected planets in the infrared part of the spectrum. JWST will be able to characterize atmospheres and detect planets by direct imaging, although the latter will not be its main focus. It will also contribute in the study of molecular clouds collapse and dust emission in debris disks at early and late stages of planet formation respectively.

1.2 Star Formation Stages

1.2.1 Young Stellar Objects and Circumstellar Disks

Stars are formed in relatively cold gaseous molecular clouds. The molecular clouds, that extent from tens to usually hundreds of AUs, collapse into dense cores because of gravitational inhomogeneities. At some point during the collapse, the dense core will begin nuclear fusion, becoming a protostar. The fast accretion rate of material onto the core is very inefficient transporting angular momentum outwards, so the material begins to rotate faster, forming a disk. There are some mechanisms that allow angular momentum transport outside the cloud; however, they are not efficient enough. After some time (< 1 Myr), the gas surrounding the protostar forms the circumstellar or protoplanetary disk. A protoplanetary disk is thought to

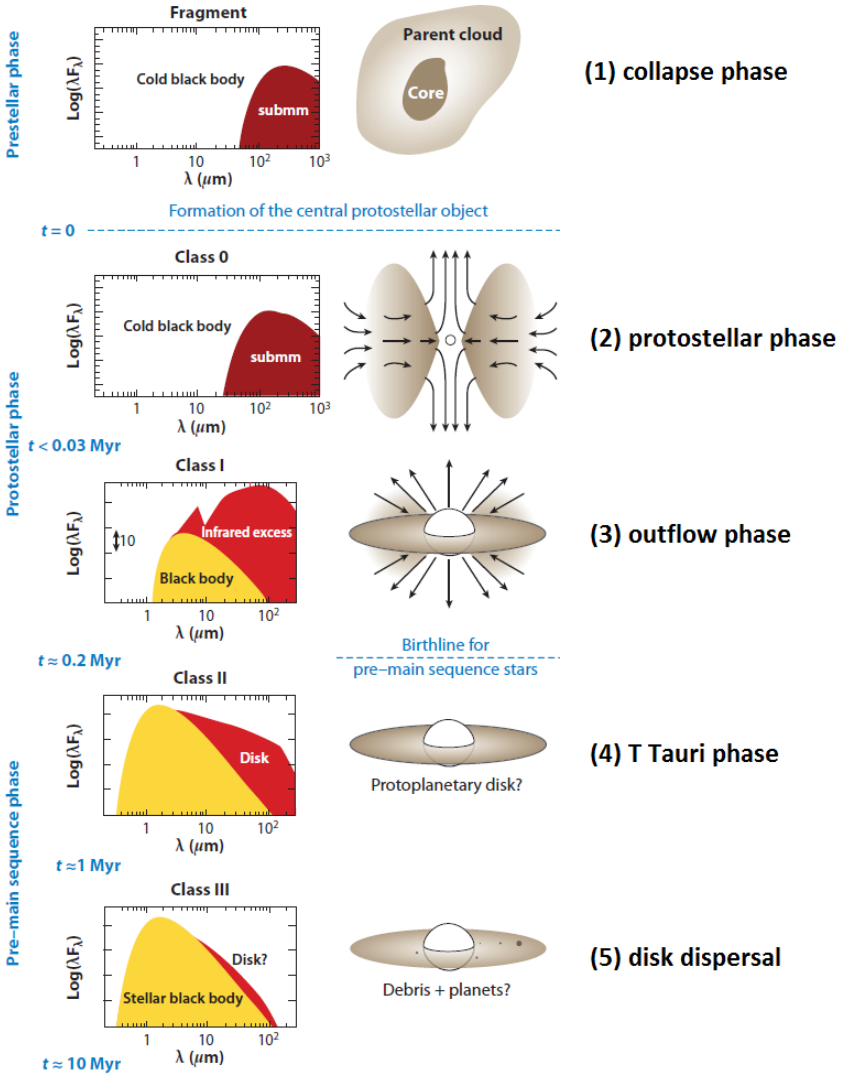

Figure 1.1: Spectral Energy Distributions for Young Stellar Objects at different evolutionary phases from early to late stages [Dauphas and Chaussidon, 2011]. This thesis will focus in physical conditions of Class I and Class II sources.

be the birth place of planets. For a more detailed review about the evolution of protoplanetary disks refer to Williams and Cieza [2011].

Inflow and outflow of material are present in the core, allowing for some angular momentum transport in the disk. These Young Stellar Objects (YSOs) show evidence of accretion onto their core. YSOs are known to have an UV excess produced shock heating of the gas being accreted by the protostar onto hot spots. They also present infrared excess associated with hot dust located in the disk near the star. This luminosity is the one that is reprocessed in the disk, the irradiation heating term.

To identify and classify the different evolution stages of protoplanetary disk, Lada [1987] made an spectral classification of YSOs according to its infrared spectral index,

$$\alpha_{\mathrm{IR}} = \frac{\mathrm{d}\log \nu F_\nu}{\mathrm{d}\log \nu} = \frac{\mathrm{d}\log \lambda F_\lambda}{\mathrm{d}\log \lambda}. \tag{1.1}$$

The α spectral index is usually calculated between 2 μm and 25 μm wavelengths. This first classification created three classes, I-II-III, all of them that fit into the collapsing and rotating core model ([Adams et al., 1987]).

After a few years of the classification, it had a refinement, made by Greene et al. [1994]. The change consisted in specify differences for sources between Class I and II. There was also another addition. Andre et al. [2000] included an earlier Class 0, that did not belong to any of the other previous classification.

Another classification was done based on the accretion state of the protostar according to their optical phase. In this classification there are: Classical T Tauri stars (optical visible pre-main sequence stars) that are associated with Class II YSOs; weak-lined T Tauri star(WTTS), that are rather associated with the Class III YSOs of the previous definition. The former type of protostar has strong Hα and UV emission, tracers of accretion, while WTTS has almost not evidence of it.

Among the different stages in the star formation sequence, planets are believed to form during the first 5-10 Myr. They are conform by the material surrounding the protostar, i.e., the gas that is still present in the circumstellar disk, before it has all been accreted or dissipated by the disk-star system.

Figure 1.1 shows the stages expected for the protoplanetary disk evolution during the star formation process. It describes the different Classes and stages for star formation evolutionary track as follows:

1. **Molecular Cloud Collapse(Class 0)**

   Molecular clouds are the initial stage necessary for planet formation. For this type of source, the Spectral Energy Distribution (SED) peaks in the far-IR or at the millimeter part of the spectrum ($\lambda \sim 100$ μm) and it has no flux emission in the Near-IR(NIR).

2. **Class I Objects**

   Class I objects have a flat or rising SED into the mid-IR. The growing in the SED profile

means that $\alpha_{\rm IR} < 0$. During this stage of the star formation, the protostar is embedded in a surrounding envelope of gas that it is being accreted, and the circumstellar disk has already formed.

3. **Class II Objects and Transitions Disks**

   Class II sources are also called Classical T Tauri stars and they have a falling SED into the mid-IR ($-1.5 < \alpha_{\rm IR} < 0$). During this epoch is when most of planet formation processes take place. Some Class II objects show giant gaps in the gas density and dust cavities also. Additionally, during this stage is possible to observe spiral arms and other important asymmetries in the disk structure. Disks that show gaps and cavities are often called *transition disks*. Class II objects, and particularly transition disks have received special attention by the astronomical community. It is believed that during this is the stage when planets are forming. The dynamical processes [Armitage, 2011b] and planets-disks interactions [Kley and Nelson, 2012] have been modeled to explain the physics in protoplanetary disk and their possible evolution path; The interaction with another bodies of their systems, is vital to understand the thoughts,

4. **Class III Objects**

   Class III objects are already pre-main sequence type of stars and are also labeled as WTTS. WTTS have little or almost no excess in the infrared, and they have not significant accretion anymore. Most of the gas has already been depleted by accretion or photoevaporation by the star. Some of them are also called debris disks. They are almost an exoplanetary system.

1.3 An Emphasis in Thermal Protoplanetary Disk Structure

When the thermal balance (heating and cooling) in a disk is dominated only by the irradiation from the star, disks are called *passive disks*. On the other hand, if there are other significant heating or cooling sources such as an important dissipation of gravitational energy, we call them *active disks*, e.g., accretion disks. For a disk to be active the other sources of disk heating have to be at least comparable to the potential energy of the system. An estimated accretion rate at which the gravitational energy release is comparable to the disk reprocessing of the star's luminosity is (see [Armitage, 2009] for more details):

$$\frac{1}{4}L_{\odot} = \frac{G\dot{M}M_{*}}{2R_{*}}, \tag{1.2}$$

where the critical mass accretion rate is close to $\dot{M} \approx 3 \cdot 10^{-8}$ $\mathrm{M_{\odot}\ yr^{-1}}$. It is worth to notice that it is assumed that the disk reprocesses one quarter of the star's luminosity). This critical accretion rate is just in the range of the measured accretion rate for T Tauri stars (Gullbring et al. [1998]). The range spans one order of magnitude above and two below this critical accretion rate.

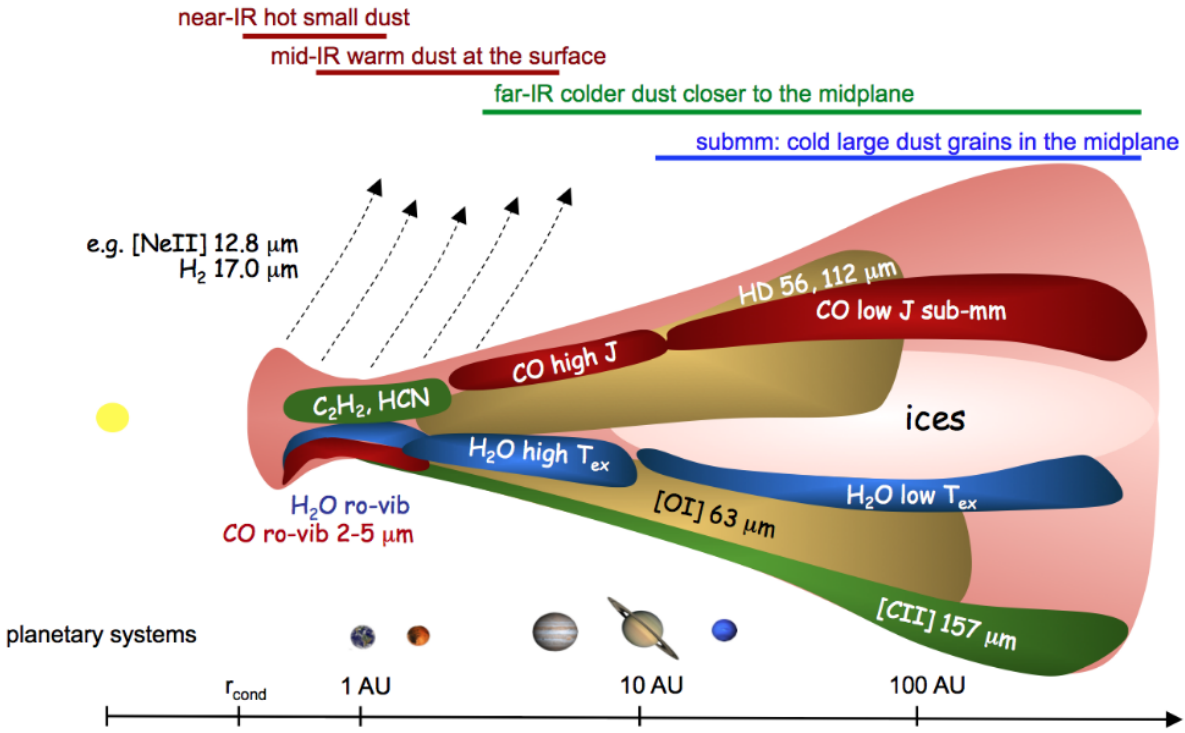

Figure 1.2: Emission origin for different wavelengths and molecular transitions in a protoplanetary disks, and their intrinsic properties [Kamp, Inga, 2015].

1.3.1 Passive Disks

Most of the luminosity of passive disk comes from reprocessed starlight by the disk. If we consider an optically thick, the surface layers are the ones more exposed to starlight, therefore, they are hotter than the midplane, which is usually colder. t o understand the radial thermal profile of a passive disk, we need previous knowledge about the physics and the structure of a protoplanetary disk. The vertical structure is given by hydrostatic equilibrium between the pressure gradient and the gravitational force, i.e.,

$$\frac{\mathrm{d}P}{\mathrm{d}z} = -\rho g_z, \tag{1.3}$$

with ρ the gas density and g_z the vertical component of the gravity. If we consider a parcel of gas at a distance d from the star and at a height z from the disk midplane, the vertical component of the gravity would be $g_z = \frac{GM_*}{\mathrm{d}^2}\sin\theta$. If we add the thin disk approximation ($z << \mathrm{d}$), we have that $g_z \approx \Omega^2 z$, with Ω the Keplerian angular velocity. Moreover, it is fair to consider vertical isothermal conditions for a passive disk in steady state. Under vertical isothermal conditions, the equation of state becomes:

$$P = \rho c_s^2, \tag{1.4}$$

with c_s the local sound speed. Using the relation between ρ and P from equation (1.4) in equation (1.3), we obtain the following relation:

$$c_s^2 \frac{\mathrm{d}p}{\mathrm{d}z} = -\Omega^2 \rho z. \tag{1.5}$$

The formal solution of equation (1.5) results in a gaussian profile for the gas density in the vertical direction. This gaussian solution is also centered at the midplane, $\rho = \rho_0 \mathrm{e}^{-z^2/2h^2}$, where ρ_0 is the midplane density and h is the scale height. The midplane density ρ_0 and the scale height h are given by

$$h = \frac{c_s}{\Omega}, \tag{1.6}$$

and

$$\rho_0 = \frac{1}{\sqrt{2\pi}} \frac{\Sigma}{h}, \tag{1.7}$$

with Σ the gas surface density.

The aspect ratio, h/r, describes the shape of the disk. Equation (1.6) shows that the sound speed is correlated with the scale height, and the temperature as well; thus, if the disk is *flared* ($\mathrm{d}h/\mathrm{d}r > 1$), the thermal radial profile would be different of the one of a flat disk. This difference in the thermal radial profile is produced because the aspect ratio increases with distance. In other words, at any distance from the star, the surface point of a flared disk disk is exposed to the stellar irradiation.

There are several papers that describe the radial temperature derivation for the thermal profile of passive disks (see Adams and Shu [1986], Kenyon and Hartmann [1987] or Chiang and Goldreich [1997b]). They show that flared, warped and flat disks have different temperature profiles, meaning that the shape is an important feature to determine the temperature profile in a disk.

We show a more formal derivation of the thermal profile for one of the simplest shapes for a protoplanetary disk. Following the treatment in Armitage [2009], we consider a razor-thin disk and a spherical star of radius R_*, which has a constant brightness I_*. The flux passing through a surface element would be

$$F = \int I_* \sin\theta \cos\phi \mathrm{d}\Omega, \tag{1.8}$$

where $\mathrm{d}\Omega$ is the element of solid angle, θ and ϕ are the usual angles of the spherical coordinates. We consider the main axis of the reference system pointing to the center of the star. If we observe only one half of the disk, for example the top part, the incoming flux would be

$$F = I_* \int_{-\pi/2}^{\pi/2} \cos\phi \mathrm{d}\phi \int_0^{\sin^{-1}(R_*/r)} \sin^2\theta \mathrm{d}\theta. \tag{1.9}$$

We assume that the received flux F is equal to the irradiation of one side of the disk at an effective temperature $T_{\rm disk}$, $F_{\rm disk} = \sigma_{\rm sb} T_{\rm disk}^4$. Then, we evaluate the integral in equation (1.9) with $I_* = (1/\pi)\sigma_{\rm sb} T_*^4$. The radial profile obtained from this relation is:

$$\left(\frac{T_{\rm disk}}{T_*}\right)^4 = \frac{1}{\pi}\Big[\sin^{-1}\left(\frac{R_*}{r}\right) - \left(\frac{R_*}{r}\right)\sqrt{1-\left(\frac{R_*}{r}\right)^2}\Big]. \tag{1.10}$$

We integrate the surface received from the disk, $F_{\rm disk}$, at each surface area, $2\pi r \mathrm{d}r$, and multiplied by the two sides of the disk to get the total disk luminosity:

$$L_{\rm disk} = 2\int_{R_*}^{\infty} 2\pi r \sigma T_{\rm disk}^4 \mathrm{d}r = \frac{1}{4} L_*, \tag{1.11}$$

which illustrates that the disk reprocesses only a quarter of the star luminosity. Additionally, if we do a Taylor expansion for the outer parts of the disk with the right terms of equation (1.10), the temperature has the following profile:

$$T_{\rm disk} \propto r^{-3/4}. \tag{1.12}$$

This profile corresponds to the profile of a flat and thin disk. For flared cases, given that the disk keeps being exposed to the stellar irradiation, their radial dependence should be higher than $-3/4$, i.e, they have a flatter thermal profile.

1.3.2 Active Disks

In an active disk, the same heat sources that are present in passive disks must be considered as well. However, these heat sources have not the predominant role in the heating and cooling mechanisms of the disk. For accretion disks in particular, one heat source that becomes important is the accretional or viscous heating. Viscous heating is associated with the gas shearing in the disk produced mainly by gas accretion. When accretion is high enough, viscous heating could be dominant over the other heat sources, becoming the principal heat source in the disk. Having said that, one of the main differences between the thermal structure of active and passive heat sources is their radial dependence. In other words, passive and active heating sources affect the disk in different ways. The stellar irradiation has a slower decrement with distance than accretional heating, so, for an active disk, the star is the responsible of the heating of the outer parts, while the accretional heating heats the inner parts.

Viscous heating depends primarily in the motion of the particles, the viscosity of the gas and its density. When an inflow of material is present, the gas has a negative drift velocity v_R,

meaning that it is being accreted onto the star. The accreted gas crosses through orbiting layers of gas that will produce a shear between them liberating energy and heating their surrounding. The inward radial velocity, v_r, mixed with the surface density, Σ, gives an expression for the mass accretion rate,

$$\dot{M} = -2\pi R \Sigma v_R. \tag{1.13}$$

The gas azimuthal velocity is close with the velocity of an object orbiting the central source (in this case the star), this means that it is nearly the Keplerian velocity, i.e.,

$$v_\phi = R\Omega_K(R) = \left(\frac{GM_*}{R}\right)^{1/2}, \tag{1.14}$$

where M_* is the mass of the star, G the gravitational constant and R the particle distance to the central source.

As has been said, the viscous dissipation per unit plane surface area, $D(R)$, is given by; the viscosity of the gas ν that quantifies the amount of shear between the particles; the gas surface density, Σ, which describes the amount of particles colliding; and the Keplerian angular velocity Ω_K. The viscous dissipation has the functional form

$$D(R) = \frac{9}{8}\nu\Sigma\frac{GM}{R^3} \tag{1.15}$$

1.4 This research

This work tries to recover the physical conditions at early and intermediate phases of protoplanetary disk evolution after the formation of the protostar. The first part details the development of a diagnostic that measures physical conditions in protoplanetary disks using line emission from molecular tracers. One of the main focuses in the planetary science community is the understanding of the planet formation process at its early stages. Physical conditions such as temperature or velocity are vital to constrain the pathways followed by planet formation process. These conditions also determine the possible outcomes for the final exoplanetary architecture.

The second part of this thesis focuses on the thermal profile of V883 Ori, a FU Ori object. ALMA observations of dust continuum were used to measure its brightness temperature radial profile. Furthermore, V883 Ori shows a steeper thermal profile at the inner AUs than the expected for a passive disk. Because of that, we can infer that it has additional heat sources. The measurement of this additional heat source may help to constrain some physical properties of the disk, such as the accretion rate and its morphology. Accretional heating is then included as an additional heat source in the radiative transfer of this object. Through modelling of the accretional heating and the brightness temperature measure from the observations, we recover the disk shape and its accretion rate. Our aim is try to understand the

underlying structure and the morphology that lead to the thermal profile observed in V883 Ori.

1.4.1 Diagnostic of Physical Conditions using Molecular Lines

One of the principal objectives in the study of protoplanetary disks is the detection of protoplanets. ALMA is at current date the best facility to do so, given its spatial resolution and spectral windows. ALMA allows astronomers to observe molecular lines inside disks, task that is not possible with other facilities or telescopes because either the star is too bright or the dust emission is too optically thick. The rotational energy transitions that are observable with ALMA at millimeter and sub-millimeter wavelengths make possible the study of disks at different depths tracing their vertical structure. Figures 1.2 and 1.3 sketch how different molecular lines trace distinct regions and layers in protoplanetary disks.

Studies of emission lines are done to measure the physical conditions at different regions in the disk, understanding its structure or its thermal and chemical evolution. The constraint of physical conditions determine how planets are formed and the future composition of planets [Kamp, Inga, 2015, Kamp et al., 2017]. Observing at the same lines of sight, it is possible to infer the relative abundances between different species and the underlying processes that produce some specific lines or the lack of them. The lines emitted or absorbed, their profile and other features contain information about the gas that is emitting it, such as: its velocity, its temperature and the total amount of material along the line of sight. These conditions are the baseline for core accretion models, protoplanetary disk evolution and planet formation theories. Furthermore, kinematic features in line emission have been recently used to test the presence of protoplanets disturbing the otherwise sub-Keplerian profile of the gas [Teague et al., 2018, Pérez et al., 2018b, Pinte et al., 2018b].

We have developed a line diagnostic that measures the physical conditions in the protoplanetary disk. Our main goal was to measure temperature, turbulence and column density along a certain direction of the molecular line emission. The diagnostic was designed to be applied in ALMA data of protoplanetary disks, but it certainly could be used for other purposes or type of sources.

1.4.2 Impact of Viscous Dissipation in the Structure of the FU Ori Source V883 Ori

Early in the planet formation process, some stars go through a very high accretion stage. These young stars with large optical outbursts are identified with the name of FU Orionis objects, named by the first source of its type [Herbig, 1977]. Figure 1.4 illustrates the inflows and outflows of material in a FU Ori object. They also have some particular spectroscopic features. FU Ori objects present a spectral type of late F or G supergiants at optical wavelengths, very blueshifted Balmer lines with broad absorption. On the contrary of their optical spectra, the infrared emission of this class of source is best fitted with K-M supergiant atmospheres. Their infrared spectra has strong CO absorption and water vapor bands in the

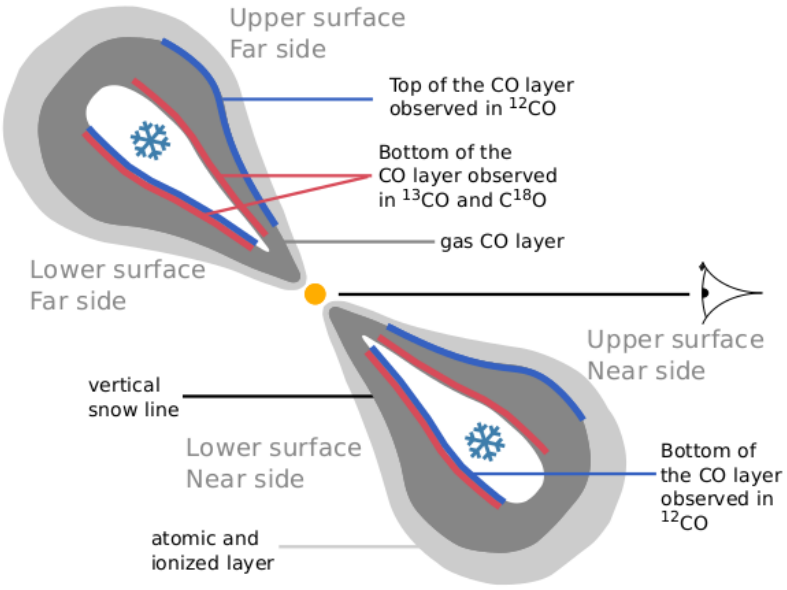

Figure 1.3: Different layers observed at the same spectral window with CO isotopologues. Each one of them traces a different depth (or height) inside the disk, allowing the study of its vertical structure [Pinte et al., 2018a]

.

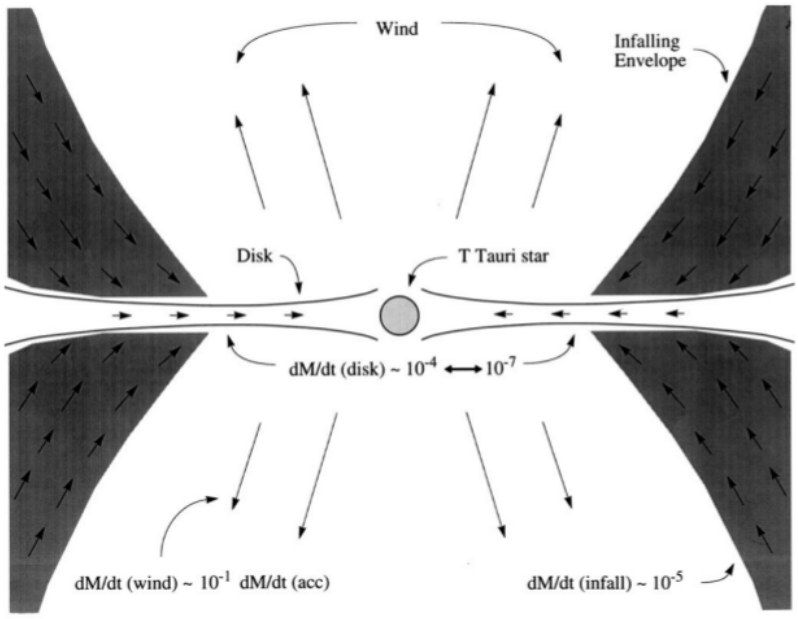

Figure 1.4: Sketch of a FU Ori object structure. It shows the characteristic inflow of material at the midplane and the winds at the envelope in a FU Ori object. Hartmann and Kenyon [1996]

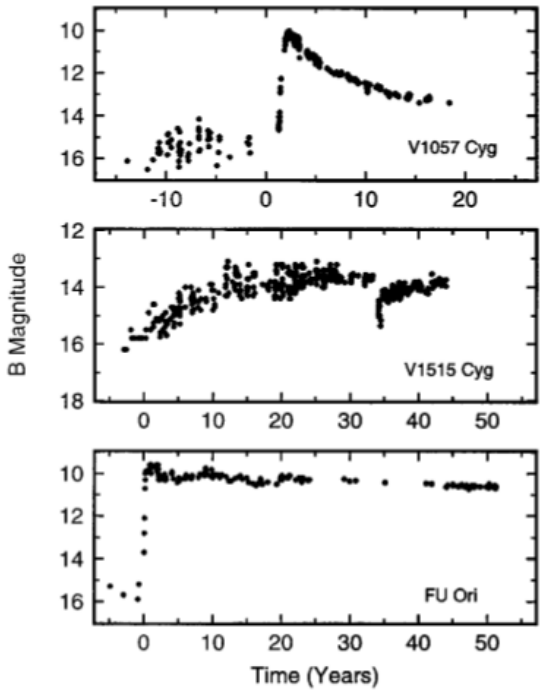

Figure 1.5: Example of light curves of FU Ori objects before and after the outburst of accretion. They increase their luminosity in two or more magnitudes.Hartmann and Kenyon [1996]

near infrared ($\sim 1 - 2\mu$m). So far, FU Oris are been modeled as a steady state accretion disk, what for most of the cases is a good approximation. It is believed that although this is a short stage, it is a repetitive and very common phenomenon in the formation of low mass stars [Hartmann and Kenyon, 1996].

Figure 1.5 show different examples of FU Ori objects. It is observed that during this outburst of accretion, the luminosity of the circumstellar disk could be amplified by one hundred or one thousand times the star's luminosity. This high accretion stage is key to explain the low luminosity problem Dunham and Vorobyov [2012]. The low luminosity problem is related to the low luminosity in low mass stars, meaning that their accretion rate is not high enough to reach their final masses [Evans et al., 2009]. So, there must be a shorter stage where more of the mass in the disks is accreted. Although, FU Ori outburst are short in star formation timescales, they may be a common stage in the low mass stars formation process.

When this transitory stage occurs, several conditions are changed. The disk structure changes abruptly, for example, there is evidence of wiggles in the radial profiles of the continuum emission in this class of sources [Sheehan and Eisner, 2018]. Winds, shock heating and viscous heating produce changes in the thermal structure and the disk shape. The condensation radius where volatiles transform into their solid form called ice lines are displaced because of that. Moreover, the chemistry and radiative processes in the disk are different from the stationary stages. The phase of some volatiles or dust grains quickly changes during short periods of time, so dust coagulation, fragmentation and thus planet formation are severely affected. Chemical reactions and abundance ratios are then modified during this stage [Molyarova et al., 2018].

Because the water snow lines are farther out in FU Ori objects, the study of dust populations and trapping at the frontier is more feasible. Several theories could be tested in FU Ori objects. For example, it is believed that drier planets may be formed inside the water snow line, where minerals were able to overcome bouncing barriers through their melting [Hubbard, 2017]. The study of these hotter sources represent a good starting point trying to understand the delivery of volatiles in planets and the condition needed for habitability.

To study the chemistry and dynamics in FU Ori objects, the effects of accretion must be included in the modeling. FU Ori systems have more emission at inner radius than passive disks with low accretion rates. The usual heating sources of a passive disk also affect a FU Ori, meaning irradiation heating and interstellar heating. However, the heating produced by the viscous shear of the gas is usually not included in the modeling of emission for specific sources, although it is a valid and studied heat source in accretion disks. [Frank et al., 2002, D'Alessio et al., 1998, Pringle, 1981]

We use a self-iterative method to model the disk shape and the additional amount of heat neceded to reach the thermal profiles observed for V883 Ori. We compared the thermal structure with and without the viscous dissipation produced by the accretion rate, showing that passive heating does not heat the disk enough to increase their dust emission and obtain such steep profiles as the one of V883 Ori at the inner fourty AUs.

Chapter 2

Line Diagnostic of Physical Conditions using gas emission.

Millimeter and sub-millimeter observations along with spectroscopy of protoplanetary disks have allowed the measurement of their physical conditions. Line emission of certain molecular tracers, such as CO, depends on a variety of different physical conditions of the gas; temperature, column density and velocity among others. These physical conditions are of great importance to study the evolutionary paths for planet formation and to constrain its effect on its host protoplanetary disk. Here, we present a model that fits line emission from molecular tracers and quantifies local physical conditions that would reproduce the line shape. We start by doing a benchmark using a controlled input of a fiducial disk. After that, we applied our line diagnostic to a 3D hydro-dynamical simulation with an embedded giant planet (1 M_J) on a protoplanetary disk for 500 orbits for a planet located at 100 AU from the central star. We test for kinematic signatures of structures launched via planet-disk interactions.

2.1 Introduction

During protoplanetary disk evolution, there are several stages, each one of them with characteristic features and spectra. Transition disks represent an intermediate stage in disk evolution which has received particular attention for its possible ling to giant planet formation process [Williams and Cieza, 2011]. This type of disk possesses a considerable amount of features containing the dynamical and kinematic history of the disk. A thorough description of protoplanetary disk evolution goes beyond the scope of the line diagnostic, for a deeper description of the steps in the protoplanetary disk track see Wyatt et al. [2015]. Most of the observational studies have been conducted with the Atacama Large Millimeter and sub-millimeter Array (ALMA).

With ALMA, more detailed and resolved observations of transition disks structures are now possible, both spatially and spectroscopically [Casassus, 2016, Perez et al., 2015b, Regály et al., 2012]. Thanks to that, different features in these disks have been observed and modeled

over the past years. To explain the origin of these features or the probable evolution of disks, a better understanding of their physical conditions is necessary, using theoretical models as well.

There are several approaches to disk modeling using theory. They intend to improve the understanding of the physical and chemical processes in the transition disk stage (see Haworth et al. [2016] and Armitage [2011]). One of particular interest to the scope of this chapter is the study of kinematic effects over the gas produced by planet-disk interactions [Rosotti et al., 2017]. Flaherty et al. [2018] for instance, they studied the amount of turbulence in a protoplanetary disk a found a certain type of correlation between temperature and turbulence. Nevertheless, the turbulence only reaches level usually lower than 10% of the local sound speed, so it is in the order of tens of meters per second. In another study, Dong et al. [2018] analyzed possible footprints of velocity dispersion inside gaps; however, they need very high sensitivity observations and they did not decouple the effect of thermal broadening to the dispersion time to be allowed to detect them.

Temperature is among the most important parameters to measure, given its importance in different processes for both chemistry and physics. There have been previous attempts done by Schwarz et al. [2016] and Teague et al. [2017] to measure the gas temperature at different regions and/or layers using CO isotopologues. Knowing the thermal structure, it is possible to constrain the snow lines locations and phase changing zones in the disk [Du et al., 2017]. Ice lines are linked with the stickiness of dust and their ability to coagulate into bigger grains. Snow lines of different volatiles are also important in the chemistry differentiation of disks. All of these physical parameters are important in several ways during the evolutionary tracks of protoplanetary disks. Gas composition and emission shape the dust evolution, the disk's shape and planet formation; hence the importance of their study.

Because of its characteristics, CO is one of the favorite lines to observe [Bruderer, 2013] in mm and sub-mm wavelengths. Besides that CO is an abundant molecule in the interstellar medium, it also possesses a multiplicity of vibrational transitions and isotopologues with different optical depths in the ALMA observability range. For example, Miotello et al. [2015, 2016, 2017] and Williams and McPartland [2016] have measured the available mass in protoplanetary disks with the measured CO flux. Perez et al. [2015a] and Yu et al. [2016] observed and analyzed the CO emission in protoplanetary disks, finding gas features that correlates with the continuum emission of the disk (mainly dust emission). Fedele et al. [2017] described the depth of CO isotopologues emission, showing that they trace different heights or layers in the disk, so there are precedents that a vertical study of the disk structure could be done using these isotopologues.

ALMA observations of dust and gas are useful to unravel the evolutionary paths of young planetary systems, but this has to be done with special caution. [Boehler et al., 2017] reported some issues to be considered in the measurement of the amount of gas with line emission. Usually, gas emission lines are separated from the continuum by subtracting an interpolated linear function of the dust emission for frequencies where there is not line present. In most of the cases, this method underestimates the gas emission because it only considers the gas emission above the continuum and not the continuum absorption. When the dust-to-gas

ratio is considerable(>0.1), like in high dust concentration scenarios such as dust traps, cautions should be taken to correctly measure the amount of gas. This absorption effect is more remarkable for optically thick gas tracers, when the dust emission is almost entirely depleted by the gas under the molecular line.

Here, we report a line diagnostic using uniform slab models for molecular line emission, particularly of CO isotopologues in transition disks at millimeter wavelenghts. Our model separates the kinematic broadening of the line into thermal effects and turbulent ones. We also measure the amount of excited column density; if we consider Local Thermodynamic Equilibrium (LTE) and the temperature measured from the fit, the net column density for that particular tracer can be recovered. Previous observational attempts to measure kinematic signatures through line emission did not considered the decoupling between thermal effects and turbulent ones, fitting the velocity dispersion as just one parameter. We also include the combination of different isotopologues at the same spectral window obtaining the vertical structure of the disk. This diagnostic can be used to study the abundance ratio between different species and the kinematic effects of protoplanets in their host disk, either vertically or radially in the disk plane. It also can be used to give details about the thermal structure and how it changes during the protoplanetary disk evolution. The inference of physical conditions and the model described here have been used for the recovery of physical parameters in other fields as well. For example, Peñaloza et al. [2017] did a similar work measuring physical conditions from line emission with a uniform slap approach but applied to molecular clouds instead.

The following chapter is structured as follow: Section 2.2 describes the model and parameters used as input for the hydrodynamical and radiative transfer models. In Section 2.3, the benchmark model of line emission and parameter measurement is detailed. Section 2.4 describes the results of the benchmark and compares the input parameters of the simulations and the parameters measured by the model. 2.5 summarizes the chapter.

2.2 Methodology

2.2.1 Hydrodynamics Simulations Setup

To test the modeling, we used the hydrodynamic simulations published in Pérez et al. [2018a]. These simulations were conducted using the open software Fargo3D [Benítez-Llambay and Masset, 2016] and are briefly described in this section. Figure 2.1 illustrates the results of the simulations for the density at the midplane, the velocity fields and the deviation respect to the expected sub-Keplerian profile.

The simulations were run using a spherical grid with a resolution (r, ϕ, θ) of $400 \times 600 \times 40$, where r is the radial coordinate, ϕ is the azimuthal component, and θ the colatitude angle measured from the zenith. The radial grid has a logarithmic spacing between 40 and 280 AU, while the angular coordinates spans linearly in the range $(0, 2\pi)$ for ϕ, and $(\frac{2\pi}{5}, \frac{9\pi}{10})$ for θ. The surface density was set with a standard power law that decays proportionally with

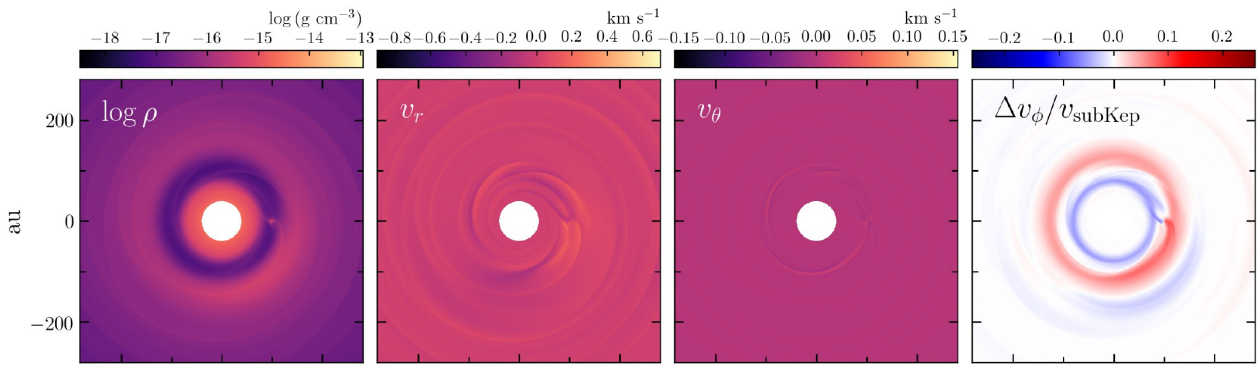

Figure 2.1: Hydrodynamical simulations done by Pérez et al. [2018a]. Left to Right: Logarithm of gas density, radial velocity, colatitude velocity and difference of azimuthal component with respect to the sub-Keplerian solution. The simulations show that there is a deviation of the order of $\approx$ 20 % of the keplerian profile in the planet's orbit and about a 10% under the dust trap due to the planet-disk interactions.

the inverse of the distance to the central star, i.e., $\Sigma \propto r^{-1}$. We used an alpha-viscosity prescription [Shakura and Sunyaev, 1973a] for the disk, where the α parameter is related to the efficiency in the transport of angular momentum. We set a conservative α parameter with a value of 10^{-4}. However, it is important to notice that such α value allows turbulence to prevail for a longer time than a higher one.

2.2.2 Radiative Transfer post-processing

Once the hydrodynamical simulations were finished, they were post-processed with the public radiative transfer code RADMC-3D [Dullemond et al., 2012]. RADMC-3D performs the radiative transfer in the disk through Monte Carlo predictions of the dust and gas emission using photons as random walkers to find thermal equilibrium. The setup for the radiative transfer was set taking a standard central star with a temperature T_*=7000 K. Given that we are looking for thermal or kinematic signatures rather than dust structures and the wavelength regime studied scattering is not as significant as gas absorption, we set photon scattering to zero. However, in others wavelength regimes, scattering should be considered in both, simulations and line emission modeling.

We set the gas temperature for the parametric disk with a standard power law :

$$T(r) = 70(\frac{r}{30})^{-0.5}\ K, \quad r > 30. \tag{2.1}$$

To measure the accuracy of our model we produced a benchmark using the initial conditions of the hydrodynamical simulations as a parametric disk with no embedded planet. The gas and dust temperature were fix and consider to be equal. We assumed a conventional ISM dust-to-gas ratio of 0.01 for the simulations.

In both cases, continuum emission and its absorption by the gas depends on the dust size for specific wavelenghts, vertical and radial distribution of grains along with its size distribution are relevant to neither underestimate nor overestimate gas emission. The vertical distribution and the grain size change the opacity and continuum emission of dust, thus, they change the thermal equilibrium of the disk, altering the gas line and the dust continuum emission. In other words, it alters the way that gas line emission is perceived [Barrière-Fouchet et al., 2005].

One of our aims is to trace the kinematic signatures of a protoplanet. Therefore, we included an embedded giant Jupiter mass planet to generate a vortex in the disk. After 500 orbits, the planet carved a gap in the disk with a stable profile and formed a vortex in the outer parts of the disk. We situated the planet at a distance of one hundred AU from the central star, in a fixed circular orbit. The acceleration that the star and the reference frame feel due to the planet's gravitational pull was also considered as an indirect term in the disk potential. This term could change the gap's width, the accretion rate and the total available mass in the disk. Regály and Vorobyov [2017] have reported that the indirect term may have significant effects in the kinematic structure of the gas for a massive planet.

As the system evolves, the drag in the dust particles changes their vertical distribution in the disk. Larger particles settles in the midplane, while smaller ones are more disperse and coupled to the gas. This stratification of the dust is called *dust settling*. The benchmarks were done in two scenarios. The first one has two dust populations with different sizes stratified in the disk. This was done to study the differences produced by dust distribution and how much of the emission observed is related to the amount of dust (larger particles have tighter distributions). In this two populations model, both of them follow a gaussian vertical distribution, but with different dispersions. The group of smaller particles is coupled to the gas, i.e., it behaves as the gas does, and the group of larger particles has a dispersion equal to the one used by Armitage [2007]:

$$\frac{\rho_p}{\rho} = \left(\frac{\rho_p}{\rho}\right)_{z=0} \mathrm{e}^{-\frac{z^2}{2h_\mathrm{d}^2}}. \tag{2.2}$$

The scale height is linked to the distribution and dispersion of the particles, and it is given by:

$$h_\mathrm{d} = \sqrt{\frac{D}{\Omega_K t_\mathrm{fric}}}, \tag{2.3}$$

being D the dissipation coefficient. The other scenario uses just one population, which is coupled to the gas.

During the radiative transfer simulations, we input a uniform microturbulence term (a_turb) in the parametric disk. We set it to 0 for the benchmark and for the hydro-dynamical simulation. It is expected that in the hydro-dynamical simulations, microturbulence should have an effect in the line shape as it is included in the radiative transfer code. According to our definition of turbulent velocity, it would be related with the microturbulence through

the relation:

$$v_{\rm turb} = a_{\rm microt}/\sqrt{2}. \tag{2.4}$$

2.2.2.1 Synthetic images for CO isotopologues for a face-on disk

We generated data cubes of line emission in radio wavelenghts for the benchmark model and the simulations. We used three different CO isotopologues lines in the rotational transition $J = 3 - 2$; ^{12}CO, ^{13}CO and C^{18}O. This particular molecular transition is observable with ALMA band 7, however, the same procedure could be applied for another transitions or molecules as well, being highly replicable. The relative abundances assumed between CO isotopologues and the rest frequencies for the transition are listed in Table 2.2. To reproduce observational features we used a circular beam with a size equivalent to 0.1 arcsec. For a source at a distance d=140 pc, the observations would have a resolution close to 15 AU in the disk. We did not convolved the benchmark because we wanted to recover the uncertainties of the model using a native resolution without smoothing effects. The images themselves do not have any errors, but an error of 2.4 mJy arcsec^{-1} was considered for the line fitting. Despite that the uncertainty is included in the fitting, because no noise was added to the simulations there is a bias in the analysis and the results are based on a best case scenario.

The gas density is used as a proxy for the dust density, as we did not solve for the dust evolution in our hydro-dynamical simulations. Dust opacity is given by a mixed population between astrosilicates (70%) and amorphous carbon (30%). The dust size distribution ($n(a)$) of the populations follows a power law proportional to the dust grain size , i.e.,

$$n(a)\mathrm{d}a \propto a^{-3.5}\mathrm{d}a, \tag{2.5}$$

where a is the size of the dust particle, spanning from 0.1 μm to 1 cm in grain size.

2.2.3 Input Fields for Benchmark

Our fitting model compares and tests for kinematic signatures in observations using 3D hydro-dynamical simulations, which were post-processed with radiative transfer. We started comparing the fitted parameters measured by the line diagnostic of a parametric disk. Given that the input grid of parameters is in 3D, we compared them using the following steps:

1. The spherical 3D grid of the parametric disk is transformed into a cartesian grid. This procedure is done to facilitate the integration along the line of sight from the observer. It also allows to compare between the controlled input and the output of the fit. We transform the coordinate through a trilinear interpolation layer by layer of the disk in the vertical coordinate. At the end, the initial spherical grid is converted into a new 3D grid in cartesian coordinates.

2. The input parameters are integrated along the direction of the observation, for inclined disks the integration is done through distinct layers at different regions of the observed disk. The integral along the line of sight is weighted by the gas number density until the optical depth, τ, reaches the value one (τ=1), otherwise it is integrated to the highest optical depth possible, meaning that it is an optically thin regime. At the end, the integral has to be normalized by the total column density up to the $\tau = 1$ layer. Integrations were done for each of the parameters (using temperature as an example) in the following manner, :

$$T_{\rm inp}(x,y) = \frac{\int_0^{\tau=1} T(x,y,z)\cdot n_{\rm H}(x,y,z){\rm d}\tau}{\int_0^{\tau=1} n_{\rm H}(x,y,z){\rm d}\tau}, \tag{2.6}$$

$T_{\rm inp}$ is the input temperature of the final image and $n_{\rm H}$ is the number density of hydrogen (most of the particles in the disk are hydrogen).

Other parameter measured by the our diagnostic of line emission is the column density. For a given molecule along the line of sight it is defined as :

$$N_{\rm X} = \int_0^{\tau=1} f_{\rm X}\cdot n_{\rm H}(x,y,z){\rm d}\tau, \tag{2.7}$$

where $N_{\rm X}$ is the column density of the X molecule(amount of X particles in the line of sight per unit of surface) and $f_{\rm X}$ is the isotopologue fraction of X with respect to H_2. In our study, we used CO isotopologues; particularly ^{12}CO, ^{13}CO and C^{18}O. The CO isotopologues can be observed in the same narrow spectral window, but having distinct abundances, they trace different vertical layers in the disk.

The final parameter that the model fits is velocity. We distinguish between the velocity of the grid ($v^2_{\rm grid} = v^2_\phi + v^2_r + v^2_\theta$) and the input velocity. The first one (v) is the velocity in the grid of the simluations, while the last ($v_{\rm inp}$), the one that we expect to observe and measure. The turbulent input velocity is calculated considering that it has two different components, a thermal and a turbulent one, which are related through the relation: $v^2_{\rm inp} = \frac{kT}{m} + v^2_{\rm turb}$. The final turbulent velocity is then $v_{\rm turb} = \sqrt{v^2_{\rm inp} - \frac{kT}{m}}$.

We then set the input velocity as:

$$v_{\rm inp} = \frac{\int_0^{\tau=1} v_{\rm turb}(x,y,z)\cdot n_{\rm H}(x,y,z){\rm d}\tau}{\int_0^{\tau=1} n_{\rm H}(x,y,z){\rm d}\tau}. \tag{2.8}$$

The model can also be applied considering inclination; however, at high inclination the measurement becomes more degenerate because the line of sight crosses distinct regions of the disk at different radii, thus the temperatures and physical conditions could substantially change. To integrate the dispersion in velocity with inclination, the initial grid must be rotated and then projected along the direction of the line of sight. Taking (r, ϕ, θ) as radius, azimuth and colatitude of the initial grid with their respective velocity components (v_r, v_ϕ, v_θ) and i the inclination angle, the projected velocity component in the disk is:

$$\begin{aligned} v_{\rm i} = \;& v_r(\sin{\rm i}\sin\theta\sin\phi + \cos{\rm i}\cos\theta) + \\ & v_\phi \sin{\rm i}\cos\phi + \\ & v_\theta(\sin{\rm i}\cos\theta\sin\phi - \cos{\rm i}\sin\theta). \end{aligned}$$

Table 2.1: Parameters of the Parameteric Disk or Benchmark Model.

Parameter	Value
Flaring Index	1.15
Disk Mass	1.5 M_J
Star's Mass	1 $M_\odot$
Star's Temperature	7000 K
Radius Range	$[4, 280]$ AU
Colalitude Range	$[1.25, 1.57]$ radians
Azimuth Range	$[0, 3.14]$ radians
Dust Grain Size Range	$[0.09, 1500]\mu$m
Grain Size slope	-3.5
Inclination	$0°$

Table 2.2: Isotopologues Abundances.

Isotopologue	Relative Abundance to H	Isotopologue fraction (f)	Rest frequency [GHz]
[^{12}CO]	10^{-4}	1.0	345.79601898
[^{13}CO]	$1.25 \cdot 10^{-6}$	0.0125	330.5887993
[C^{18}O]	$1.78 \cdot 10^{-7}$	0.0018	329.3305802

3. After that, the 2D map of the disk is masked to avoid problematic pixels at the edges. These pixels may overestimate the error between the model and the synthetic images. The mask was done considering just the points were the emission is higher than one third of the peak ($I > I_{\max}/3$). Although the algorithm could be computational expensive, it can be applied locally to a mask at lower computational costs.

2.3 Spectral Modeling

2.3.1 Line emission Diagnostic

We use the uniform slab approach to model the emission of each line. We assume LTE conditions and solve the radiative transfer equations to make a line diagnostic of the gas emission in the protoplanetary disk. The kinematics and the opacity in the disk model are dependent on its thermal structure. In particular, the opacity at a given frequency is highly dependant on the physical conditions of the gas, such as: temperature, velocity and column density. The model for the intensity received is stated in the following equation:

$$I_\nu(\tau_\nu) = B(T, \nu)(1 - \mathrm{e}^{-\tau}) + I_0(\frac{\nu}{\nu_0})^\alpha \mathrm{e}^{-\tau}, \tag{2.9}$$

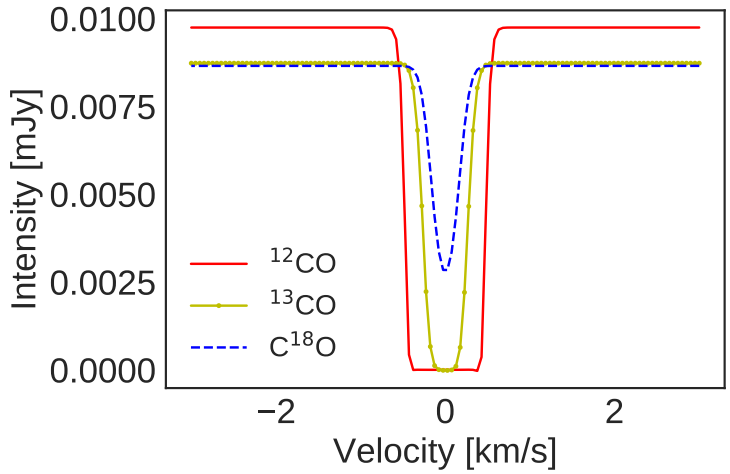

Figure 2.2: Dust emission absorbed under the line for different isotopologues. It is observed that gas absorbs part of the dust emission as it was previously noticed by [Boehler et al., 2017]. Thicker isotopologues (^{12}CO and ^{13}CO) absorb most of the dust emission. If this effect is not taken into account there would be an underestimation of the line emission.

with τ the optical depth, ν_0 the rest frequency of the molecule observed, α the spectral index and $B(T, \nu)$ the blackbody emission at temperature T and frequency ν.

We based our line emission model based on a similar approach previously done by Williams and Best [2014], although our model has the dust continuum absorption by the gas. The line diagnostic is intended to work in small spectral windows, thus the continuum is assumed to be a constant with value I_0 but modulated by the spectral index α. However, gas absorption of the continuum is considered and included in the optical depth profile, meaning that dust emission is absorbed by the gas under the line. Figure 2.2 shows that optically thick tracers, like ^{12}CO, have larger absorption of the dust emission than optically thin ones, such as C^{18}O.

The line profile is modeled with a gaussian function. In this gaussian, the broadening of the line (its dispersion) is given by the kinematics of the gas. The principal broadening factor of the molecular line is the velocity dispersion. We intend to separate this dispersion in two terms. The first term is the thermal broadening, and the temperature is tied to the peak of the line (its maximum intensity). The other term is the turbulent velocity. This velocity component is related to the kinematic effects of the gas dynamics and planet-disk interactions without considering temperature. When there is noticeable turbulence in the gas, broader lines are expected [Regály et al., 2014]. The optical depth in the model would be determined by the column density [Mangum and Shirley, 2015], the collisional cross section of the respective isotopologue and the inclination of the disk. Additionally, for long wavelength emission (sub-mm or longer), a correction for stimulated emission must be included. The optical depth of the lines is then:

$$\tau_\nu = N_u^{\mathrm{CO}} \cdot \exp\left(\frac{h\nu}{k_B T} - 1\right) \cdot f \cdot \frac{c^2}{8\pi\nu^2} A_{ul} \cdot \sec(\mathrm{i}), \tag{2.10}$$

where $N_u^{\rm CO}$ is the CO column density in the upper state of the transition observed, f is the isotopologue fraction, A_{ul} the Einstein coefficient for the transition to be observed, $\phi(\nu)$ the frequency dependent line profile and i the inclination angle of the disk. To simplify notation we will denote

$$\sigma = \frac{A_{ul}c^2}{8\pi\nu_0^2} \cdot \phi(\nu). \tag{2.11}$$

The $\phi(\nu)$ profile defines the line shape of gas emission and its dependence on turbulent velocity and temperature, which is mostly expressed on the broadening of the line. The line shape used is:

$$\phi(\nu) = \frac{1}{\Delta\nu\sqrt{2\pi}} \exp \frac{-(\nu-\nu_0)^2}{2\Delta\nu^2}, \tag{2.12}$$

where

$$\Delta\nu = \frac{\nu_0}{c}\sqrt{\frac{kT}{m} + v_{\rm turb}^2}. \tag{2.13}$$

One of the main difficulties measuring the gas kinematics is to accurately define the velocity deviation of the particles respect to the velocity centroid. The most usual approach is to directly measure the standard deviation of the line profile with respect to the weighted velocity centroid as a velocity dispersion estimator. The problem is that this dispersion contains both, thermal and turbulent components. To distinguish between both of them, temperature should be also measured to quantify and then subtract its effect on the net broadening. The effect on the gas kinematics of any not thermal phenomenon could be obtained separating these two components, for example, planet induced structures in the disk. We defined the thermal kinematic component as:

$$v_{\rm thermal} = \sqrt{\frac{k_B T}{m}}. \tag{2.14}$$

Because the measured column density corresponds to the amount of gas in the upper or excited state of the transition observed, the total column density is recovered using the rotational partition function:

$$Q_{\rm rot} = \sum_{\rm i} g_{\rm i} \exp\Big(\frac{-E_{\rm i}}{kT}\Big). \tag{2.15}$$

For LTE conditions, the total column density, $N_{\rm tot}$, is given by the following relation:

$$N_{\rm tot} = N_u \cdot \frac{Q_{\rm rot}}{g_u} \exp\Big(\frac{E_u}{kT_{\rm exc}}\Big). \tag{2.16}$$

2.3.2 Optimization of the Line Diagnostic

To find the physical conditions that fit the observed emission, we minimize a target function. The target function to minimize is the negative log likelihood (NLL) between the model

Table 2.3: Parameters range for the spectra fitting.

Parameter	Range
Temperature [K]	$[5, 100]$
$N_{CO}[cm^{-2}]$	$[0, 10^{22}]$
$v_{turb}[cm{\cdot}s^{-1}]$	$[0, 60000]$
ν_0 [Hz]	$[\bar{\nu} - d\nu/2, \bar{\nu} + d\nu/2]$

and the line. To minimize the NLL we use the Minuit algorithm [James and Roos, 1975]. Minimizing the NLL is equivalent to maximize the likelihood of the model, therefore, the maximum a posteriori (MAP) probability of the model is also maximized. The Likelihood Probability function used for the model is related to the χ^2 error between the model and the data of the simulations, which is the following:

$$\mathcal{L}(\text{pars}, \nu) \propto \exp \sum (I_\nu - I(\text{pars}, \nu))^2 / 2\sigma^2. \tag{2.17}$$

The parameters of our line model were bounded by a physical range to improve the spectral fitting. The range used for each parameter is detailed in Table 3.1, where $\bar{\nu}$ is the frequency obtained from the first moment (centroid) of the spectrum at each pixel, which is calculated using $\bar{\nu} = \frac{\sum I_j \nu_j}{\sum I_j}$, and $d\nu$ is the spectral resolution of the simulation or the observations. For inclined disks, the centroid of the line is also fitted as a free parameter, given that the line is not necessary centered at the rest frequency of the molecule as it does in face-on (i=180°) parametric disks.

Once the parameters from the model are obtained, we calculated a relative error between the expected parameter from the input and the one fitted by our line diagnostic.

$$e_p = \sqrt{\frac{\sum_i (\frac{P_i^{\text{input}} - P_i^{\text{fit}}}{P_i^{\text{input}}})^2}{N}}, \tag{2.18}$$

$$e_v = \sqrt{\frac{\sum_i (v_i^{\text{input}} - v_i^{\text{fit}})^2}{N}}. \tag{2.19}$$

We used Equation 2.18 for the temperature and the column density. For the velocity dispersion, we used the mean squared error (eq, (2.19)) instead because velocity dispersion could have a zero value making the error diverge (this happens in the case of the face-on parametric disk with no microtubulence).

To test our diagnostic tool, we made different cuts for each measured parameter on the physical 2D fields. Azimuthal cuts were done at specific radii. This radii were chosen where the dispersion and parameters error were the highest or they were of particular interest for kinematic structures.

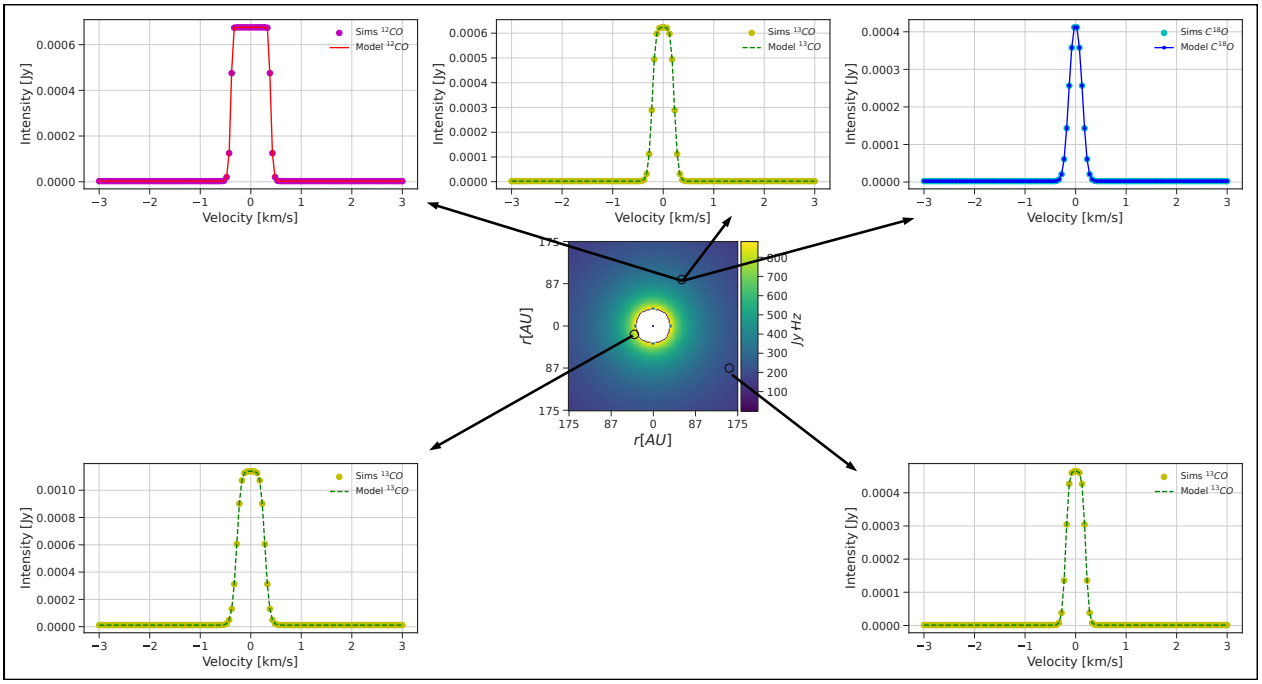

Figure 2.3: Spectra fitting at different points of the parametric disk. **Top**: ^{12}CO, ^{13}CO, C^{18}O from left to right. **Center**: Integrated spectra in frequency, **Bottom**: ^{13}CO fits. The algorithm fits the spectra at different regions of the disk and with different isotopologues. It is observed that the line profile is recovered at different temperatures and gas abundances.

We calculated two different cuts. The first cut is a radial one at a specific direction (fixed azimuth) and the second one is a general radial cut. For the second cut, the median for all the azimuths at a specific radius was used as the estimator for the physical condition at that distance.

2.3.3 Spectra Fitting using the Line Diagnostic

Using the parametric face-on disk, the measured parameters by the fit match the input parameters given by the parametric disk of the simulations (Fig 2.3). Despite that, the observed spectra in inclined disks of optically thin molecules, such as C^{18}O, show a non gaussian profile with more than one peak in the emission. This is produced because the line of sight goes through more than one region in the disk. These regions have different orbital velocities and distinct projected components along the line of sight, so their emission peaks at different frequencies. For cases with optically thin isotopologues and inclined disks, it is more difficult to produce good measurements of physical conditions given that emission comes from different zones that are probably under different sets of physical parameters.

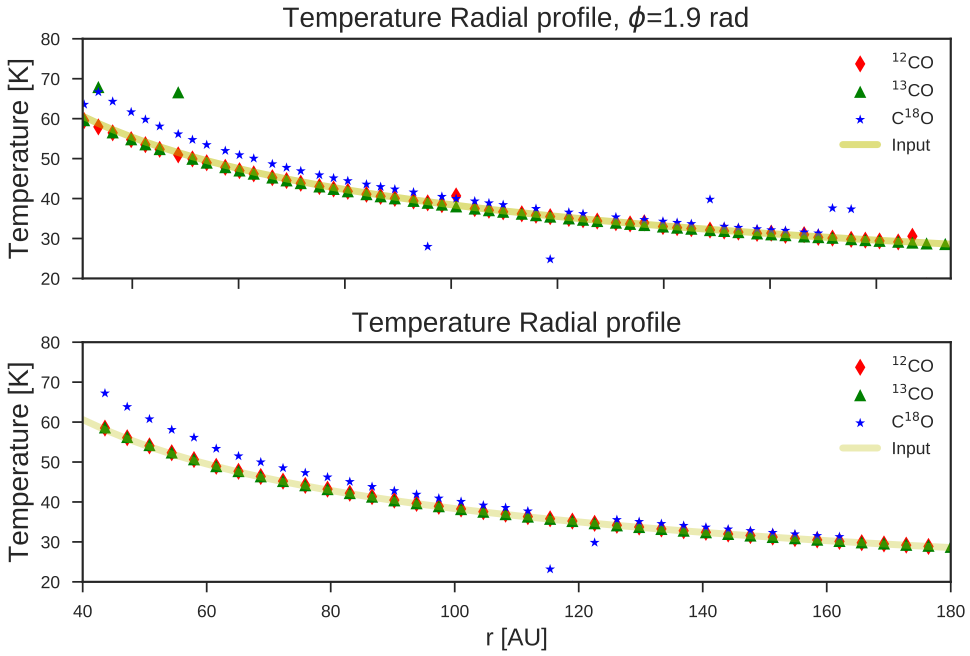

Figure 2.4: Temperature radial cut for the face-on benchmark model (i = 180°).**Top**: Temperatures at a particular azimuth, $\phi = 1.2$ radians. **Bottom**: Median Azimuthal Temperature. It is illustrated that the measured temperature matches the input even at specific directions.

2.4 Results

2.4.1 Temperature Fields recovered by the line diagnostic.

The temperature was fixed for both models, so it should recover the power law profile given in equation (2.6). Figures 2.4, 2.5 and 2.6 illustrate the measured temperatures for the benchmark in a 2D field, and both radial and azimuthal profiles. Fig. 2.4 shows that except from C$^{18]}$O at the very inner regions, the CO images allow us to measure the temperature in the disk with a very low error, matching the power law profile as an azimuthal average and at a specific random direction. This trend is also observed in the azimuthal cut of the Figure 2.5. The azimuthal profile (Figure 2.5) show that the behaviour of the most optically thick isotopologues is more stable and close to the input temperature. The C^{18}O shows a scatter $\sim$ 20 K and it is centered around a temperature $\approx$ 2K above the input level. Of the three isotopologues the most stable is the ^{13}CO, the temperature measured from it is well related to the input. Finally we can observed the combined effect of both ob them in the 2D map in Fig. 2.6, where it can be seen that the deviations are of the order of $\sim$5 K.

The ^{12}CO and ^{13}CO are able to recover the temperature profile from the input, while C^{18}O has an error that reaches the 20 K (Figure 2.6) in the region with radius $r \in [80, 120]$ AU. Additionally, the C^{18}O temperature in the figure shows concentric rings that result in systematic errors in its measurement.

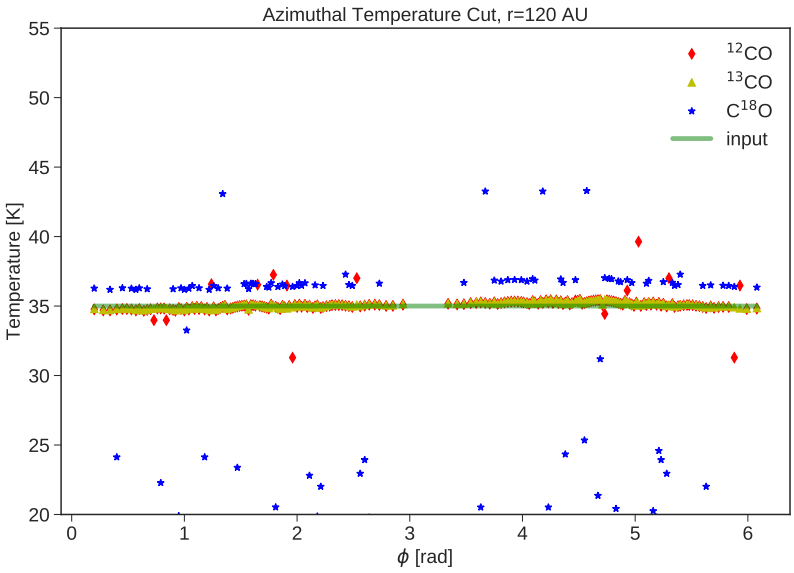

Figure 2.5: Temperature in azimuthal cut at a physical radius of 120 AU. The cut shows that ^{12}CO and ^{13}CO, the optically thicker isotopologues recover the temperature of the field, while C^{18}O, which is optically thin, overestimates the temperature, but in less than four Kelvin degrees for distances larger than 60 AUs.

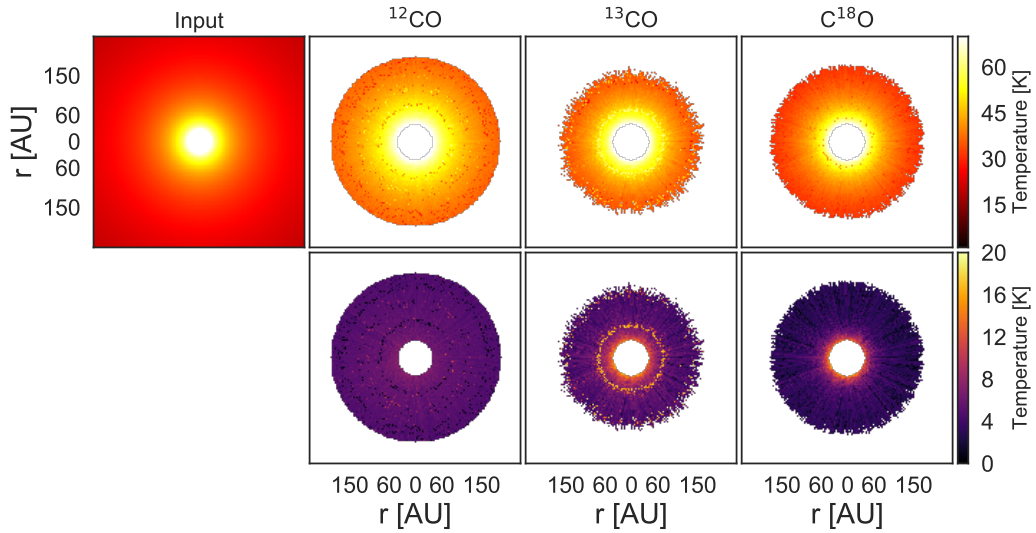

Figure 2.6: Comparison between the temperature field and the input measured. **Top**: Input temperature of the model, ^{12}CO, ^{13}CO, and C^{18}O. **Bottom**: Residuals between the recovered temperature and the input.

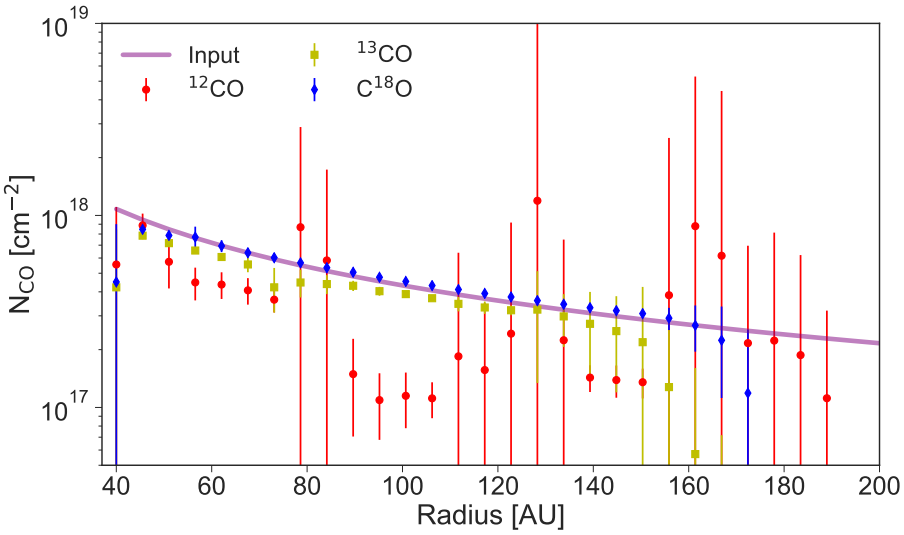

Figure 2.7: Radial profile recovered from the benchmark or parametric disk for the three isotopologues. The profiles illustrates the measured column density with its numerical error in the fitting in a profile withou addition of noise. As expected, $C^{18}O$ is the one with more reliability and ^{12}CO the most uncertain. The uncertainty in the column density for ^{12}CO also produces uncertainty in the turbulent velocity measurements. At higher radii the measurement is no longer reliable for optically thin traces, which is produced by the low temperatures of the gas and its low density, so line emission becomes comparable to the dust continuum, making the measurement of the line harder.

2.4.2 Column Density Measurements and Differences between Isotopologues.

2.4.2.1 Measurement for the Column Density in a Parametric Disk

Given the fact that the optical depth of the gas is strongly related to the column density of gas. $C^{18}O$, being the least abundant molecule, tracing even to the midplane layer. On the other hand ^{12}CO is too thick to be a reliable estimator of the total amount of gas along the line of sight. Figure 2.7 and 2.8 show the profiles recovered for the column density. We can observe in Figure 2.7 that it follows the power law profile of the column density for the set gamma value of $\gamma = 1$, i.e., $N_{\rm CO} \propto r^{-1}$. The errorbars are the dispersion of the values measured in the azimuthal direction. It can be seen that the uncertainty in ^{12}CO is even higher than an order of magnitude in some cases. On the contrary, ^{13}CO and $C^{18}O$ show a better constrain of the local column density, being $C^{18}O$ the best tracer in this case with a very low dispersion, except at larger radii, when the temperature is too low, so the continuum and line emission are more difficult to decouple. 2.8 illustrates the radial profile at a radius, r=144 AU. The same behavior that was observed in the radial case is observed here, although the dispersion at this particular radius is lower for all the isotopologues. Nevertheless, ^{12}CO presents a systematic off set of a factor between two and three between the exact amount of gas, underestimating it. Therefore, ^{12}CO can not be trusted as a column density tracer.

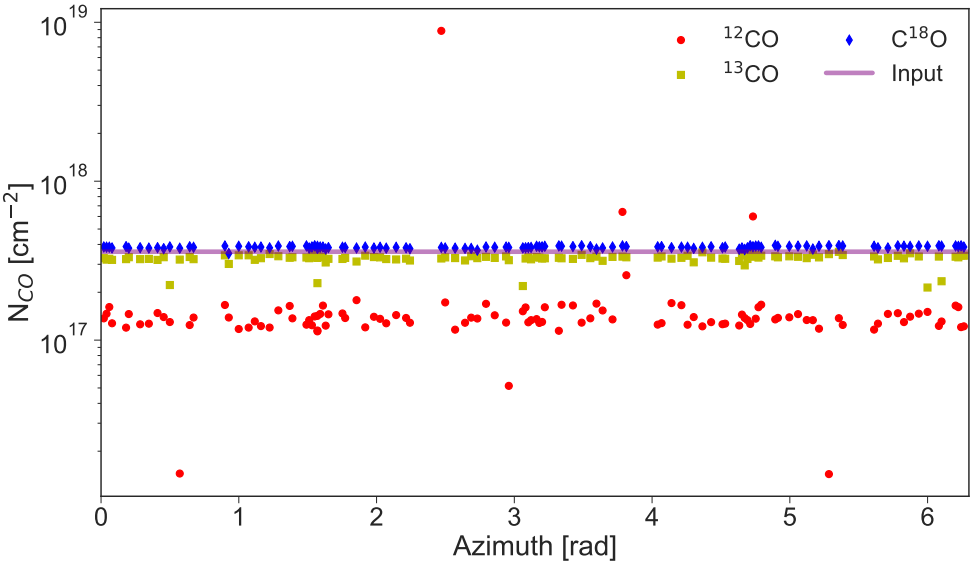

Figure 2.8: Azimuthal profile recovered from the benchmark for the three isotopologues at 120 AU. It is observed that C^{18}O and ^{13}CO have the best behavior in the measurement of the column density, while ^{12}CO underestimates the column density by a factor between two and three. The errorbars for ^{13}CO and C^{18}O are smaller and in the same order of magnitude. On the contrary the dispersion of ^{12}CO is much higher and leads to higher uncertainties in the turbulent velocity as well.

Despite the fact that there is a higher degeneracy between temperature and column density in optically thin case, C^{18}O does not seem to show any trouble recovering both quantities at higher radii. The degeneracy is visible in the equation 2.9 for the optically thin regime ($\tau << 1$). In that case is no longer easy to decouple temperature and column density. The approximation $e^{-\tau} \approx 1 - \tau$ for low optical depths makes the degeneracy more visible:

$$I_\nu(\tau_\nu) = B(T, \nu)\tau + I_0(\frac{\nu}{\nu_0})^\alpha(1 - \tau), \tag{2.20}$$

An increase in temperature could be compensated by a decrease in $N_{\rm CO}$ and vice versa, making the degeneracy more visible.

2.4.2.2 Hydrodynamical Simulation and Radiative Transfer post-processing setups

We measured the expected column densities in our synthetic images of a hydro-dynamical simulation using the three isotopologues. Figure 2.9 illustrates the input column density and Figure 2.10 shows the quantities given by the model. It is clear that the horseshoe is observed in ^{13}CO and C^{18}O; however, the ^{12}CO seems pretty uncertain as it was expected. Figure 2.10 shows the peak in column density under the horseshoe concentrating a higher amount of gas. As it was shown in the parametric disk, C^{18}O has the best accuracy in the recovery of the column density; however, when either the temperature or the column density is too low,

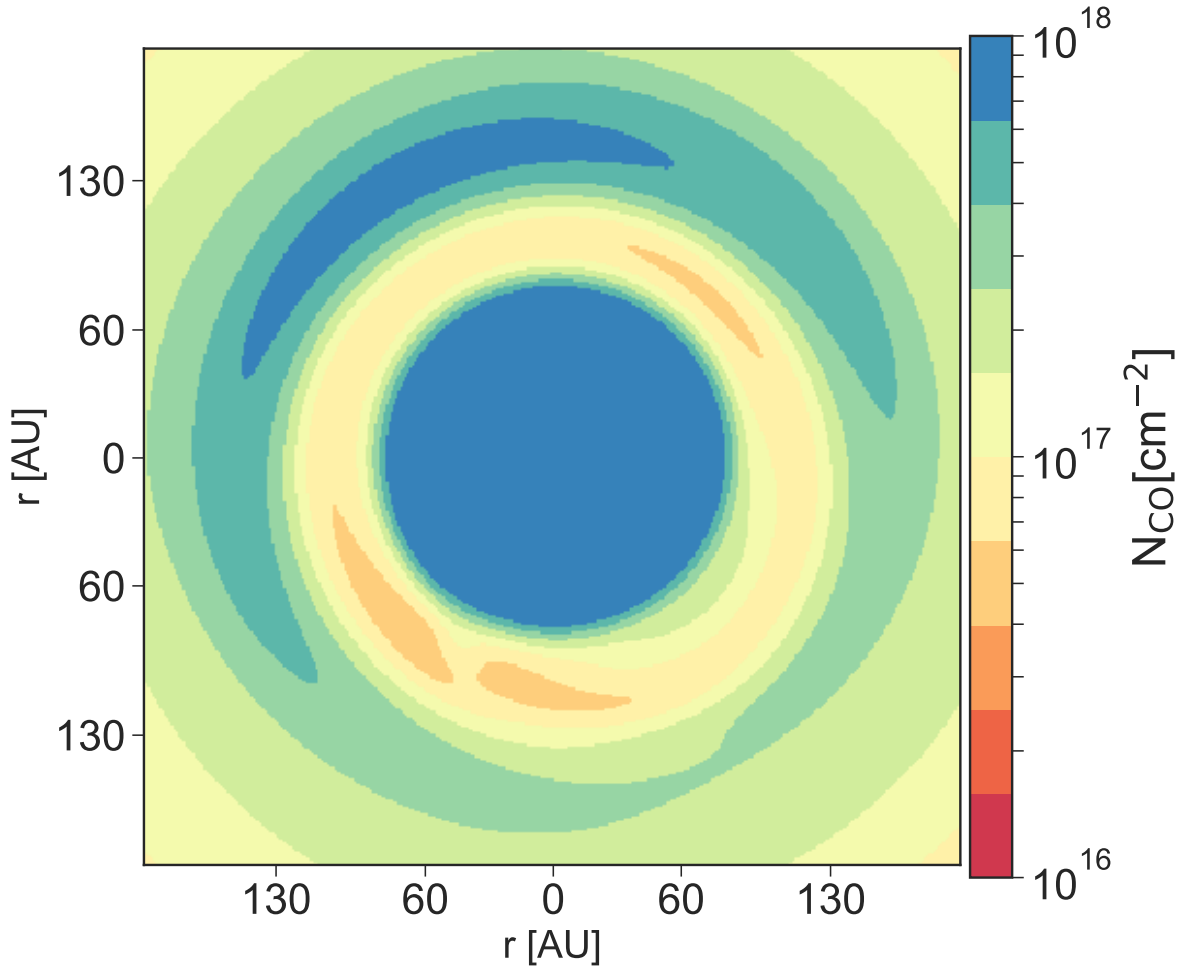

Figure 2.9: Input image of the column density for $C^{18}O$. The image presents a horseshoe feature in the gas. The goal of the line diagnostic is to recover the column density and the turbulence in the disk, i.e., the input field.

the diagnostic underestimate the line emission. $C^{18}O$ shows a higher contrast, although the emission at that radius is lower, and given the less amount of material in the opposite side of the horseshoe, the measurement becomes more difficult at that region.

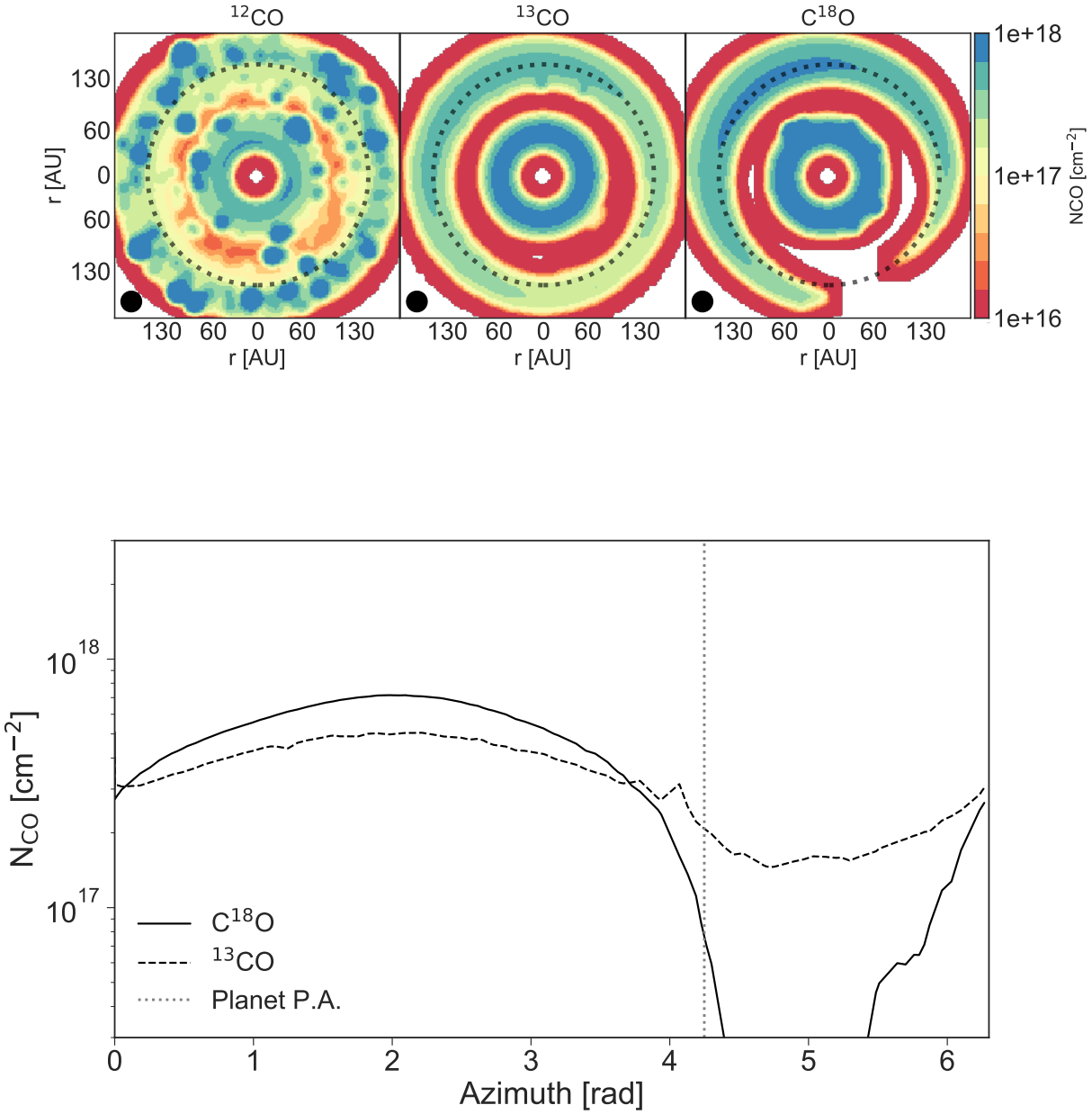

Figure 2.10: Images of the measured column density in a transition disk with a one Jupiter mass embedded planet at 100 AU. **Top**:Column density measured from each isotopologue. Because C^{18}O is the most optically thin, it is the most reliable to measure the column density, however, outside the horseshoe the emission decreases so it becomes more difficult to measure it. The ring shows the peak intensity in the horseshoe at r=144 AU. **Bottom**: Azimuthal profile of the column density measured in ^{13}CO and C^{18}O at r=144 AU. There is a contrast of a factor 2.3 in ^{13}CO inside the horseshoe and outside of it.

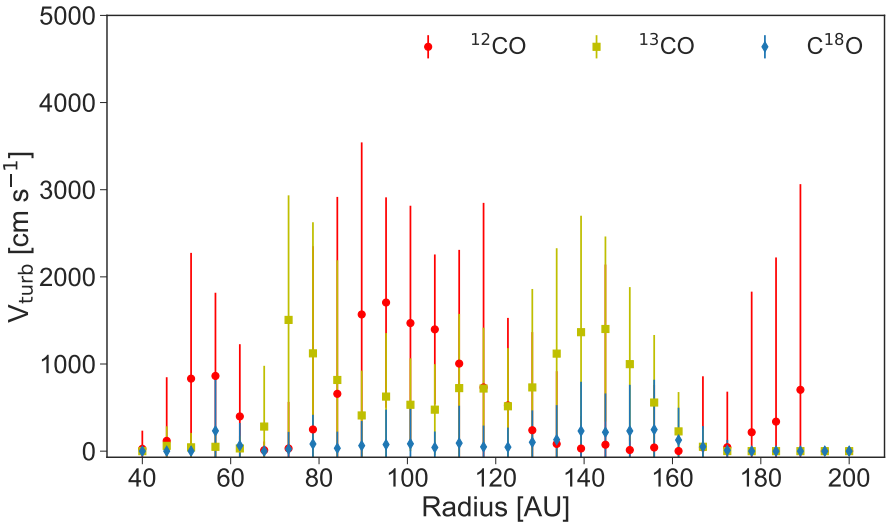

Figure 2.11: The Figure shows the turbulent velocity with its dispersion at each radii. $C^{18}O$ has the lowest values measured, even though is the optically thin isotopologue. Despite the fact that ^{13}CO measurements are not 0, its values are within the dispersion and are low enough to keep being reliable. ^{12}CO has the highest dispersion and highest values among the three isotopologues, however it. Again it is important to keep in mind that the synthetic images have not white noise added, so this error is only numerical.

2.4.3 Turbulence in the Gas Kinematics in the Planet's Orbit and under the Horseshoe

2.4.3.1 Measurements in a Parametric Disk and Numerical Errors

After running the line diagnostic in the benchmark model, there should be no turbulent velocity in the fit measurements. Because we expected 0 turbulent motion, any measurement is basically the error of the model. The most trustworthy isotopologue is $C^{18}O$, although the three of them have good performances, considering that the spectral resolution of the simulations is of 75 m s^{-1} between channels.

Figures 2.11 illustrates the radial profile of the turbulent velocity, and **??** shows an azimuthal cut at 144 AU, where the horseshoe is. In the radial profile $C^{18}O$ is consistently null with small variation within the spectral resolution of the synthetic images. ^{13}CO measurements are above zero, but all of them are within the dispersion value. The isotopologue with the highest turbulence measured is ^{12}CO probably produced by the saturation of the line, which increases the uncertainty in the measurment for this particular isotopologue. The azimuthal profile shows a similar trend, but it is not exactly the same. $C^{18}O$ has null measurements, but ^{12}CO and ^{13}CO have the same level of scattering, around 20 m s^{-1}.

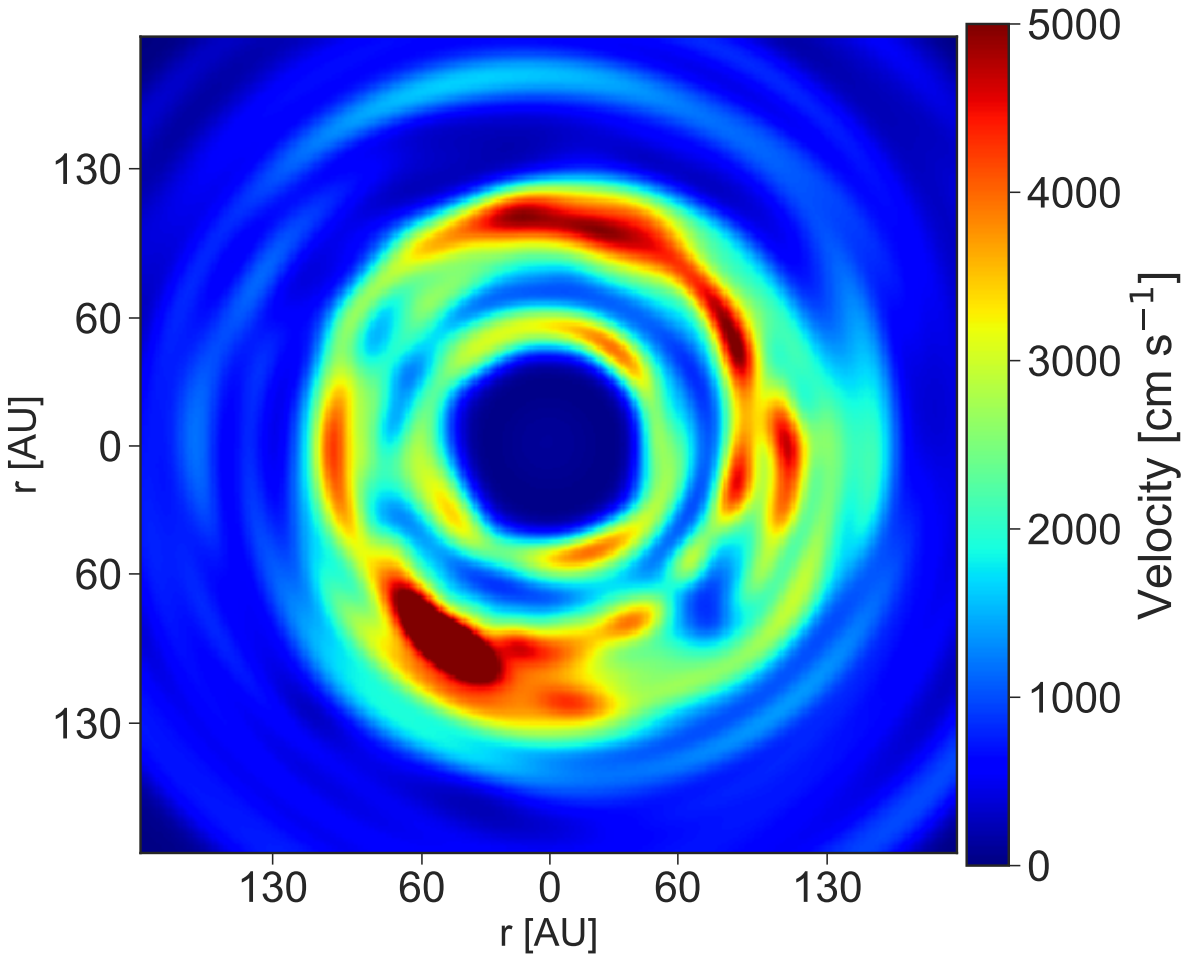

Figure 2.12: Input image of the turbulent velocity for ^{12}CO. The turbulent velocity in the simulations was calculated using equation (2.8). The peak in the turbulent velocity is at the position of the planet, the horseshoe does not show a considerable turbulence for the input, although is slightly higher in that region.

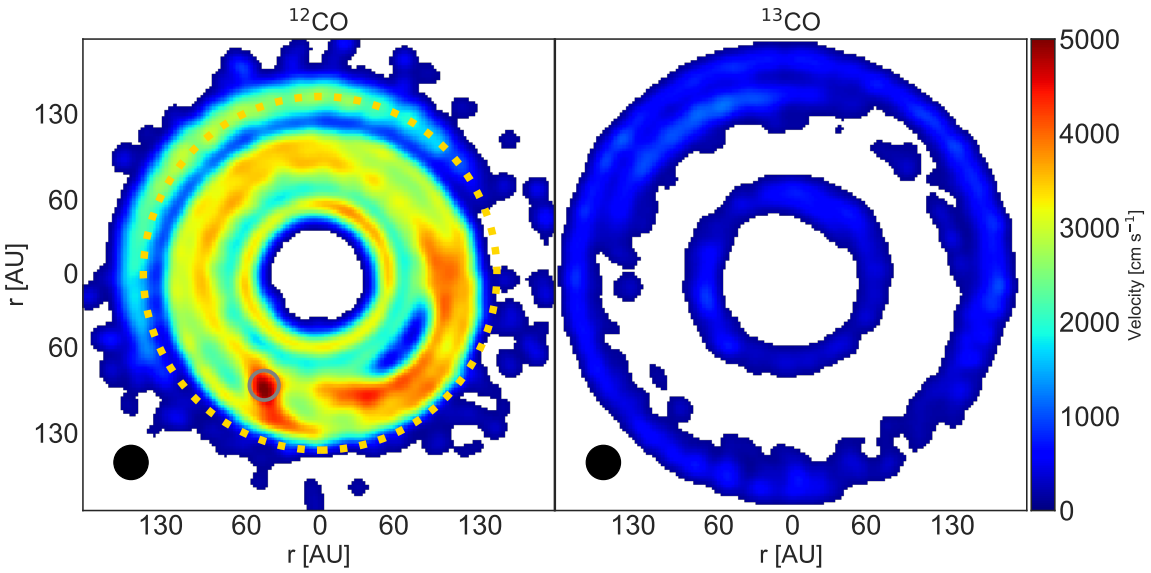

Figure 2.13: Images of the measured turbulent velocity in a synthetic transition disk with a one Jupiter mass embedded planet at 100 AU. The turbulent velocity is shown for ^{12}CO and 13CO, C^{18}O emission is too weak to allow for measurements in the turbulence, given the simulation conditions. The figure shows that the only isotopologue with a strong turbulence is ^{12}CO. The planet is located at a PA=240° and it is marked in the plot with a gray circle. ^{12}CO measurements recover the higher turbulence in the planet's orbit, although the horseshoe has a stronger signal that the one present in the simulations. The golden circle represents a circumference at 144 AU from the star at the maximum gas emission inside the horseshoe.

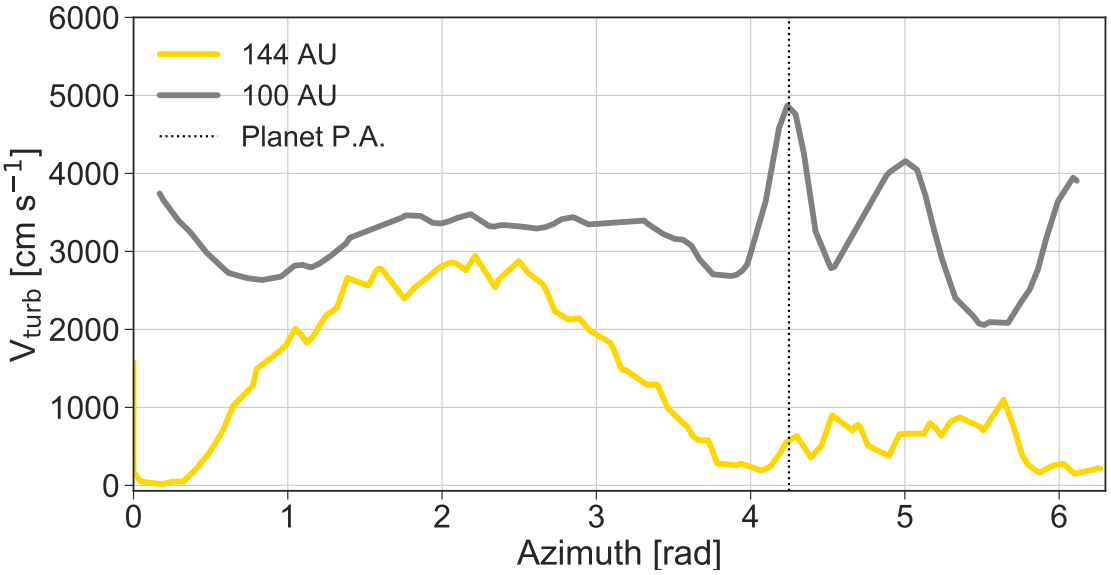

Figure 2.14: Azimuthal profiles at the planet's orbit and at the peak of the horseshoe. It is observed that turbulence reaches a maximum in the planet's locations, where it reaches a value of 58 m s^{-1}. Also, there is a measured turbulent velocity in the horseshoe with a peak value of 29 m s^{-1}, however the horseshoe's signature was not observed in the input image.

2.4.3.2 Turbulent Velocity in the Simulations using CO isotopologues

We analyzed the synthetic images of the disk for possible footprint of the planet's presence in the disk. Among the three isotopologues, ^{12}CO was the only one with a signal strong enough to be able to have a signature in the disk in the measured turbulence. We analyzed the azimuthal profile in both the horseshoe and inside the gap in the planet's orbit. Figure 2.12 is the input velocity field for ^{12}CO and 2.13 show the image obtained from the line diagnostic of the convolved images. It is observed that the horseshoe's signature is not observed in the input field, although the kinmeatic signature in the planet's orbit is observed in both. The planet's orbit has the highest turbulence velocity in both cases, but it has a lower column density. Given that ^{12}CO is the most abundant isotopologue, it is the easiest CO isotopologue to observe. Figure 2.14 shows azimuthal cuts of the planet's orbit and at the peak of the horseshoe emission. From the figures, it could be inferred that the kinematic signature of the planet is much stronger in the upper layers than in the midplane of the line emission, because the signal was too weak in the other isotopologues or the kinematic footprint was too low. From the benchmark, the dispersion of the turbulent velocity at 144 AU was very low, less than 8 m s^{-1}, while the turbulence reaches a plateau of level of $\approx$ 32 m s^{-1}. The case of the planet's orbit is different because the dispersion was much higher, with $\sigma \sim 14$ m s^{-1}, but the peak in the planet's position is 52 m s^{-1}, higher than 3σ, so it could be detectable, and if the planet is even more massive the signature would be stronger.

2.5 Summary

We developed a line diagnostic using the uniform slab model to fit physical properties in protoplanetary disks. The line diagnostic was done using different molecular tracers in radio wavelengths. We aimed to give a characterization of the reliability of the measurement of physical features in the gas emission of disks. Particularly, we looked for kinematic signatures of a vortex produced by an embedded giant planet in the turbulence motion of the disk. The line shape contains relevant information about the temperature, amount of gas and the turbulence, but they are intimately linked, so a proper the model is needed in order to decouple them. Although our line diagnostic has the caveat that it models the line emission assuming LTE conditions and an isothermal structure, it also takes into account the effect of continuum absorption by the gas, effect that has recently been addressed. If this effect is not considered it leads to underestimation of the temperature and the column density of the disk. Among the different CO isotopologues, 12CO has the worst performance, but specifically for the column density. On the other side, C18O shows the best performance overall. It is the best tracer for the column density and the turbulent velocity, even though it was not the best thermal tracer, the uncertainties were not considerably high. Despite the fact that C18O is the best tracer to recover the physical conditions, the turbulence effect produced by the planet seems to be higher at upper layers in the disk. The turbulent velocity is clearly observed in the 12CO, in both the planet's orbit and in the horseshoe, reaching levels of $\sim$ 50 m s^{-1} and $\sim$35 m s^{-1} respectively. Despite that the turbulence peaks in the planet's orbit, the gas emission is lower inside the carved gap, so there was not recovery for the other tracers, and even though 13CO measures turbulence under the horseshoe, it is too low to be a considerable footprint of a vortex in the disk. Nevertheless, the analysis was done for a Jupiter mass planet, a standard and more conservative value, so a more massive planet would generate more turbulence in the disk, what could potentially produce a stronger kinematic footprint.

Chapter 3

Viscous Heating as a heat source in the FU Ori object V883 Ori

FU Ori objects with high accretion rates could lead to a better understanding of planet formation processes. The outburst of high accretion takes the snow lines farther out in the disk, so they are easier to observe and study. Among the FU Ori objects, V883 Ori was the first one with indirect evidence of a resolvable snow line. V883 Ori observations with the Atacama Large Millimeter and sub-millimeter Array (ALMA) presents an abrupt change in the spectral index at ∼40 AU of the central star. We show that the observed thermal profile at the inner disk is too steep for a standard passive disk, thus the usual heating components of a disk can not be the only heat sources. We introduce a model for the thermal structure of this source including accretional heating as an extra heat source. Our aim is to reproduce the thermal structure and morphology of the disk that could explain the observations. The disk modeling includes the effect of both, stellar and flaring heating terms; the influence in the disk shape caused by this outburst of accretion is included as well. To determine the accuracy of our model, we produce synthetic images with radiative trasnfer simulations that recreate the V883 Ori mm observations. Our final predictions underline the importance of this extra heating term for this class of source.

3.1 Introduction

FU Ori objects are young stellar objects with episodes of outbursts that occur when the accretion rates of the young stars are enhanced by orders of magnitude. During these events, they reach levels up to $10^{-5}, 10^{-4}$ $M_\odot$ yr^{-1} [Hartmann et al., 1996]. In particular, these stages could be a possible explanation for the low luminosity problem in the stellar formation process [Dunham and Vorobyov, 2012, Kóspál et al., 2017]. The luminosity of the protostars is not high enough to reach their final mass, meaning that they are not accreting as much as they are supposed to. These short episodes of high accretion rates infalling onto the protostar could solve this problem and they explain the low luminosities of the circumstellar disks during the low accretion rate states. Furthermore, the high temperatures enhances the

stickiness of dust grains, which is a possible formation scenario for dry planets [Boley et al., 2014, Hubbard, 2017].

Recent ALMA observations [Cieza et al., 2016] have shown that this class of sources have a very bright and optically thick core in the sub-mm continuum surrounded by an optically thin halo. An excess of emission at the inner parts and snow lines that are probably outer than usual. Cieza et al. [2016] measured the temperature in V883 Ori and resolved the region where $T < 115$ K, observing an abrupt change in the intensity at 42 AU. The change in the emission could be explained by the sublimation of ice grains, effect that adjusts the opacity of the dust grains. Consequently, the abrupt change in the optical depth could be interpreted as an indirect evidence of the presence of the snow line in a protostellar object. This phenomenon may be due to the heating produced by the outbursts of high accretion, which shifts the snow line outwards. Shifts in the snow line locations has been previously predicted by Min et al. [2011] and Lecar et al. [2006]. They located the snowline shift at a distance of the order of ~ 10 AUs.

Different features have been studied trying to explain possibles sources for the outward shift of the snow line. For example, Harsono et al. [2015] studied the disk thermal profile with a flattened envelope in the model; however, this envelope would shift the snow line just a couple of AUs. A shift of a few AUs is not enough to explain the case of V883 Ori, another heat source that would locate the snow line at distances of tens of AUs is needed. For luminous stars($> 10 L_\odot$), unless the accretion rate reaches values higher than 10^{-4} $M_\odot$ yr^{-1}, the shift would be produce mostly by stellar radiation rather than by viscous heating. Another possible reason for the outer location of the snow line could be found in the accretion rate that heats up the circumstellar disk, raising the dust emission.

Several approaches have been done to model the structure of FU Ori objects. For example, if matter starts to be accreted in the disk faster that onto the star, it will accumulate in a few AUs keeping the elevated temperatures in the disk [Gammie, 1996]. The star's accretion rate is not the same as the rate at which the disk is fed, producing a congregation of dust closer than 1 AU. Dust accumulation very close to the star has been predicted by Liu, Hauyu Baobab et al. [2017]. This effect is produced by the inefficiency of the gravitational instability (GI) to keep transporting material inwards at distances closer to the star; the pile-up of material in magnetic field dead zones will eventually activate a magneto rotational instability (MRI), producing the outburst of accretion. High concentrations of dust would increase the optical depth to values much higher than 1, thus increasing the dust emission for cases when it could be optically thin otherwise. However, Bae et al. [2014, 2013] described an alternative type of FU-Ori source with an inside-out burst produced by a non zero dead zone viscosity instead of the usual outside-in bursts of the GI + MRI process. MacFarlane and Stamatellos [2017] did models with radiative and episodic feedback. They found that episodic accretion changes the thermal and density profiles of the object.

Bell et al. [1997] showed that for FU Ori objects, the shape of their disks(their aspect ratio h/r) changes with radius, meaning that they have a non constant flaring index. The radial variability in the flaring index would produce some parts to be flared and another ones to be self-shadowed by the disk itself. For high accretion rates scenarios, the inner part of the disk follows a flared disk structure, but after a certain boundary radius the shape

changes because viscous heating is not as important as it is at ineer radii. At that point the scale height is lower because the disk is cooler, producing a self-shadowing. They also showed that the boundary zone is dependent on the accretion rate of the star; for example, in highly accreting stars, this radius would be of the order of tens of astronomical units. With this self-shadowing, the outer parts of the disk are not directly irradiated by the star. Moreover, Bitsch et al. [2013] showed that the inclusion of viscous heating produces thicker disks, although the accretion rates used in their simulations are still orders of magnitude lower than the ones measured in FU-Ori objects. The aspect ratio of their simulations follow a flatter profile for increasing accretion rate, rather than a flared structure. Bitsch et al. [2014] also reported changes in the structure of accreting discs with radial dips and bumps in the disk produced by the accretion rate. Thus, the study of a non-constant flaring structure in the parametric disk is needed for a thorough understanding of this type of objects, given that the disk could have a different shape farther out the snow line. This feature could be key to explain the excess emission at the inner part of V883 Ori and other FU Ori objects.

FU Ori objects are thought to be a short stage during low mass star formation. The phenomenology and the importance of testing the possible explanations for FU Ori thermal and density evolution are detailed in Armitage [2011a] and Hartmann et al. [2016]. Hartmann and Bae [2018] and Zhu et al. [2009] analyze how young stellar objects accrete, and what kind of thermal profiles should be expected for different parametric disks, changing the stellar accretion rate and the mass of the central star. Due to the high accretion rates reached by these objects, it is important to explore the heating sources that are involved and how these sources would change the emission in the inner and outer parts of the disk. Liu et al. [2017] reported that a possible combination of free-free and dust emission are relevant near the star, because most of the dust would be sublimated at those high temperatures. Despite that, we expect the free-free emission to be relevant for longer wavelenghts than ALMA band 6 observations at $\lambda = 1.3$ mm. Bitsch et al. [2015] studied the thermodynamics in the disk including the viscous heating and the opacity of the dust grains for different thermal regimes. They looked at different aspect ratios adjusting the radial dependence of the opacity in the disks; also, they explored the changes produced by the viscosity assuming an α-viscosity accretion disk [Shakura and Sunyaev, 1973b]. In some cases, when the self-shadowing is present in the disk, the outer part would become shielded to stellar irradiation by the denser and thicker inner regions.

We present the first model that replicates the steep thermal profile for V883 Ori at inner radius in mm wavelengths. We have included the viscous heating produced by the high accretion rates in FU Ori objects. For that, we used a self-consistent numerical modeling to input in a radiative transfer code. Our model includes the accretional heating as the main heat source in the inner disk, where the optical depth in V883 Ori has been predicted to be high to be emitting as blackbody. The self-iterative algorithm that we developed fits the continuum intensity modeling, the physical temperature, the dust distribution of the disk and its accretion rate.

The following paper is structured as follows. In Section 3.2, we explain a two layers analytical model for the disk using accretional heating. In Section 3.3, we present the model that we used as input for the radiative transfer code RADMC-3D [Dullemond et al., 2012]. In Section 3.4, we describe the results of the radiative transfer model for the dust and thermal

structure along with the predictions for the millimeter emission. Finally, in Section 5, we summarize our results and its conclusions.

3.2 Methods

3.2.1 Two layers model approach

Our first modeling approach was done with a passive disk(only with the irradiation heating). The model was resolved with a MCMC fitting of the observations(Pérez et al in prep), and it uses the self-similar solution of Lynden-Bell and Pringle [1974] for the dust surface density:

$$\Sigma = \Sigma_c \Big(\frac{R}{R_c}\Big)^{-\gamma} \exp\Big[-\Big(\frac{R}{R_c}\Big)^{2-\gamma}\Big], \tag{3.1}$$

where Σ_c is the dust surface density at the characteristic radius R_c. This first approach considers a constant flaring angle, i.e, the scale height is determined by the following equation: $h(R) = H_c(\frac{R}{R_c})^{\psi}$. A more detailed explanation for the parametric disk model and the MCMC fitting can be found in Cieza et al. [2017].

We used the parameters obtained from this simple passive disk fit as the starting point for our self-consistent model described below, where we added a variable flaring index and the viscous heating to the model. For this particular case, the parameters that fitted V883 Ori are detailed in Table 3.1.

The new Gaia DR2 [Gaia Collaboration et al., 2016, 2018] situates V883 Ori at a distance of ~ 270 pc, instead of the previous measurement of 414 pc **?**. It would relocate the snowline at a distance of 26 AU. However, because the distance to Orion has been pretty well constrained, we associated this distance to the outflows and to the luminosity of V883 Ori. A bright source in the optical, such as V883 Ori, is problematical to calibrate adn it would have higher systematical errors in Gaia DR2[**?**].

V883 Ori has a high measured bolometric luminosity of ~ 400 $L_\odot$ [Strom and Strom, 1993]. That luminosity is equivalent to a total star accretion rate of $\dot{M}_* \sim 7 \cdot 10^{-5}$ $M_\odot$ yr^{-1}. Although V883 Ori started its outburst of accretion nearly a century ago, its luminosity is still high enough to consider viscous heating as an extra heat source.

V883 Ori is a very young source, so it has a very massive disk. We set for the disk a total mass of 0.6 $M_\odot$. Given that the midplane optical depth is proportional to the dust density, we expect a optically thick disk at millimeter wavelengths, at least at the core of V883 Ori. Nevertheless, it could still be optically thick even at distances of tens of astronomical units from the protostar.

Table 3.1: Parameters of Parametric Disk in V883-Ori

Parameter	Value
Accretion Rate [$M_\odot \cdot yr^{-1}$]	$7.5 \cdot 10^{-5}$
ψ, Flaring Index	1.15
R_c, Characteristic Radius [AU]	31.6
H_c, Scale Height at R_c [AU]	4.17
M_d, Disk Mass [$M_\odot$]	0.6
γ	1.48

3.2.1.1 Model Assumptions

Our model has two types of layers. One is the surface or photospheric layer, from where most of the radiation comes, and the other one is the midplane at the center of the disk. We have assumed the following conditions: 1)It is geometrically thin enough to be considered locally plane-parallel. 2)The disk is axisymmetric. 3)The disk is in local thermodynamic equilibrium and the viscous heating is evenly distributed in the vertical direction [Flock et al., 2017]. 4)To use the Eddington approximation we need the radiation field to be isotropic, and the total radiation flux at the midplane to be zero. 5)For simplicity, we haven't considered scattering in the modeling, so the scattering coefficient σ_ν is set to 0 for the radiative transfer.

3.2.1.2 Heat Sources present in an Active Disk

For the model we have considered three heat sources. The first one is the irradiation heating that comes from the central star. The second one is the viscous heating produced by the accretion rate, and the third one is the background radiation field coming from the interstellar medium. The last term is negligible compared to the other, but it was added mainly for convergence of the numerical algorithm, although its influence is less important than the stellar and accretional terms.

The total irradiation heating takes into account the stellar irradiation and the differences in this heating associated to the flaring. Considering that the disk is irradiated by the two sides and using the thin disk assumption, the irradiation received by each side is approximately [Fukue, 2013]:

$$q_{\rm irr} = \sigma_{\rm sb} T_{\rm irr}^4 = T_*^4 \Big[\Big(\frac{R_*}{r} \Big)^2 H_h \Big(\frac{{\rm d}H}{{\rm d}r} - \frac{H}{r} \Big) + \frac{2}{3\pi^2} \Big(\frac{R_*}{r} \Big)^3 \Big]. \tag{3.2}$$

The variable $T_{\rm irr}$ introduced in equation (3.2) is just an "equivalent temperature" for the incoming flux of the irradiation heating at one side of the disk. This heating source has two terms. The first one ($\Big(\frac{R_*}{r} \Big)^2 H_h \Big(\frac{{\rm d}H}{{\rm d}r} - \frac{H}{r} \Big)$ (flaring term) is related to the flaring of the disk ($\frac{{\rm d}H}{{\rm d}r}$) and its local thickness ($\frac{H}{r}$), so it changes with the disk's shape. In the equation (3.2), we have added the factor H_h, that is used by Chiang and Goldreich [1997a] to describe the location of the photosphere in young stars. This phostospheric scale height is proportional

to the scale height of the disk in the model that we constructed. At radius between 1 to 100 AUs, it is considered to be between $4-5$ times the scale height of the disk ($H_h \approx 4-5h$). In particular, our model uses $H_h = 4h$, where h is the scale height of the disk. The second term $\frac{2}{3\pi}\left(\frac{R_*}{r}\right)^3$ (stellar term) is associated to the star's size, a bigger star has more impact heating up the surrounding material as it scales with R_*^3. Because we have assumed a big star radius, this term becomes important at the most inner parts of the disk.

Besides the irradiation heating, we need to add the expression associated to viscous dissipation. The viscous heating in a ring for a standard α disk for each side is [Shakura and Sunyaev, 1973b]:

$$\delta Q^+ = \frac{9}{8}\Sigma\nu\Omega_K^2 2\pi r\delta r. \tag{3.3}$$

Taking the flux energy density of the accretional heat in the equation 3.3, we obtain the expression:

$$q^+ = \frac{9}{8}\Sigma\nu\Omega_K^2. \tag{3.4}$$

.

Different radial and vertical prescriptions can be found depending on the disk structure assumed for the parameters Σ and ν. Those two parameters are more difficult to constrain observationally, so we used the accretion rate instead. This approach was chosen because it diminishes the number of free parameters in our model and it is easier to constrain.

To express the viscous heating as a function of $\dot{M}$, we use the equation that relates the accretion rate with the viscosity and gas surface density for a steady state accretion disk:

$$\nu\Sigma = \frac{\dot{M}}{3\pi}. \tag{3.5}$$

The viscous heat then takes an expression that is a function of the accretion rate and the Keplerian velocity $\Omega_K = \sqrt{GM_*/r^3}$, thus the mass of the YSO. Combining equations (3.4) and (3.5) the final equation for the accretional heating is then the following:

$$q^+_{\rm acc} = \frac{3}{8\pi}\dot{M}\Omega_K^2 = \sigma_{\rm sb}T^4_{\rm acc}. \tag{3.6}$$

In equation (3.6) we introduce $T_{\rm acc}$. It represents just a correspondence between the viscous heating and an " effective accretional temperature". In this case, most of the viscous dissipation will be embedded inside the disk, below of the photosphere. By assuming radiative equilibrium, the energy dissipation will eventually reach the upper layers, heating them up. We have assumed a uniform volume rate of energy dissipation Γ distributed vertically along four scale heights. The viscous heating is multiplied by two, because the term in equation

(3.6) corresponds to only one side of the disk. This means that the viscous energy dissipation per unit volume in our model is:

$$\Gamma(r,z) = \frac{3}{8\pi}(\dot{M}\Omega_K^2)\frac{1}{2h}. \tag{3.7}$$

Equations (3.6) and (3.7) show a linear dependence between the viscous heat and the accretion rate. If we considered a constant accretion rate, we would have a radial dependence of the form $q^+ \propto \Omega_K^2 \propto r^{-3}$. This means that for the outer radius, the irradiation from the star will be much more important than the viscous heating since it decays with $r^{\dot{}2}$ (see equation (3.2)).

We also set a local basal temperature as a background radiation. We set this basal temperature as the one that comes from the interstellar medium or the environment of the star. This background radiation field sets a constant lower limit for the temperature of the disk. The basal temperature is added as another external heat source, as follows:

$$q_{\rm basal} = \sigma_{\rm sb} T_{\rm basal}^4, \tag{3.8}$$

where we set $T_{\rm basal} = 20$ K. However, we notice that the results didn't have major changes using $T_{\rm basal}$ in the range between 10 K and 20 K.

3.2.1.3 Effective Temperature

We define the effective temperature as the one that would match the dust as if it emits as a blackbody considering its attenuation by optical depths effects(at least in the optically thin region). For the optically thick regime we used the brightness temperature as the effective temperature.

According to models done by [Cieza et al., 2016], V883 Ori would have a spectral index of ≈ 2 at the inner ~ 40 AU. This spectral index is typical of blackbody emission, so we assumed that the disk is optically thick at that part. Thus, for the purposes of the modeling, given that the dust is emitting as a blackdoby and its milimeter emission is optically thick at the inner 40 AU, the brightness temperature(Tb) is almost equal to the effective temperature $T_{\rm eff}$.

From the energy conservation equation we obtain the relation for the radiative equilibrium of the disk. The input energy at the surface is the viscous heating from the interior of the disk plus the irradiation heating from the star and what we have called the basal radiation from the medium. The energy output at a certain location is just the emission flux at the dust effective temperature.

$$q^+ + \sigma_{\rm sb} T_{\rm irr}^4 + \sigma_{\rm sb} T_{\rm basal}^4 = \sigma_{\rm sb} T_{\rm eff}^4 \tag{3.9}$$

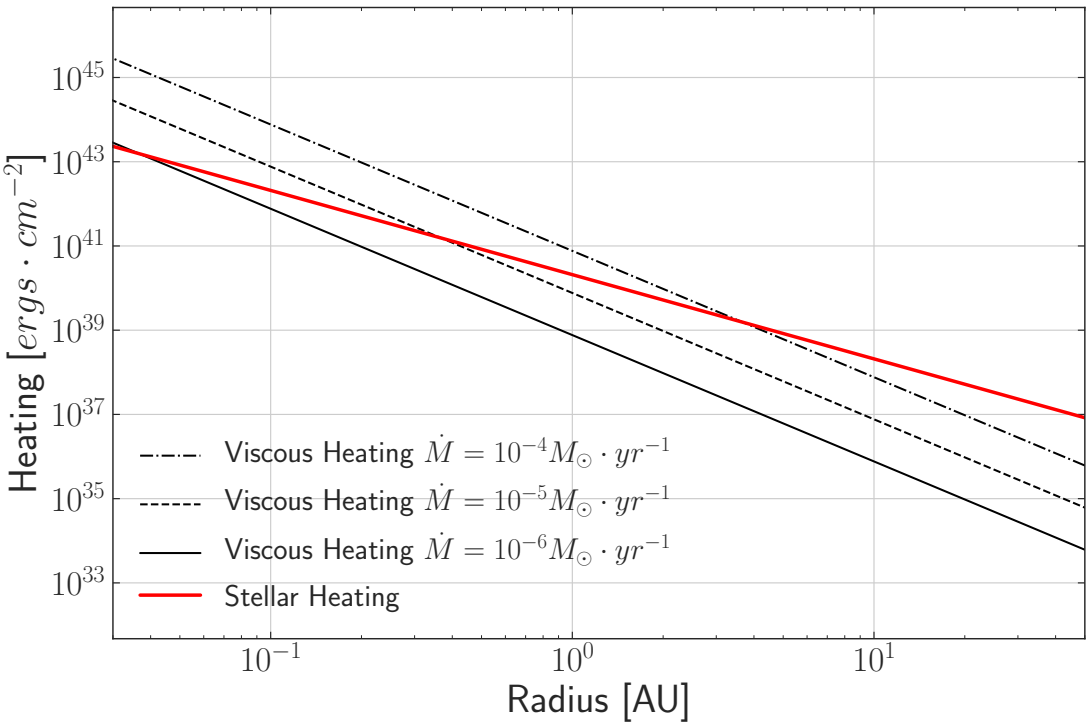

Figure 3.1: Comparison between viscous heating for three different accretion rates constant along the disk and the stellar irradiation heating.

Figure 3.1 shows the comparison between stellar irradiation heating and accretional heating for a star with 10000 K and $R_* = 4R_\odot$. Accretion rates measured for FU Ori outbursts have reached values close to 10^{-4} solar masses per year. When the accretion rate is of the order of 10^{-4} $M_\odot \cdot$ yr^{-1}, the viscous heat overrules any other heat source to distances of the order of AUs. We observe that the viscous dissipation for such high star accretion rate, as the one in V883 Ori ($\approx 3 \cdot 10^{-5}$ $M_\odot \cdot$ yr^{-1}), should play an important role, being predominant close to the star. It is then expected that the viscous dissipation is a heat source that would strongly affect the source emission through changes in the disk morphology, increments of the dust temperature and changes in the dust opacity regimes, i.e, the disk's optical depth.

Following the results obtained by Bell et al. [1997], we expect a self- shadowed disk, starting with a high flared structure caused by the high temperatures in the midplane that enhances the local sound speed. Then, it decays, producing the self-shielded disk. At the outer part of the disk, it is much more flared and much less dense, so we considered it to have an isothermal vertical structure. Since the accretional heating is less important given that it decays rapidly with radius, the outer part of the disk is principally heated by irradiation.

Irradiation and basal heating are not enough to explain the dust temperature measured for V883 Ori, especially at its core. For the optically thick part(at the interior of the snow line), we found that an additional heat source is necessary. Using just those heating sources the intensity doesn't even reach the 1% of the dust emission in the closest 40 AU to the

star. This means that $T^4_{\rm acc} >> T^4_{\rm basal} + T^4_{\rm irr}$. We assumed that the brightness temperature of the emission should match the accretional temperature of the dust within a small margin, meaning that we modeled the dust as it was emitting as a blackbody with $T_{\rm acc}$.

$$B_\nu(Tb) \approx B_\nu(T_{\rm acc})(1 - {\rm e}^{-\tau}) \approx B_\nu(T_{\rm acc}). \tag{3.10}$$

We used the relation (3.10) to quantify $T_{\rm acc}$ from the observations. Then, we used this accretional temperature to solve the accretion rate using the viscous dissipation in eq 3.6. The accretion rate inferred from this brightness temperature is

$$\dot{M} = \frac{8\pi\sigma_{\rm sb}T^4_{\rm acc}}{3\Omega^2_K}. \tag{3.11}$$

With that parameter, we estimate a local surface accretion rate necessary to achieve the dust emission once the irradiation and basal heating have been taking into account. We obtain the final effective temperature considering all the heating terms mentioned in eq (3.9):

$$T^4_{\rm eff} = T^4_{\rm irr} + T^4_{\rm acc} + T^4_{\rm basal} \tag{3.12}$$

3.2.1.4 Midplane Temperature

D'Alessio et al. [2005] predicted temperatures of thousands of Kelvin degrees for the midplane in accretion disks. To calculate the effect of accretional heating in the thermal structure of the disk, the optical depth is needed too, since the dust is the principal responsible of the heat diffusion from the midplane to the surface. From the observations we have the brightness temperature as a constraint between the effective temperature and the optical depth. Our model uses the self-similar solution for the dust surface density expressed in equation (3.1), so we have the dust surface density for each radius, as it was used as an input for this two layers model. In particular, we had to use a gas-to-dust ratio of 0.1 to reproduce the observations, otherwise optical depth of the source is not high enough. We considered the temperature dependent opacity prescription from Bell and Lin [1994] for the heat diffusion in the disk. With this opacity and the dust surface density, the optical depth to the midplane is calculated using $\tau_{\rm mid} = \frac{\kappa\Sigma}{2}$. Once the viscous dissipation is obtained, we calculate the temperature at the midplane using the radiation diffusion equation. More over, the sound speed at the midplane constrains the aspect ratio and the scale height of the disk, given that most of the disk mass is concentrated in that layer. On the other hand, the surface layer is closer to the effective layer for the optically thick region, so it relates with the observed flux from the disk, in this case at a millimeter wavelength ($\lambda = 1.3$ mm).

For the optically thick part, at the inner radius, the disk is much hotter in the midplane (where the viscous heating has been input) than at the effective layer (near the surface), so it will be heated up from the midplane to the surface. We solved the vertical structure of the temperature with the radiative transfer equations for a gray atmosphere in the vertical axis,

as in Hubeny [1990]. Considering $\mu = \cos(\theta)$, with θ the angle of the incident radiation, we define the intensity moments: J_ν as the mean intensity, H_ν the Eddington flux, and K_ν the mean radiation stress, i.e.,

$$J_\nu = \int_{-1}^{1} I_\nu \mathrm{d}\mu, \tag{3.13}$$

$$H_\nu = \int_{-1}^{1} \mu I_\nu \mathrm{d}\mu, \tag{3.14}$$

$$K_\nu = \int_{-1}^{1} \mu^2 I_\nu \mathrm{d}\mu. \tag{3.15}$$

Using the plane-parallel approximation for a thin disk with no scattering term, the radiative transfer equations become:

$$\mu \frac{\mathrm{d}I_\nu}{\mathrm{d}z} = \rho\Big(\frac{j_\nu}{4\pi} - \kappa_\nu I_\nu\Big), \tag{3.16}$$

$$\frac{\mathrm{d}H_\nu}{\mathrm{d}z} = \rho\Big(\frac{j_\nu}{4\pi} - \kappa_\nu J_\nu\Big), \tag{3.17}$$

$$\frac{\mathrm{d}K_\nu}{\mathrm{d}z} = -\rho\kappa_\nu H_\nu, \tag{3.18}$$

where ρ is taken as the gas density, κ_ν the absorption coefficient, and j_ν the dust emissivity. We also considered the Eddington approximation, with an Eddington factor $f_K = K/J = 1/3$. This means:

$$K_\nu = \frac{J_\nu}{3}. \tag{3.19}$$

The energy conservation equation between matter and radiation for a given (r, z),

$$0 = \Gamma(r, z) - \rho(j - 4\pi\kappa_j J), \tag{3.20}$$

allows us to solve the Eddington flux. In equation (3.20) $\Gamma(r, z)$ is the vertical distribution of the viscous heating given by the expression in equation (3.7). Integrating equation (3.20) in the frequency solves equation (3.17).

This means that equation (3.17) is the mean vertical rate of change of the flux, which is $\Gamma(r, z)/4\pi$ (see (3.7)). Integrating the equation (3.17) from the disk surface to the midplane, the following expression is obtained:

$$H(z) = H(0) + \int \frac{\Gamma(z)}{4\pi} \mathrm{d}z = q_{\mathrm{acc}}(2h - (z_{\mathrm{m}} - z)), \tag{3.21}$$

where z_{m} is the midplane of the disk and $H(0)$ is the Eddington flux at the surface. The $H(0)$ is given by the energy that comes from the disk's interior, i.e., the viscous heating. In other words,

$$H(0) = \frac{\sigma_{\mathrm{sb}} T_{\mathrm{acc}}^4}{4\pi}. \tag{3.22}$$

Then, we integrated the equation (3.18) through all frequencies and used the optical depth integrated over frequency $\mathrm{d}\tau = -\rho\kappa \mathrm{d}z$ between the surface($z = 0$) and the midplane layer($z = z_m$), i.e.,

$$\int_{J(0)}^{J(z_{\mathrm{m}})} \mathrm{d}J = 3 \int_0^{z_{\mathrm{m}}} H \rho \kappa_{\mathrm{rs}} \mathrm{d}z. \tag{3.23}$$

Then, equation equation (3.18) becomes:

$$\int \mathrm{d}J = 3 \left(H(0)\tau_{\mathrm{mid}} + \int_{z_{\mathrm{m}}-2h}^{z_{\mathrm{m}}} q_{\mathrm{acc}}(2h - (z_{\mathrm{m}} - z)) \rho \kappa_{\mathrm{rs}} \mathrm{d}z \right). \tag{3.24}$$

We used a gaussian distribution for the vertical structure of the disk, with the scale height as the dispersion, so $\rho(r, z) = \frac{\Sigma(r,z)}{h\sqrt{2\pi}} \exp(-(z - z_{\mathrm{m}})^2/2h^2)$. Solving the integral in the right of equation (3.24) with that dust density distribution, it results in:

$$J(z_{\mathrm{m}}) = J(0) + 3H(0)\tau_{\mathrm{mid}} + \sigma_{\mathrm{sb}} T_{\mathrm{acc}}^4 \tau_{\mathrm{mid}} \frac{3(1 - \mathrm{e}^{-2})}{4\pi\sqrt{2\pi}}. \tag{3.25}$$

We applied the following boundary condition at the surface of the disk., $J(0) = 2H(0) + \frac{\sigma_{\mathrm{sb}} T_{\mathrm{irr}}^4}{\pi} + \frac{\sigma_{\mathrm{sb}} T_{\mathrm{basal}}^4}{\pi}$. The final expression for the midplane temperature is then:

$$T_{\mathrm{mid}}^4 = \frac{3}{4} T_{\mathrm{acc}}^4 \left(\tau_{\mathrm{mid}} + \frac{2}{3} \right) + T_{\mathrm{irr}}^4 + T_{\mathrm{basal}}^4 + T_{\mathrm{acc}}^4 \tau_{\mathrm{mid}} \frac{3(1 - \mathrm{e}^{-2})}{4\sqrt{2\pi}}. \tag{3.26}$$

To calculate the optical depth in the millimeter regime of the inner disk, we used a mean opacity value of $\kappa_{\mathrm{mm}} = 0.02\ \mathrm{cm}^2 \cdot\ \mathrm{gr}^{-1}$ considering only absorption (no scattering) [Hord et al., 2017]. With this, we measured the optical depth for the band 6 continuum observations. We get that the optical depth is much greater than 1 at radius less than 40 AU. The high optical depth at inner radii is showed in Fig 3.6, where τ_{mm} increases as it gets closer to the star. However, for the inner disk $\tau_{\mathrm{mm}} \propto \Sigma_{\mathrm{d}}$, because we have considered κ_{mm} to be constant.

3.2.1.5 Outer disk, Optically Thin Regime

In the outer disk ($\tau_{\rm mm} < 1$) the brightness temperature measured is lower than the temperature of an irradiated disk, thus an optically thin disk is needed, otherwise the temperature from the model would be higher than the physical temperature of the disk. In this zone of the disk, farther out from the star, the main heating source is the irradiation term. Because the accretional heating has become negligible at this part, the hottest layer won't be the midplane, so heat won't diffuse from the center to the surface. Another treatment is needed to find the thermal structure at this region. In this area of the disk, we have assumed that it is vertically isothermal, so the midplane temperature and the surface temperature are considered to be the same.

We measure the optical depth in this region solving the radiative transfer equation $I_\nu = B_\nu(1 - \mathrm{e}^{-\tau_\nu})$, where we know the physical temperature from the passive disk fitting, and the brightness temperature is obtained from ALMA Band 6 observations. The expression for the millimeter optical depth $\tau_{\rm mm}$ is the following equation:

$$\tau = -\ln\Big(1 - \frac{B_\nu(Tb)}{B_\nu(T_{\rm phy})}\Big). \tag{3.27}$$

3.2.1.6 Algorithm Consistency

Initially, we used a self-consistent two layers model as in Chiang and Goldreich [1997a] to find the thermal structure in the disk. We consider just the irradiation term stated in equation (3.2) with a star of $R_* = 4R_\odot$ and a temperature of $T_* = 10000\ K$. Equation (3.2) takes into consideration the effect of both stellar irradiation and the flaring of the disk, i.e. its shape. The $\left(\frac{\mathrm{d}H}{\mathrm{d}r} - \frac{H}{r}\right)$ term states that the flaring could actually cool down the disk when it is self-shadowed, i.e., $\frac{\mathrm{d}H}{\mathrm{d}r} < \frac{H}{r}$. This may occur in this FU-Ori object and it is observable on the data, when the emission decreases and then goes up again at the frontier of the possible snow line location. This radial term shows that the irradiation heating is dependent on both, the local scale height and its radial rate of change. Once we have calculated a midplane temperature, the sound speed changes, so the scale height and the flaring are updated to the new temperature along with the opacity regime, which could strongly change the optical depth. For the algorithm to be consistent, it needs to solve the thermal and flaring structure for the same radius more than one time, because of the interdependence between flaring, temperature and opacity.

The algorithm begins by solving the effective temperature for each radius from the outer part to the inner regions. It starts fitting until the optical depth is $\tau_{\rm mm} \sim 1$.

For the first run, we only considered the irradiation and basal terms. After that, we add the viscous heating term equating the brightness temperature to the accretional temperature for regions with $\tau_{\rm mm} > 1$. Then, the midplane temperature is calculated using the equation (3.26), where the Rosseland mean opacity is calculated from the Bell and Lin [1994] prescription and the dust density is taken from the fit done by [Cieza et al., 2017]. Changing the

temperature produces a change in the scale height and the sound speed, this in turn changes the flaring and aspect ratio, so the temperature varies again. The self-iterative algorithm takes into account the changes in the local flaring, aspect ratio and opacity during each iteration and updates them with the new temperature calculated. After the recalculation with the new midplane temperature is done, the algorithm starts again from the beginning with a new irradiation term that is given by the new flaring and aspect ratio (see eq. (3.2)). The algorithm follows iterating until the shift in temperature is smaller than ≈0.1 K.

Before running the algorithm, we studied its convergence considering different initial outer radii. We found that the algorithm converged at ≈ 150 AU, so using a $r_{\rm out}$=180 AU for the grid is good enough to trace the temperature in the interior of the snow line. The algorithm used a basal temperature of $T_b = 15$ K at the outer radius, as the temperature of the environment of V883 Ori. We used different temperatures for this basal temperature between $T = 10$ K and $T = 20$ K, and it didn't change the results. We set the algorithm to start with a self-iterative loop from the outside(500 AU) to the inside of the disk(outside-in) with an initial flaring index of 1.5 and a initial aspect ratio of 0.13. Then, the algorithm follows solving iteratively until convergence to the inner radius of the observations.

3.2.1.7 Convergence of the outside-in algorithm

We run the algorithm for different outer radii used as starting points in the range between 110 and 10000 AUs. Figure 3.2 shows the convergence of the algorithm for a sample of different outer radiis chosen as starting points. It is observable that for the temperature and the aspect ratio, the algorithm converges very quickly to a stable solution. Inside 100 AU, all of them have already converged. The case for the flaring angle is the one that takes longer to converge and the most variable, so we used this parameter to define the radial grid of the algorithm. Our model starts with a flaring angle of 1.5 at the outer radius of the grid and then converges to a value of 1.15. We decided to define the outer radius of the model at 500 AU, because we observe that it has already converged at nearly 250 AU, and we are interested principally in the modeling of the inner 50 AU.

3.2.2 Radiative Transfer Simulations

The radiative transfer was done using the additional `heatsource.inp` input file for RADMC-3D as it was implemented by Hord et al. [2017]. This component considers an additional heat source in the simulation grid. It includes the amount of energy added by the external heat source at every cell of the grid. We included this extra component using the expression in equation (3.6).

The numerical simulation were run in a numerical grid of $500 \times 256 \times 1$ in (r, θ, ϕ) respectively. The radius cells follow a logarithmic sample. The colatitude coordinate is linearly sampled from 0 to $\frac{\pi}{2}$, with mirror symmetry to the other side of the midplane. We preserved the density structure obtained from the two layers model. In this case, most of the mass is concentrated within a disk geometry, where the gas is vertically distributed with a gaussian

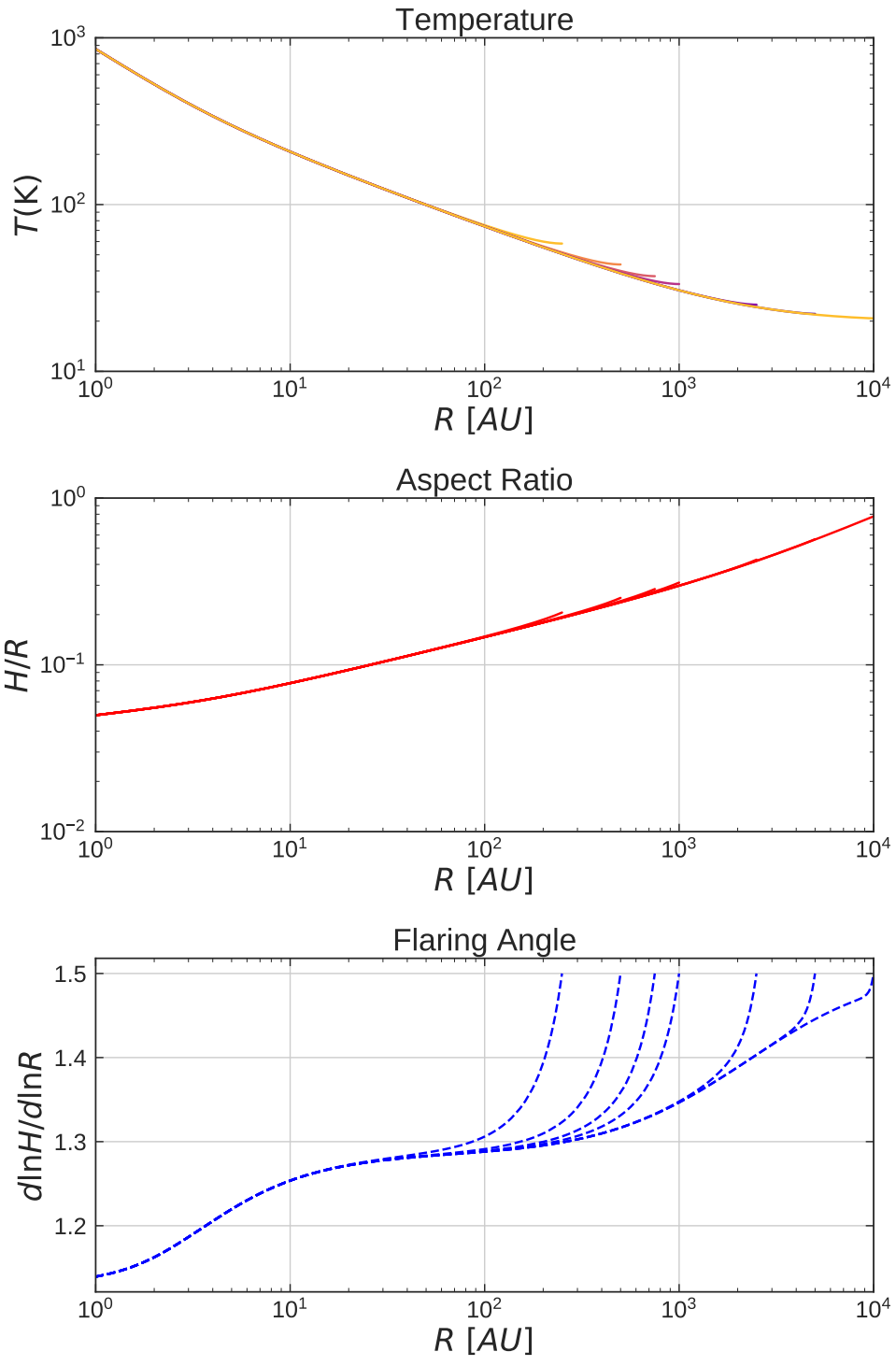

Figure 3.2: Study of the convergence of the algorithm for different outer radius. **Top:** Temperature, **Middle:** Aspect Ratio, **Bottom:** Flaring Angle. The aspect ratio and Temperature converges quickly no matter the initial outer radius given for the algorithm. Flaring angles is more sensible to the starting point of the algorithm, so a initial $r_{\rm out} = 180$ AU was set.

centered at $z = 0$ and the local scale height used as the dispersion of the vertical distribution. To avoid unnecessary numerical cost we used just one cell in azimuth, because the disk is considered to be axisymmetric; hence, we considered isotropic scattering as well. In the radial coordinate, our grid has a starting point at $R_{\rm in} = 0.8$ AUs, and the outer radius is located at $R_{\rm out} = 180$ AUs. The radial grid is not as extended as the two layers model, because it is not necessary for it to converge at a certain radius. We used a variable flaring, modeling the disk with the shadowing effect obtained from the self-consistent fit.

The thermal equilibrium was calculated using 10^8 photon walkers for each run. This number of photon walkers is usually enough to avoid photon noise. We modeled the opacity of the dust with a mixed dust population of 70% of astrosilicates and 30% of amorphous carbons. Dust size distribution follows a standard power law proportional to the dust grain size,

$$f_0(a) \propto a^{-2.5}, \tag{3.28}$$

where a is the size of the dust particle. We set the minimum size for dust particles to be $a_{\rm min} = 0.1$ μ m and the maximum size $a_{\rm max} = 2.5$ mm. Two different simulations were done with a gas-to-dust ratio of 0.01 and 0.1, where we found that the 0.01 does not reproduce correctly the emission and the optical depth of the source, while a gas-to-dust ratio of 0.1 has a better performance for the fit.

In order to make a real comparison with the ALMA band 6 observations, a synthetic continuum image for $\lambda = 1.3$ mm was generated with the radiative transfer code. Then, the resulting image was convolved using the same elliptical beam that the one from the observations. The ALMA elliptical beam has a semi major axis of ≈ 37 mas, a semi minor axis of ≈ 27 mas with a position angle of 52 degrees.

The expression in equation (3.6) is a flux density, the grid defined in the code has three dimensions, so we use the expression in. However, the vertical structure of the viscous heating is unknown, but it did not seem to affect considerably the brightness temperature.

3.3 Results

3.3.1 Effect of Viscous Heating on Temperature

The first consequence of the addition of viscous heating is the increase of gas temperature to values of the order of ~ 1000 K at radius less than 1 AU. Due to the high gas density and the uniform distribution of the heat source vertically in the disk, we obtain an almost constant thermal structure for different colatitudes or heights within the disk. Because a high gas-to-dust ratio was considered, the energy is more easily trapped by all this amount of gas and dust. For lines of sight that are optically thick we expect that the brightness temperature of the dust emission should be similar to the physical temperature of the disk. The two-layers fit results in Fig 3.6 show that the accretional heating is substantially more important at few

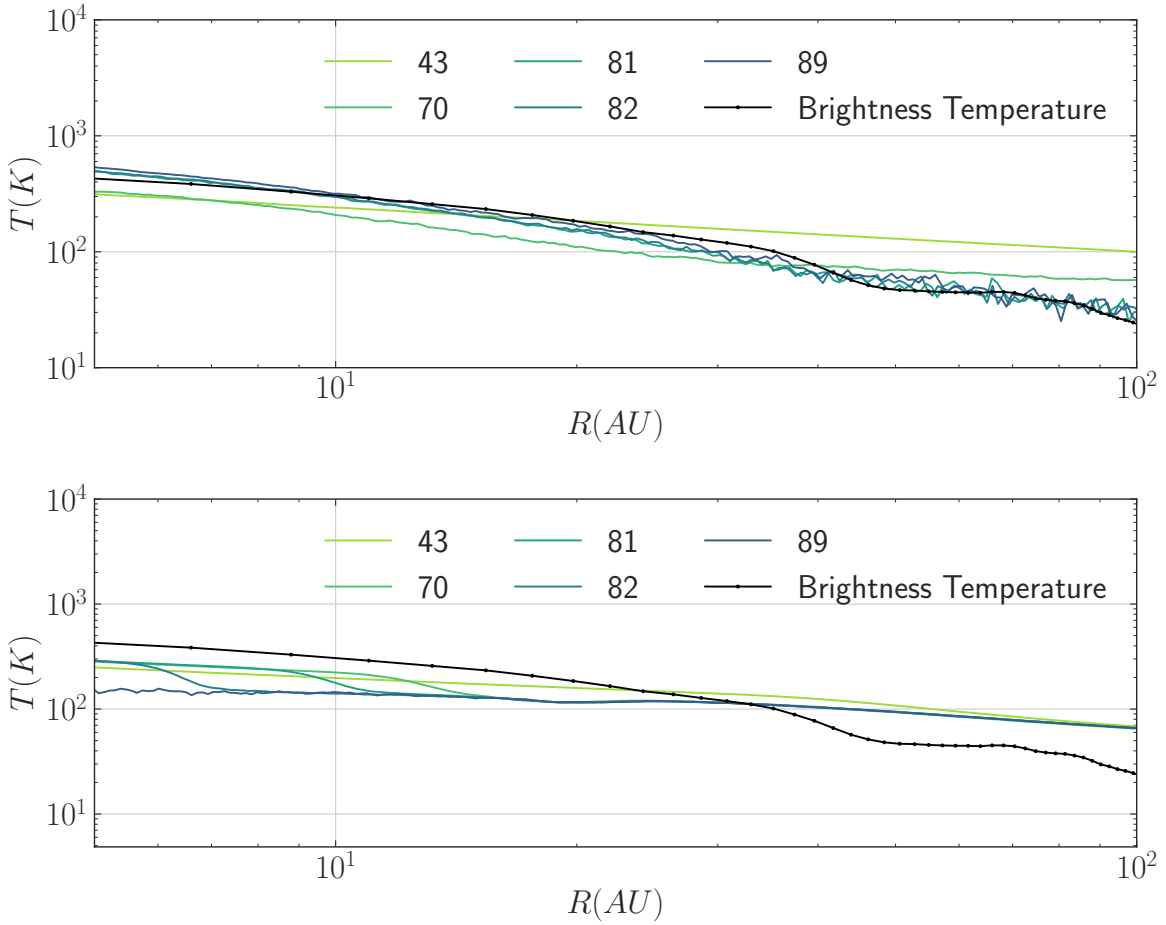

Figure 3.3: Comparison of data in continuum emission with model at $\lambda = 1.3$ mm with and without accretional heating. Profiles represent different colatitudes of the grid, where the angle is measured in degrees from the zenith to the midplane.

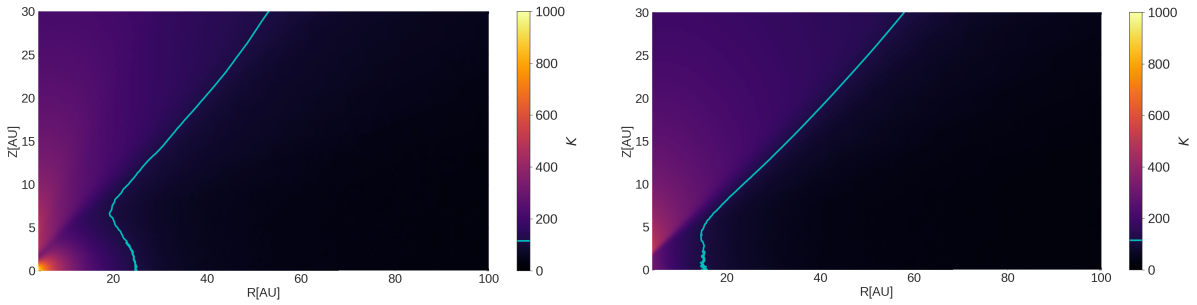

Figure 3.4: Temperature of the dust grid after the radiative transfer simulation. Blue line is an isothermal contour at T=115 K, an approximation for the snow line location. **Left:** Image with accretional heating. **Right**: Image without accretional heating. The simulation with viscous heating shows the shift in the location of the snow line in almost 20 AU.

AUs, so the disk is heated from the midplane to the surface. This phenomenon is stated in Figure 3.3. It shows the thermal profile for a meridional cut with and without accretional heating included, when the accretional heating is included the midplane is hotter than the surface layers. It is observed that the accretional heating increase the temperature at the midplane of the disk as far as 20-26 AU from the star. For the outer part of the disk ($r > 70$ AU), the accretional heating stops to be significant and the dust is almost isothermal and coincident for both cases, so our initial assumption for the outer disk seems reasonable. It is observed that for the simulation without accretional heating the brightness temperature is much higher than the temperature of the dust in the simulation at almost every layer. Considering that the physical temperature of the dust is an upper limit for the brightness temperature (only in very optically thick regimes it is reached), the conclusion of an extra heat source for the best fit of the data, besides irradiation heating, is reinforced. For the simulations with the accretional heating, we see that the brightness temperature is almost equal to the physical temperature of the gas, something that is predicted for the highly optically thick disk modeled.

3.3.2 Radial Dependence of Flaring and Aspect Ratio

The self-consistent solution shows a variable flaring and some self-shadowed parts There is a decline of the aspect ratio after the snow line, where the accretion rate also starts to decrease. The change in the morphology is mainly caused by the decrement in the effect of accretional heating and the change in the opacity regime of the dust grains. The increase in temperature is correlated with a thicker disk, producing the shadowed disk after the snow line. At this zone, the disk starts to cool down, so it becomes thinner and more shielded to the star's radiation by its inner parts. This phenomenon explains the abrupt change in the flaring as the one that is observed in the Fig 3.6. A flaring index less than one causes the cool down of the disk at that part, because it doesn't receive direct irradiation from the star. Furthermore, the aspect ratio and the flaring angle show a plateau between 10 and 40 AU; if the disk is flat, the outwards zones would not be directly irradiated by the star. This zone is where there is an indirect evidence of the snow line location. Additionally, at this location, the predicted accretion wiggles, reaching its peak, after that it starts an abrupt decay. The change in the

disk's accretion rate could mean that there is an accumulation of material at the snow line zone. Such effect would be important to understand the effect of snow lines in dust evolution and planet formation. The $\tau_{\rm mm}$ plot also shows a smooth connection between the two regions of the disk, the optically thick, and the outer oprtically thinner disk, where $\tau_{\rm mm} = 1$ at ~ 40 AU.

3.3.3 Accretion Rate as a function of radius

The accretion rate shown in Fig 3.6 is a local accretion rate. It reaches a peak near $10^{\breve{}3}$ $M_\odot \cdot$ yr^{-1} just at the region of the plateau. Then, the outburst of accretion is not that strong, otherwise the disk would still be very thick, keeping it with a high emission. The fact that the accretion rate is not continuous throughout the disk means that there is a pile-up of material. However, given that V883 Ori is a FU Ori object, it means that V883 Ori has at least gone through an outburst of high accretion. The outburst scenario could explain the differences in the local accretion rate. Fig 3.6 also shows that our measured radial velocity, which given by rate (equation (3.29)), is still lower than the free fall velocity, see equation (equation(3.30)), even at the location where the peak of accretion occurs; hence the gas is not virialize, i.e, it is still dynamically coupled to the dust to produce the viscous dissipation.

$$v_r = \frac{\dot{M}}{2\pi\Sigma r} \tag{3.29}$$

$$v_{\rm ff} = \sqrt{\frac{2GM_*}{r}} \tag{3.30}$$

Integrating the accretional luminosity produced by the viscous dissipation should not be higher than the bolometric luminosity measured for V883-Ori (~ 400 $L_\odot$) with the corrected distance given by Gaia. The integration in this high accretion scenario is done with the equation (3.31) through circular concentric rings at each radius,

$$L(R_1, R_2) = \int_{R_1}^{R_2} 2 \cdot 2\pi R \frac{3}{8\pi} \dot{M}(R) \Omega_K^2(R) {\rm d}R \tag{3.31}$$

The accretional luminosity is $L_{\rm acc} \approx 80$ $L_\odot$, which is less than the 20% of the V883 OriÂ´s bolometric luminosity.

3.3.4 Synthetic Predictions for V883 Ori

Fig. 3.5 exposes the predicted dust continuum images for $\lambda = 1.3$ mm and its match with the bservations, where the accretional heating produces a considerable change in the dust emission. The accretional heating contribution is a centered increment in the intensity that

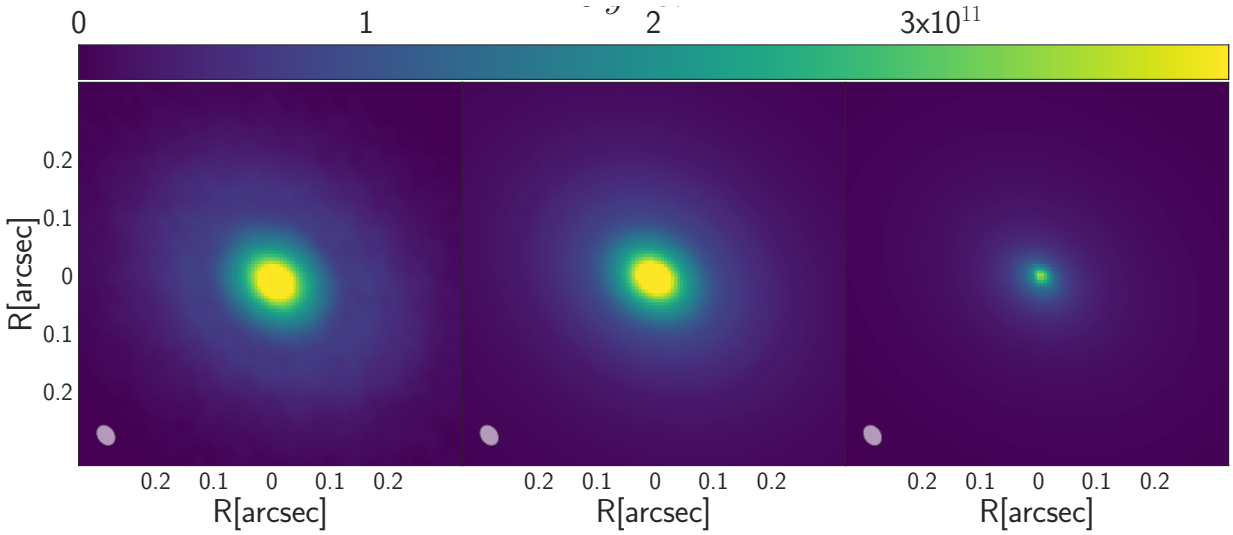

Figure 3.5: Comparison between observations and synthetic images of dust continuum at $\lambda = 1.3mm$ with and without viscous heat in units of Jy/sr. **Left**: Observations, **Center**: Image with viscous heating, **Right**: Image without viscous heating. The images show that the addition of viscous heating matches the centrally peak emission of the observations, whereas the image without viscous heating is not able to match the emission at the inner AUs.

decays considerable at outer radii, producing a steeper radial profile, as the one observed in V883 Ori.

Considering that V883-Ori is one of the most massive YSO measured so far, the best fits, which give a disk mass of $0.7M_{\odot}$ explain the photon noise at inner radius even using a high amount of photon walkers. The dense gas produces the thick opacity regime in this region, so it is most difficult for the photons to advance a step in the grid.

The MCMC fit were done in a model with a singular flaring index. However, this will strongly affects the temperature structure, because the local scale height of the disk is proportional to the temperature and the accretion outburst heats up the gas temperature through the viscous dissipation, thus raising up the disk. As it was already reported by Bell et al. [1997], active disks such as the ones present in FU Ori objects change their flaring index at certain radius, where the accretion decreases. The location of this radius is farther out in the disk with higher accretion rates.

The radiative transfer simulations had a smooth radial profile. Fig 3.8 shows the density structure used as input in RADMC-3D. The plateau is observed at the inner 30 AU, where the disk has a flaring index less than one, thus the aspect ratio is diminishing as it is shown in the plot of Fig. 3.6.

There is a wiggle that has not been reproduced at the frontier of the snowline. It could be associated with a change in the dust density or the dust grains size populations. This phenomenon has been predicted in Banzatti et al. [2015] and in Okuzumi et al. [2016], where they have simulated the density wiggles and dips before and after the snow lines, finding a

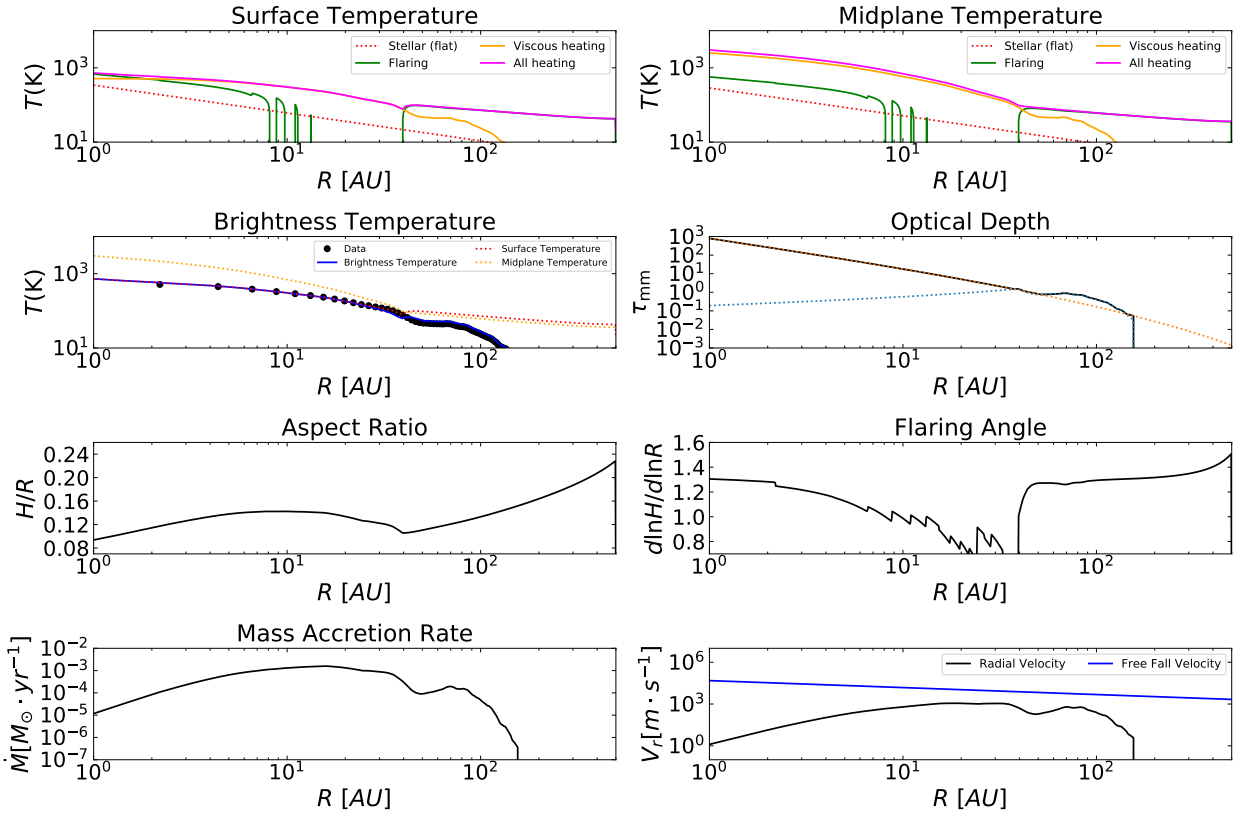

Figure 3.6: Physical conditions of our model. The midplane temperature looks much higher than the surface temperature, given by the optical depth effects. The fast increment in the mm optical depth is observed as getting closer to the star inside the snow line. Flaring angle and the aspect ratio shows the disk shape and the plateau that generates the self-shadowing when the $\dot{M}$ starts to decrease. The mass accretion rate that is measured to match the dust emission is still under the free-fall velocity of gas, so dust and gas are still coupled to generate viscous dissipation.

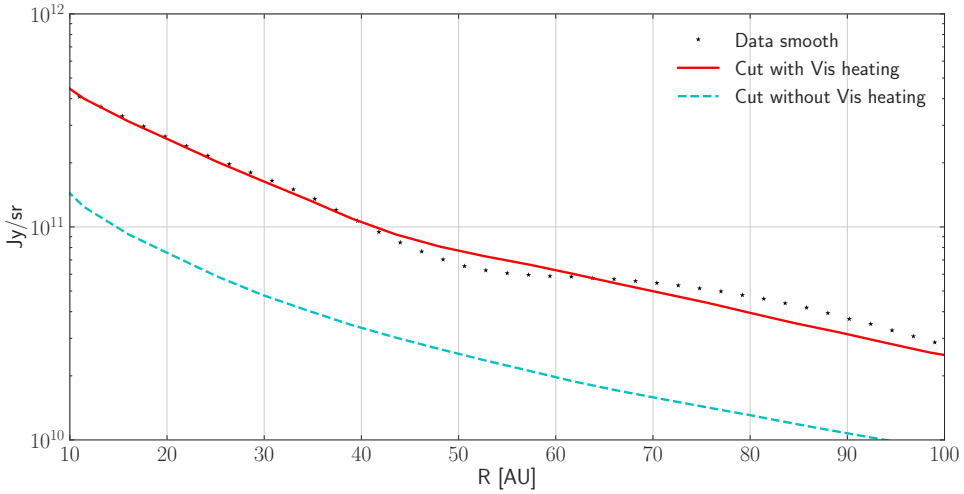

Figure 3.7: Comparison of data in continuum emission with model at $\lambda = 1.3$ mm. The dust distribution match the wiggle between 400 and 60 AU of the intensity profile, and the excess emission at the inner 20 AUs.

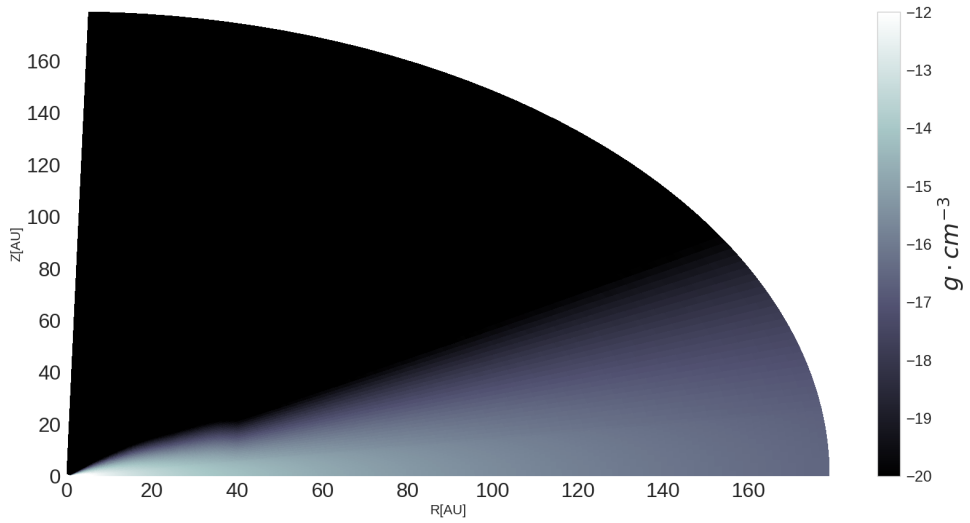

Figure 3.8: Dust density distribution for radiative transfer code. The distribution shows the change and the plateau obtained from the two layers approach, where the disk is shielded to irradiation.

greater concentration of dust just outside of them and a little depletion in the inside. They also predicted a huge increment of the optical depth at the interior of the snow line of water and an accumulation of dust particles at its boundary. The model shows a quick increment at r$\sim$ 26 AU of the optical depth as well. Besides the change in the opacity regime caused by the melting of the ice grains, another possible treatment for this issue could be a differentiation in the dust species. Through the addition of another dust population after the snow line, it would cool down the gas because this produces a local change in the opacity of the dust. An optically thinner disk just inside of the snowline would decrease its emission and thus produce a heating just outside of it. The reason is because the outer layer would be more exposed to stellar irradiation. This dust population composed of larger ice grains could then be the producer of the wiggle in the emission.

3.4 Discussion and Summary

3.4.1 Comparison of the Efficiency between Radial and Vertical Diffusion

In reality the disk diffuses both vertically and radially. However, we only consider vertical diffusion because it is much more efficient than radial diffusion for the disk. in order to explain it, we compared the radial and vertical gradient in temperature. The radial gradient

$$\frac{\mathrm{d}T}{\mathrm{d}r} = \frac{T}{r}\frac{\mathrm{d}\ln T}{\mathrm{d}\ln r} \tag{3.32}$$

can be expressed in terms of the shape of the disk once that is known.

$$T \propto c_s^2, \tag{3.33}$$

so

$$\mathrm{d}\ln T = 2\mathrm{d}\ln c_s. \tag{3.34}$$

From theoretical approaches:

$$c_s = H\Omega, \tag{3.35}$$

thus, combining equations (3.32), (3.34) and (3.35) we obtain the following expression for the radial gradient:

$$\frac{\mathrm{d}T}{\mathrm{d}r} = \frac{T}{r}\Big(\frac{\mathrm{d}\ln\Omega}{\mathrm{d}\ln r} + \frac{\mathrm{d}\ln H}{\mathrm{d}\ln r}\Big). \tag{3.36}$$

Because the terms inside the brackets are of order unity at most ($\frac{\mathrm{d}\ln\Omega}{\mathrm{d}\ln r} = -1.5$ and $\frac{\mathrm{d}\ln H}{\mathrm{d}\ln r}$ is the flaring), $\frac{\mathrm{d}T}{\mathrm{d}r}$ scales with $\frac{T}{2r}$.

For the vertical gradient, the midplane temperature can be approximated as

$$T \sim T_{\mathrm{eff}}\tau^{1/4}, \tag{3.37}$$

then, differentiating with respect to z

$$\frac{\mathrm{d}T}{\mathrm{d}z} = \frac{T_{\mathrm{eff}}}{4}\tau^{-3/4}\frac{\mathrm{d}\tau}{\mathrm{d}z} = \frac{T_{\mathrm{eff}}}{4}\tau^{-3/4}\rho\kappa \tag{3.38}$$

.

If we compare equations (3.38) and (3.36) we obtain that

$$\frac{\mathrm{d}T/\mathrm{d}r}{\mathrm{d}T/\mathrm{d}z} \sim \frac{T_{\mathrm{mid}}}{rT_{\mathrm{eff}}}\frac{\tau^{3/4}}{\rho\kappa}. \tag{3.39}$$

Using the equation (3.37), the approximation fro optical depth $\tau = \frac{\Sigma\kappa}{2}$ in a two layers model and an approximation for the volumetric density as $\rho \sim \frac{\Sigma}{H}$; the following relation results:

$$\frac{\mathrm{d}T/\mathrm{d}r}{\mathrm{d}T/\mathrm{d}z} \sim \frac{H}{r} \tag{3.40}$$

within order unity. Relation (3.40) states that radial diffusion is less efficient than vertical diffusion by a factor of at least five. Although it is important to notice that vertical diffusion is more important than radial diffusion in a disk with a hotter midplane, and as such, its inclusion would not change the macro structure of the disk. However, radial diffusion could be a possible solution for some smaller features in the thermal profile of the disk.

In the comparison with and without viscous heating, it is shown that for FU-Ori objects, the viscous heat has an important role. It changes the thermal profile and the shape of the disk. It is significant in the first AUs, at short radii. There, it increases the temperature to the order of 1000 K and higher values raising up the disk and producing a depression when the accretional heating is no longer important. Despite that, for flared disks, the temperature starts to drop by layers at different distances of the star, as could be expected for the disk shape. On the other hand, for the self-shadowing disk, most of the gas in the outer part of the disk is shielded by the inner part, the accretional heating is now irrelevant and the disk is pretty much isothermal.

The main results are shown in Figure 3.6. It shows that when accretional heating is included, the midplane temperature in the optically thick region is higher than the surface temperature. In fact, accretional heating is the principal heating source at the inner disk,

more important than the stellar or the flaring terms; however, it decays much faster than these terms, so it becomes negligible at the outer disk. On the other hand, for stars with lower accretion rates ($\dot{M} < 10^{-6}$ $M_\odot$ yr^{-1}) the stellar heating is the main source of heating in most of the disk parts, as it is seen in Fig 3.1. In Fig 3.7, the radiative transfer predictions of the model are compared with the observations. Accretional heating provides the extra energy budget to reach the emission levels. It shows that the addition of viscous heat increments the continuum emission as a central source close to the star, changing the radial slope of the thermal profile to a closer match with the observations. There is a presence of the wiggle that is not explained by our model. We associate it with a change in the dust population right before and after the snowline rather than a heating effect. The freezing of water enhances dust growth, since the fragmentation velocity becomes bigger.

In order to reproduce the wiggle in the observations near the snow line, a different dust distribution would be needed. The dust distribution should decrease at a closer radius and increase just outside the snow line. This phenomenon represent an accumulation of dust in the frontier of the snow line produced by the water change of state. Another possible explanation could be the addition of another dust populaton including the effect of the ice grains inward and outward the snow line, the dust stickiness would be increase by the ice, enhancing dust growth. The self-iterative method showed that for passive heating to be able to reproduce the radial profile of the V883 Ori, a giant wall of material would be needed; however, the same wall would shield the outer parts of the disk, so it would be much cooler that what has been measured.

If the Gaia distance to V883 Ori (d$\sim$ 270 pc) would have been considered instead of the one that we used, the qualitative results would not change. It would have mainly changed the values of the disk and star parameters, such as their masses, sizes, and the location of the snowline; it would have been at $\sim$ 26 AU from the star, that distance is still far enough than expected values, so the need of active heating and a hotter midplane remains.

Summarizing, classical passive heat sources are not capable of reproduce the emission profile of the FU-Ori source V883 Ori. An additional heating source is needed. This extra source has the particularity of been significant in the inner part, centrally peak and it decays quickly after a few AUs. High accretion rates is typical of FU Ori objects and their associated accretional heating matches the conditions to be a feasible explanation for the continuum emission profile of a FU Ori object, particularly for V883 Ori.

Chapter 4

Conclusion

This thesis focused on the study of physical properties and conditions in protoplanetary disks. It is known that protoplanetary disks passed through several physical processes during their evolution. The recovery or measurement of those properties is not an easy task given the opacity of both gas and dust. However, millimeter and sub-millimeter wavelengths can trace deep layers in the disk helping us to get a better understanding of the whole planet formation process. This study was divided in two parts; the first one used gas line emission in an intend to recover physical properties and a vertical structure in the disk, along with possible kinematic tracers of planet formation; the second one used dust continuum observations to trace the heating sources in a system going through an outburst of very high accretion. Although both parts used different approaches with distinct specific objectives, the main motivation was the same, how are planets formed?

In Chapter 2, we detailed the first half of this work. We explain the development and modeling of a line diagnostic that measures temperature, turbulent motion and column density in gas line emissions. We started with a benchmark using a parametric disk (toy model) to validate our model. We found that the diagnostic worked for that case, although its better performance is with abundant and optically thin molecular tracers. It seems that numerical error is lower for optically thin tracer, so as long as line shapes is not to degenerate, they become better to measure physical conditions, given that the emission coming from that region is from optically thin tracers. However, using isotopologues or complementing with observations of different gas tracers could be a good idea to improve the performance of the diagnostic. Despite its performance, optically thin tracers emission is dimmer and more difficult to t observe. In our simulations the higher footprint was measured in the most optically thick isotopologue rather than in the thinner ones. Overall, the diagnostic has potential to be applied to detect and characterize the effect of protoplanets in the gas structure of the disk, and it may be applicable to other astronomy areas as well.

In the third Chapter, we have shown the importance of active disk heat sources in Young Stellar Objects. We explored the relevance of viscous heating in the modelling of a FU Ori object, V883 Ori. It is believed that most of low mass stars, just like the Sun, pass through this FU Ori stage, so it is a very common stage during protoplanetary disk evolution.

However, Fu Ori object is a very short stage, so there is only a bunch of them that has been detected so far. To understand the effect of the outburst of accretion on these disks, we developed a self-iterative algorithm that fits the continuum emission and models the disk's radial structure, shape, and its accretion rate. It has been proven that the accretion rate and shape play an important role in the thermal structure, thus the dust emission of the disk. Given that our algorithm details the thermal structure and flow of material on the disk, it can be used to locate the different snow lines in it. Snow lines are key features in the evolution of the disk, they change the chemistry and physics of the disk, playing an important role in planet formation, particularly the water snow line. Usually, the water snow line is inside the inner two AUs, so it is not resolvable with any of the current telescopes; however, viscous heating in FU Oris pushes the water snow line to distances of the order of 10 AUs, which could be resolvable. Therefore, FU Oris are unique sources to understand the role of dust coagulation and water chemistry in planet formation.

Bibliography

Fred C. Adams and Frank H. Shu. Infrared Spectra of Rotating Protostars. , 308:836, September 1986. doi: 10.1086/164555.

Fred C. Adams, Charles J. Lada, and Frank H. Shu. Spectral Evolution of Young Stellar Objects. , 312:788, January 1987. doi: 10.1086/164924.

ALMA Partnership, C. L. Brogan, L. M. Pérez, T. R. Hunter, W. R. F. Dent, A. S. Hales, R. E. Hills, S. Corder, E. B. Fomalont, C. Vlahakis, Y. Asaki, D. Barkats, A. Hirota, J. A. Hodge, C. M. V. Impellizzeri, R. Kneissl, E. Liuzzo, R. Lucas, N. Marcelino, S. Matsushita, K. Nakanishi, N. Phillips, A. M. S. Richards, I. Toledo, R. Aladro, D. Broguiere, J. R. Cortes, P. C. Cortes, D. Espada, F. Galarza, D. Garcia-Appadoo, L. Guzman-Ramirez, E. M. Humphreys, T. Jung, S. Kameno, R. A. Laing, S. Leon, G. Marconi, A. Mignano, B. Nikolic, L.-A. Nyman, M. Radiszcz, A. Remijan, J. A. Rodón, T. Sawada, S. Takahashi, R. P. J. Tilanus, B. Vila Vilaro, L. C. Watson, T. Wiklind, E. Akiyama, E. Chapillon, I. de Gregorio-Monsalvo, J. Di Francesco, F. Gueth, A. Kawamura, C.-F. Lee, Q. Nguyen Luong, J. Mangum, V. Pietu, P. Sanhueza, K. Saigo, S. Takakuwa, C. Ubach, T. van Kempen, A. Wootten, A. Castro-Carrizo, H. Francke, J. Gallardo, J. Garcia, S. Gonzalez, T. Hill, T. Kaminski, Y. Kurono, H.-Y. Liu, C. Lopez, F. Morales, K. Plarre, G. Schieven, L. Testi, L. Videla, E. Villard, P. Andreani, J. E. Hibbard, and K. Tatematsu. The 2014 ALMA Long Baseline Campaign: First Results from High Angular Resolution Observations toward the HL Tau Region. , 808:L3, July 2015. doi: 10.1088/2041-8205/808/1/L3.

P. Andre, D. Ward-Thompson, and M. Barsony. From Prestellar Cores to Protostars: the Initial Conditions of Star Formation. *Protostars and Planets IV*, page 59, May 2000.

P. J. Armitage. Lecture notes on the formation and early evolution of planetary systems. *ArXiv Astrophysics e-prints*, January 2007.

P. J. Armitage. Dynamics of Protoplanetary Disks. , 49:195–236, September 2011. doi: 10.1146/annurev-astro-081710-102521.

Philip J. Armitage. *Astrophysics of Planet Formation*. Cambridge University Press, 2009. doi: 10.1017/CBO9780511802225.

Philip J. Armitage. Dynamics of protoplanetary disks. *Annual Review of Astronomy and Astrophysics*, 49(1):195–236, 2011a. doi: 10.1146/annurev-astro-081710-102521. URL `https://doi.org/10.1146/annurev-astro-081710-102521`.

Philip J. Armitage. Dynamics of protoplanetary disks. *Annual Review of Astronomy and Astrophysics*, 49(1):195–236, 2011b. doi: 10.1146/annurev-astro-081710-102521. URL https://doi.org/10.1146/annurev-astro-081710-102521.

J. Bae, L. Hartmann, Z. Zhu, and C. Gammie. Variable Accretion Outbursts in Protostellar Evolution. , 764:141, February 2013. doi: 10.1088/0004-637X/764/2/141.

J. Bae, L. Hartmann, Z. Zhu, and R. P. Nelson. Accretion Outbursts in Self-gravitating Protoplanetary Disks. , 795:61, November 2014. doi: 10.1088/0004-637X/795/1/61.

A. Banzatti, P. Pinilla, L. Ricci, K. M. Pontoppidan, T. Birnstiel, and F. Ciesla. Direct Imaging of the Water Snow Line at the Time of Planet Formation using Two ALMA Continuum Bands. , 815:L15, December 2015. doi: 10.1088/2041-8205/815/1/L15.

L. Barrière-Fouchet, J.-F. Gonzalez, J. R. Murray, R. J. Humble, and S. T. Maddison. Dust distribution in protoplanetary disks. Vertical settling and radial migration. , 443:185–194, November 2005. doi: 10.1051/0004-6361:20042249.

N. M. Batalha, J. F. Rowe, S. T. Bryson, T. Barclay, C. J. Burke, D. A. Caldwell, J. L. Christiansen, F. Mullally, S. E. Thompson, T. M. Brown, A. K. Dupree, D. C. Fabrycky, E. B. Ford, J. J. Fortney, R. L. Gilliland, H. Isaacson, D. W. Latham, G. W. Marcy, S. N. Quinn, D. Ragozzine, A. Shporer, W. J. Borucki, D. R. Ciardi, T. N. Gautier, III, M. R. Haas, J. M. Jenkins, D. G. Koch, J. J. Lissauer, W. Rapin, G. S. Basri, A. P. Boss, L. A. Buchhave, J. A. Carter, D. Charbonneau, J. Christensen-Dalsgaard, B. D. Clarke, W. D. Cochran, B.-O. Demory, J.-M. Desert, E. Devore, L. R. Doyle, G. A. Esquerdo, M. Everett, F. Fressin, J. C. Geary, F. R. Girouard, A. Gould, J. R. Hall, M. J. Holman, A. W. Howard, S. B. Howell, K. A. Ibrahim, K. Kinemuchi, H. Kjeldsen, T. C. Klaus, J. Li, P. W. Lucas, S. Meibom, R. L. Morris, A. Prša, E. Quintana, D. T. Sanderfer, D. Sasselov, S. E. Seader, J. C. Smith, J. H. Steffen, M. Still, M. C. Stumpe, J. C. Tarter, P. Tenenbaum, G. Torres, J. D. Twicken, K. Uddin, J. Van Cleve, L. Walkowicz, and W. F. Welsh. Planetary Candidates Observed by Kepler. III. Analysis of the First 16 Months of Data. , 204:24, February 2013. doi: 10.1088/0067-0049/204/2/24.

K. R. Bell and D. N. C. Lin. Using FU Orionis outbursts to constrain self-regulated protostellar disk models. , 427:987–1004, June 1994. doi: 10.1086/174206.

K. R. Bell, P. M. Cassen, H. H. Klahr, and T. Henning. The Structure and Appearance of Protostellar Accretion Disks: Limits on Disk Flaring. , 486:372–387, September 1997. doi: 10.1086/304514.

P. Benítez-Llambay and F. S. Masset. FARGO3D: A New GPU-oriented MHD Code. , 223: 11, March 2016. doi: 10.3847/0067-0049/223/1/11.

B. Bitsch, A. Crida, A. Morbidelli, W. Kley, and I. Dobbs-Dixon. Stellar irradiated discs and implications on migration of embedded planets. I. Equilibrium discs. , 549:A124, January 2013. doi: 10.1051/0004-6361/201220159.

B. Bitsch, A. Morbidelli, E. Lega, and A. Crida. Stellar irradiated discs and implications on migration of embedded planets. II. Accreting-discs. , 564:A135, April 2014. doi: 10.1051/

0004-6361/201323007.

B. Bitsch, A. Johansen, M. Lambrechts, and A. Morbidelli. The structure of protoplanetary discs around evolving young stars. , 575:A28, March 2015. doi: 10.1051/0004-6361/201424964.

Y. Boehler, E. Weaver, A. Isella, L. Ricci, C. Grady, J. Carpenter, and L. Perez. A Close-up View of the Young Circumbinary Disk HD 142527. , 840:60, May 2017. doi: 10.3847/1538-4357/aa696c.

A. C. Boley, M. A. Morris, and E. B. Ford. Overcoming the Meter Barrier and the Formation of Systems with Tightly Packed Inner Planets (STIPs). , 792, September 2014. doi: 10.1088/2041-8205/792/2/L27.

W. J. Borucki, D. Koch, G. Basri, N. Batalha, T. Brown, D. Caldwell, J. Caldwell, J. Christensen-Dalsgaard, W. D. Cochran, E. DeVore, E. W. Dunham, A. K. Dupree, T. N. Gautier, J. C. Geary, R. Gilliland, A. Gould, S. B. Howell, J. M. Jenkins, Y. Kondo, D. W. Latham, G. W. Marcy, S. Meibom, H. Kjeldsen, J. J. Lissauer, D. G. Monet, D. Morrison, D. Sasselov, J. Tarter, A. Boss, D. Brownlee, T. Owen, D. Buzasi, D. Charbonneau, L. Doyle, J. Fortney, E. B. Ford, M. J. Holman, S. Seager, J. H. Steffen, W. F. Welsh, J. Rowe, H. Anderson, L. Buchhave, D. Ciardi, L. Walkowicz, W. Sherry, E. Horch, H. Isaacson, M. E. Everett, D. Fischer, G. Torres, J. A. Johnson, M. Endl, P. MacQueen, S. T. Bryson, J. Dotson, M. Haas, J. Kolodziejczak, J. Van Cleve, H. Chandrasekaran, J. D. Twicken, E. V. Quintana, B. D. Clarke, C. Allen, J. Li, H. Wu, P. Tenenbaum, E. Verner, F. Bruhweiler, J. Barnes, and A. Prsa. Kepler Planet-Detection Mission: Introduction and First Results. *Science*, 327:977, February 2010. doi: 10.1126/science.1185402.

S. Bruderer. Survival of molecular gas in cavities of transition disks. I. CO. , 559:A46, November 2013. doi: 10.1051/0004-6361/201321171.

S. Casassus. Resolved Observations of Transition Disks. , 33:e013, April 2016. doi: 10.1017/pasa.2016.7.

E. I. Chiang and P. Goldreich. Spectral Energy Distributions of T Tauri Stars with Passive Circumstellar Disks. , 490:368–376, November 1997a. doi: 10.1086/304869.

E. I. Chiang and P. Goldreich. Spectral Energy Distributions of T Tauri Stars with Passive Circumstellar Disks. , 490:368–376, November 1997b. doi: 10.1086/304869.

L. A. Cieza, S. Casassus, J. Tobin, S. P. Bos, J. P. Williams, S. Perez, Z. Zhu, C. Caceres, H. Canovas, M. M. Dunham, A. Hales, J. L. Prieto, D. A. Principe, M. R. Schreiber, D. Ruiz-Rodriguez, and A. Zurlo. Imaging the water snow-line during a protostellar outburst. , 535:258–261, July 2016. doi: 10.1038/nature18612.

L. A. Cieza, D. Ruiz-Rodriguez, S. Perez, S. Casassus, J. P. Williams, A. Zurlo, D. A. Principe, A. Hales, J. L. Prieto, J. J. Tobin, Z. Zhu, and S. Marino. The ALMA early science view of FUor/EXor objects - V: continuum disc masses and sizes. *ArXiv e-prints*, November 2017.

P. D'Alessio, N. Calvet, and D. S. Woolum. Thermal Structure of Protoplanetary Disks. In A. N. Krot, E. R. D. Scott, and B. Reipurth, editors, *Chondrites and the Protoplanetary Disk*, volume 341 of *Astronomical Society of the Pacific Conference Series*, page 353, December 2005.

Paola D'Alessio, Jorge CantÃP, Nuria Calvet, and Susana Lizano. Accretion disks around young objects. i. the detailed vertical structure. *The Astrophysical Journal*, 500(1):411, 1998. URL `http://stacks.iop.org/0004-637X/500/i=1/a=411`.

Nicolas Dauphas and Marc Chaussidon. A perspective from extinct radionuclides on a young stellar object: The sun and its accretion disk. *Annual Review of Earth and Planetary Sciences*, 39(1):351–386, 2011. doi: 10.1146/annurev-earth-040610-133428. URL `https://doi.org/10.1146/annurev-earth-040610-133428`.

Ruobing Dong, Sheng-yuan Liu, and Jeffrey Fung. Observational Signatures of Planets in Protoplanetary Disks: Planet- Induced Line Broadening in Gaps. *arXiv e-prints*, art. arXiv:1811.09629, November 2018.

F. Du, E. A. Bergin, M. Hogerheijde, E. F. van Dishoeck, G. Blake, S. Bruderer, I. Cleeves, C. Dominik, D. Fedele, D. C. Lis, G. Melnick, D. Neufeld, J. Pearson, and U. Yıldız. Survey of Cold Water Lines in Protoplanetary Disks: Indications of Systematic Volatile Depletion. , 842:98, June 2017. doi: 10.3847/1538-4357/aa70ee.

C. P. Dullemond, A. Juhasz, A. Pohl, F. Sereshti, R. Shetty, T. Peters, B. Commercon, and M. Flock. RADMC-3D: A multi-purpose radiative transfer tool. Astrophysics Source Code Library, February 2012.

Michael M. Dunham and Eduard I. Vorobyov. Resolving the luminosity problem in low-mass star formation. *The Astrophysical Journal*, 747(1):52, 2012. URL `http://stacks.iop.org/0004-637X/747/i=1/a=52`.

N. J. Evans, II, M. M. Dunham, J. K. Jørgensen, M. L. Enoch, B. Merín, E. F. van Dishoeck, J. M. Alcalá, P. C. Myers, K. R. Stapelfeldt, T. L. Huard, L. E. Allen, P. M. Harvey, T. van Kempen, G. A. Blake, D. W. Koerner, L. G. Mundy, D. L. Padgett, and A. I. Sargent. The Spitzer c2d Legacy Results: Star-Formation Rates and Efficiencies; Evolution and Lifetimes. , 181:321–350, April 2009. doi: 10.1088/0067-0049/181/2/321.

D. Fedele, M. Carney, M. R. Hogerheijde, C. Walsh, A. Miotello, P. Klaassen, S. Bruderer, T. Henning, and E. F. van Dishoeck. ALMA unveils rings and gaps in the protoplanetary system <ASTROBJ>HD 169142</ASTROBJ>: signatures of two giant protoplanets. , 600:A72, April 2017. doi: 10.1051/0004-6361/201629860.

Kevin M. Flaherty, A. Meredith Hughes, Richard Teague, Jacob B. Simon, Sean M. Andrews, and David J. Wilner. Turbulence in the TW Hya Disk. , 856:117, April 2018. doi: 10.3847/1538-4357/aab615.

M. Flock, R. P. Nelson, N. J. Turner, G. H.-M. Bertrang, C. Carrasco-González, T. Henning, W. Lyra, and R. Teague. Radiation Hydrodynamical Turbulence in Protoplanetary Disks: Numerical Models and Observational Constraints. , 850:131, December 2017. doi: 10.

3847/1538-4357/aa943f.

J. Frank, A. King, and D. J. Raine. *Accretion Power in Astrophysics: Third Edition*. January 2002.

Jun Fukue. Radiative transfer in protoplanetary disks under irradiation by the protostar. *Progress of Theoretical and Experimental Physics*, 2013(5):053E02, 2013. doi: 10.1093/ptep/ptt028. URL `http://dx.doi.org/10.1093/ptep/ptt028`.

Gaia Collaboration, T. Prusti, J. H. J. de Bruijne, A. G. A. Brown, A. Vallenari, C. Babusiaux, C. A. L. Bailer-Jones, U. Bastian, M. Biermann, D. W. Evans, L. Eyer, F. Jansen, C. Jordi, S. A. Klioner, U. Lammers, L. Lindegren, X. Luri, F. Mignard, D. J. Milligan, C. Panem, V. Poinsignon, D. Pourbaix, S. Randich, G. Sarri, P. Sartoretti, H. I. Siddiqui, C. Soubiran, V. Valette, F. van Leeuwen, N. A. Walton, C. Aerts, F. Arenou, M. Cropper, R. Drimmel, E. Høg, D. Katz, M. G. Lattanzi, W. O'Mullane, E. K. Grebel, A. D. Holland, C. Huc, X. Passot, L. Bramante, C. Cacciari, J. Castañeda, L. Chaoul, N. Cheek, F. De Angeli, C. Fabricius, R. Guerra, J. Hernández, A. Jean-Antoine-Piccolo, E. Masana, R. Messineo, N. Mowlavi, K. Nienartowicz, D. Ordóñez- Blanco, P. Panuzzo, J. Portell, P. J. Richards, M. Riello, G. M. Seabroke, P. Tanga, F. Thévenin, J. Torra, S. G. Els, G. Gracia-Abril, G. Comoretto, M. Garcia-Reinaldos, T. Lock, E. Mercier, M. Altmann, R. Andrae, T. L. Astraatmadja, I. Bellas-Velidis, K. Benson, J. Berthier, R. Blomme, G. Busso, B. Carry, A. Cellino, G. Clementini, S. Cowell, O. Creevey, J. Cuypers, M. Davidson, J. De Ridder, A. de Torres, L. Delchambre, A. Dell'Oro, C. Ducourant, Y. Frémat, M. García-Torres, E. Gosset, J. L. Halbwachs, N. C. Hambly, D. L. Harrison, M. Hauser, D. Hestroffer, S. T. Hodgkin, H. E. Huckle, A. Hutton, G. Jasniewicz, S. Jordan, M. Kontizas, A. J. Korn, A. C. Lanzafame, M. Manteiga, A. Moitinho, K. Muinonen, J. Osinde, E. Pancino, T. Pauwels, J. M. Petit, A. Recio-Blanco, A. C. Robin, L. M. Sarro, C. Siopis, M. Smith, K. W. Smith, A. Sozzetti, W. Thuillot, W. van Reeven, Y. Viala, U. Abbas, A. Abreu Aramburu, S. Accart, J. J. Aguado, P. M. Allan, W. Allasia, G. Altavilla, M. A. Álvarez, J. Alves, R. I. Anderson, A. H. Andrei, E. Anglada Varela, E. Antiche, T. Antoja, S. Antón, B. Arcay, A. Atzei, L. Ayache, N. Bach, S. G. Baker, L. Balaguer-Núñez, C. Barache, C. Barata, A. Barbier, F. Barblan, M. Baroni, D. Barrado y Navascués, M. Barros, M. A. Barstow, U. Becciani, M. Bellazzini, G. Bellei, A. Bello García, V. Belokurov, P. Bendjoya, A. Berihuete, L. Bianchi, O. Bienaymé, F. Billebaud, N. Blagorodnova, S. Blanco-Cuaresma, T. Boch, A. Bombrun, R. Borrachero, S. Bouquillon, G. Bourda, H. Bouy, A. Bragaglia, M. A. Breddels, N. Brouillet, T. Brüsemeister, B. Bucciarelli, F. Budnik, P. Burgess, R. Burgon, A. Burlacu, D. Busonero, R. Buzzi, E. Caffau, J. Cambras, H. Campbell, R. Cancelliere, T. Cantat-Gaudin, T. Carlucci, J. M. Carrasco, M. Castellani, P. Charlot, J. Charnas, P. Charvet, F. Chassat, A. Chiavassa, M. Clotet, G. Cocozza, R. S. Collins, P. Collins, G. Costigan, F. Crifo, N. J. G. Cross, M. Crosta, C. Crowley, C. Dafonte, Y. Damerdji, A. Dapergolas, P. David, M. David, P. De Cat, F. de Felice, P. de Laverny, F. De Luise, R. De March, D. de Martino, R. de Souza, J. Debosscher, E. del Pozo, M. Delbo, A. Delgado, H. E. Delgado, F. di Marco, P. Di Matteo, S. Diakite, E. Distefano, C. Dolding, S. Dos Anjos, P. Drazinos, J. Durán, Y. Dzigan, E. Ecale, B. Edvardsson, H. Enke, M. Erdmann, D. Escolar, M. Espina, N. W. Evans, G. Eynard Bontemps, C. Fabre, M. Fabrizio, S. Faigler, A. J. Falcão, M. Farràs Casas, F. Faye, L. Federici, G. Fedorets, J. Fernández-Hernández, P. Fernique, A. Fienga, F. Figueras, F. Filippi,

K. Findeisen, A. Fonti, M. Fouesneau, E. Fraile, M. Fraser, J. Fuchs, R. Furnell, M. Gai, S. Galleti, L. Galluccio, D. Garabato, F. García-Sedano, P. Garé, A. Garofalo, N. Garralda, P. Gavras, J. Gerssen, R. Geyer, G. Gilmore, S. Girona, G. Giuffrida, M. Gomes, A. González-Marcos, J. González-Núñez, J. J. González-Vidal, M. Granvik, A. Guerrier, P. Guillout, J. Guiraud, A. Gúrpide, R. Gutiérrez-Sánchez, L. P. Guy, R. Haigron, D. Hatzidimitriou, M. Haywood, U. Heiter, A. Helmi, D. Hobbs, W. Hofmann, B. Holl, G. Holland, J. A. S. Hunt, A. Hypki, V. Icardi, M. Irwin, G. Jevardat de Fombelle, P. Jofré, P. G. Jonker, A. Jorissen, F. Julbe, A. Karampelas, A. Kochoska, R. Kohley, K. Kolenberg, E. Kontizas, S. E. Koposov, G. Kordopatis, P. Koubsky, A. Kowalczyk, A. Krone-Martins, M. Kudryashova, I. Kull, R. K. Bachchan, F. Lacoste-Seris, A. F. Lanza, J. B. Lavigne, C. Le Poncin-Lafitte, Y. Lebreton, T. Lebzelter, S. Leccia, N. Leclerc, I. Lecoeur-Taibi, V. Lemaitre, H. Lenhardt, F. Leroux, S. Liao, E. Licata, H. E. P. Lindstrøm, T. A. Lister, E. Livanou, A. Lobel, W. Löffler, M. López, A. Lopez-Lozano, D. Lorenz, T. Loureiro, I. MacDonald, T. Magalhães Fernandes, S. Managau, R. G. Mann, G. Mantelet, O. Marchal, J. M. Marchant, M. Marconi, J. Marie, S. Marinoni, P. M. Marrese, G. Marschalkó, D. J. Marshall, J. M. Martín-Fleitas, M. Martino, N. Mary, G. Matijevič, T. Mazeh, P. J. McMillan, S. Messina, A. Mestre, D. Michalik, N. R. Millar, B. M. H. Miranda, D. Molina, R. Molinaro, M. Molinaro, L. Molnár, M. Moniez, P. Montegriffo, D. Monteiro, R. Mor, A. Mora, R. Morbidelli, T. Morel, S. Morgenthaler, T. Morley, D. Morris, A. F. Mulone, T. Muraveva, I. Musella, J. Narbonne, G. Nelemans, L. Nicastro, L. Noval, C. Ordénovic, J. Ordieres-Meré, P. Osborne, C. Pagani, I. Pagano, F. Pailler, H. Palacin, L. Palaversa, P. Parsons, T. Paulsen, M. Pecoraro, R. Pedrosa, H. Pentikäinen, J. Pereira, B. Pichon, A. M. Piersimoni, F. X. Pineau, E. Plachy, G. Plum, E. Poujoulet, A. Prša, L. Pulone, S. Ragaini, S. Rago, N. Rambaux, M. Ramos-Lerate, P. Ranalli, G. Rauw, A. Read, S. Regibo, F. Renk, C. Reylé, R. A. Ribeiro, L. Rimoldini, V. Ripepi, A. Riva, G. Rixon, M. Roelens, M. Romero-Gómez, N. Rowell, F. Royer, A. Rudolph, L. Ruiz-Dern, G. Sadowski, T. Sagristà Sellés, J. Sahlmann, J. Salgado, E. Salguero, M. Sarasso, H. Savietto, A. Schnorhk, M. Schultheis, E. Sciacca, M. Segol, J. C. Segovia, D. Segransan, E. Serpell, I. C. Shih, R. Smareglia, R. L. Smart, C. Smith, E. Solano, F. Solitro, R. Sordo, S. Soria Nieto, J. Souchay, A. Spagna, F. Spoto, U. Stampa, I. A. Steele, H. Steidelmüller, C. A. Stephenson, H. Stoev, F. F. Suess, M. Süveges, J. Surdej, L. Szabados, E. Szegedi-Elek, D. Tapiador, F. Taris, G. Tauran, M. B. Taylor, R. Teixeira, D. Terrett, B. Tingley, S. C. Trager, C. Turon, A. Ulla, E. Utrilla, G. Valentini, A. van Elteren, E. Van Hemelryck, M. van Leeuwen, M. Varadi, A. Vecchiato, J. Veljanoski, T. Via, D. Vicente, S. Vogt, H. Voss, V. Votruba, S. Voutsinas, G. Walmsley, M. Weiler, K. Weingrill, D. Werner, T. Wevers, G. Whitehead, Ł. Wyrzykowski, A. Yoldas, M. Žerjal, S. Zucker, C. Zurbach, T. Zwitter, A. Alecu, M. Allen, C. Allende Prieto, A. Amorim, G. Anglada-Escudé, V. Arsenijevic, S. Azaz, P. Balm, M. Beck, H. H. Bernstein, L. Bigot, A. Bijaoui, C. Blasco, M. Bonfigli, G. Bono, S. Boudreault, A. Bressan, S. Brown, P. M. Brunet, P. Bunclark, R. Buonanno, A. G. Butkevich, C. Carret, C. Carrion, L. Chemin, F. Chéreau, L. Corcione, E. Darmigny, K. S. de Boer, P. de Teodoro, P. T. de Zeeuw, C. Delle Luche, C. D. Domingues, P. Dubath, F. Fodor, B. Frézouls, A. Fries, D. Fustes, D. Fyfe, E. Gallardo, J. Gallegos, D. Gardiol, M. Gebran, A. Gomboc, A. Gómez, E. Grux, A. Gueguen, A. Heyrovsky, J. Hoar, G. Iannicola, Y. Isasi Parache, A. M. Janotto, E. Joliet, A. Jonckheere, R. Keil, D. W. Kim, P. Klagyivik, J. Klar, J. Knude, O. Kochukhov, I. Kolka, J. Kos, A. Kutka, V. Lainey, D. LeBouquin, C. Liu, D. Loreggia, V. V. Makarov, M. G. Marseille, C. Martayan, O. Martinez-Rubi, B. Massart, F. Meynadier, S. Mignot, U. Munari, A. T.

Nguyen, T. Nordlander, P. Ocvirk, K. S. O'Flaherty, A. Olias Sanz, P. Ortiz, J. Osorio, D. Oszkiewicz, A. Ouzounis, M. Palmer, P. Park, E. Pasquato, C. Peltzer, J. Peralta, F. Péturaud, T. Pieniluoma, E. Pigozzi, J. Poels, G. Prat, T. Prod'homme, F. Raison, J. M. Rebordao, D. Risquez, B. Rocca-Volmerange, S. Rosen, M. I. Ruiz-Fuertes, F. Russo, S. Sembay, I. Serraller Vizcaino, A. Short, A. Siebert, H. Silva, D. Sinachopoulos, E. Slezak, M. Soffel, D. Sosnowska, V. Straižys, M. ter Linden, D. Terrell, S. Theil, C. Tiede, L. Troisi, P. Tsalmantza, D. Tur, M. Vaccari, F. Vachier, P. Valles, W. Van Hamme, L. Veltz, J. Virtanen, J. M. Wallut, R. Wichmann, M. I. Wilkinson, H. Ziaeepour, and S. Zschocke. The Gaia mission. , 595:A1, November 2016. doi: 10.1051/0004-6361/201629272.

Gaia Collaboration, Brown, A. G. A., Vallenari, A., Prusti, T., de Bruijne, J. H. J., and et al. Gaia data release 2. summary of the contents and survey properties. *A&A*, 2018. doi: 10.1051/0004-6361/201833051. URL `https://doi.org/10.1051/0004-6361/201833051`.

Charles F. Gammie. Layered Accretion in T Tauri Disks. , 457:355, January 1996. doi: 10.1086/176735.

Thomas P. Greene, Bruce A. Wilking, Philippe Andre, Erick T. Young, and Charles J. Lada. Further Mid-Infrared Study of the rho Ophiuchi Cloud Young Stellar Population: Luminosities and Masses of Pre–Main-Sequence Stars. , 434:614, October 1994. doi: 10.1086/174763.

Erik Gullbring, Lee Hartmann, Cesar Briceño, and Nuria Calvet. Disk Accretion Rates for T Tauri Stars. , 492:323–341, January 1998. doi: 10.1086/305032.

D. Harsono, S. Bruderer, and E. F. van Dishoeck. Volatile snowlines in embedded disks around low-mass protostars. , 582:A41, October 2015. doi: 10.1051/0004-6361/201525966.

L. Hartmann and J. Bae. How do T Tauri stars accrete? , 474:88–94, February 2018. doi: 10.1093/mnras/stx2775.

L. Hartmann, G. Herczeg, and N. Calvet. Accretion onto Pre-Main-Sequence Stars. , 54: 135–180, September 2016. doi: 10.1146/annurev-astro-081915-023347.

Lee Hartmann and Scott J. Kenyon. The fu orionis phenomenon. *Annual Review of Astronomy and Astrophysics*, 34(1):207–240, 1996. doi: 10.1146/annurev.astro.34.1.207. URL `https://doi.org/10.1146/annurev.astro.34.1.207`.

Lee Hartmann, , and Scott J. Kenyon. The fu orionis phenomenon. *Annual Review of Astronomy and Astrophysics*, 34(1):207–240, 1996. doi: 10.1146/annurev.astro.34.1.207. URL `https://doi.org/10.1146/annurev.astro.34.1.207`.

T. J. Haworth, J. D. Ilee, D. H. Forgan, S. Facchini, D. J. Price, D. M. Boneberg, R. A. Booth, C. J. Clarke, J.-F. Gonzalez, M. A. Hutchison, I. Kamp, G. Laibe, W. Lyra, F. Meru, S. Mohanty, O. Panić, K. Rice, T. Suzuki, R. Teague, C. Walsh, P. Woitke, and Community authors. Grand Challenges in Protoplanetary Disc Modelling. , 33:e053, October 2016. doi: 10.1017/pasa.2016.45.

G. H. Herbig. Eruptive phenomena in early stellar evolution. , 217:693–715, November 1977.

doi: 10.1086/155615.

B. Hord, W. Lyra, M. Flock, N. J. Turner, and M.-M. Mac Low. On Shocks Driven by High-mass Planets in Radiatively Inefficient Disks. III. Observational Signatures in Thermal Emission and Scattered Light. , 849:164, November 2017. doi: 10.3847/1538-4357/aa8fcf.

S. B. Howell, C. Sobeck, M. Haas, M. Still, T. Barclay, F. Mullally, J. Troeltzsch, S. Aigrain, S. T. Bryson, D. Caldwell, W. J. Chaplin, W. D. Cochran, D. Huber, G. W. Marcy, A. Miglio, J. R. Najita, M. Smith, J. D. Twicken, and J. J. Fortney. The K2 Mission: Characterization and Early Results. , 126:398, April 2014. doi: 10.1086/676406.

C. X. Huang, J. Burt, A. Vanderburg, M. N. Günther, A. Shporer, J. A. Dittmann, J. N. Winn, R. Wittenmyer, L. Sha, S. R. Kane, G. R. Ricker, R. K. Vanderspek, D. W. Latham, S. Seager, J. M. Jenkins, D. A. Caldwell, K. A. Collins, N. Guerrero, J. C. Smith, S. N. Quinn, S. Udry, F. Pepe, F. Bouchy, D. Ségransan, C. Lovis, D. Ehrenreich, M. Marmier, M. Mayor, B. Wohler, K. Haworth, E. H. Morgan, M. Fausnaugh, D. R. Ciardi, J. Christiansen, D. Charbonneau, D. Dragomir, D. Deming, A. Glidden, A. M. Levine, P. R. McCullough, L. Yu, N. Narita, T. Nguyen, T. Morton, J. Pepper, A. Pál, J. E. Rodriguez, and the TESS team. TESS Discovery of a Transiting Super-Earth in the π Mensae System. *ArXiv e-prints*, September 2018.

Alexander Hubbard. Making terrestrial planets: High temperatures, fu orionis outbursts, earth, and planetary system architectures. *The Astrophysical Journal Letters*, 840(1):L5, 2017. URL `http://stacks.iop.org/2041-8205/840/i=1/a=L5`.

I. Hubeny. Vertical structure of accretion disks - A simplified analytical model. , 351:632–641, March 1990. doi: 10.1086/168501.

F James and M Roos. MINUIT: a system for function minimization and analysis of the parameter errors and corrections. *Comput. Phys. Commun.*, 10(CERN-DD-75-20):343–367. 38 p, Jul 1975. URL `https://cds.cern.ch/record/310399`.

Inga Kamp, Stefano Antonellini, Andres Carmona, John Ilee, and Christian Rab. Multi-wavelength observations of planet forming disks: Constraints on planet formation processes. *ArXiv e-prints*, art. arXiv:1712.00303, December 2017.

Kamp, Inga. Modeling and interpretation of line observations*. *EPJ Web of Conferences*, 102:00013, 2015. doi: 10.1051/epjconf/201510200013. URL `https://doi.org/10.1051/epjconf/201510200013`.

S. J. Kenyon and L. Hartmann. Spectral Energy Distributions of T Tauri Stars: Disk Flaring and Limits on Accretion. , 323:714, December 1987. doi: 10.1086/165866.

M. Keppler, M. Benisty, A. Müller, T. Henning, R. van Boekel, F. Cantalloube, C. Ginski, R. G. van Holstein, A.-L. Maire, A. Pohl, M. Samland, H. Avenhaus, J.-L. Baudino, A. Boccaletti, J. de Boer, M. Bonnefoy, G. Chauvin, S. Desidera, M. Langlois, C. Lazzoni, G.-D. Marleau, C. Mordasini, N. Pawellek, T. Stolker, A. Vigan, A. Zurlo, T. Birnstiel, W. Brandner, M. Feldt, M. Flock, J. Girard, R. Gratton, J. Hagelberg, A. Isella, M. Janson, A. Juhasz, J. Kemmer, Q. Kral, A.-M. Lagrange, R. Launhardt, A. Matter, F. Ménard,

J. Milli, P. Mollière, J. Olofsson, L. Pérez, P. Pinilla, C. Pinte, S. P. Quanz, T. Schmidt, S. Udry, Z. Wahhaj, J. P. Williams, E. Buenzli, M. Cudel, C. Dominik, R. Galicher, M. Kasper, J. Lannier, D. Mesa, D. Mouillet, S. Peretti, C. Perrot, G. Salter, E. Sissa, F. Wildi, L. Abe, J. Antichi, J.-C. Augereau, A. Baruffolo, P. Baudoz, A. Bazzon, J.-L. Beuzit, P. Blanchard, S. S. Brems, T. Buey, V. De Caprio, M. Carbillet, M. Carle, E. Cascone, A. Cheetham, R. Claudi, A. Costille, A. Delboulbé, K. Dohlen, D. Fantinel, P. Feautrier, T. Fusco, E. Giro, L. Gluck, C. Gry, N. Hubin, E. Hugot, M. Jaquet, D. Le Mignant, M. Llored, F. Madec, Y. Magnard, P. Martinez, D. Maurel, M. Meyer, O. Möller-Nilsson, T. Moulin, L. Mugnier, A. Origné, A. Pavlov, D. Perret, C. Petit, J. Pragt, P. Puget, P. Rabou, J. Ramos, F. Rigal, S. Rochat, R. Roelfsema, G. Rousset, A. Roux, B. Salasnich, J.-F. Sauvage, A. Sevin, C. Soenke, E. Stadler, M. Suarez, M. Turatto, and L. Weber. Discovery of a planetary-mass companion within the gap of the transition disk around PDS 70. , 617:A44, September 2018. doi: 10.1051/0004-6361/201832957.

W. Kley and R.P. Nelson. Planet-disk interaction and orbital evolution. *Annual Review of Astronomy and Astrophysics*, 50(1):211–249, 2012. doi: 10.1146/annurev-astro-081811-125523. URL `https://doi.org/10.1146/annurev-astro-081811-125523`.

Á. Kóspál, P. Ábrahám, T. Csengeri, O. Fehér, M. R. Hogerheijde, C. Brinch, M. M. Dunham, E. I. Vorobyov, D. M. Salter, and T. Henning. Mass Transport from the Envelope to the Disk of V346 Nor: A Case Study for the Luminosity Problem in an FUor-type Young Eruptive Star. , 843:45, July 2017. doi: 10.3847/1538-4357/aa7683.

C. J. Lada. Star formation: from OB associations to protostars. In *Star Forming Regions*, volume 115, page 1, January 1987.

M. Lecar, M. Podolak, D. Sasselov, and E. Chiang. On the Location of the Snow Line in a Protoplanetary Disk. , 640:1115–1118, April 2006. doi: 10.1086/500287.

J. J. Lissauer, D. Ragozzine, D. C. Fabrycky, J. H. Steffen, E. B. Ford, J. M. Jenkins, A. Shporer, M. J. Holman, J. F. Rowe, E. V. Quintana, N. M. Batalha, W. J. Borucki, S. T. Bryson, D. A. Caldwell, J. A. Carter, D. Ciardi, E. W. Dunham, J. J. Fortney, T. N. Gautier, III, S. B. Howell, D. G. Koch, D. W. Latham, G. W. Marcy, R. C. Morehead, and D. Sasselov. Architecture and Dynamics of Kepler's Candidate Multiple Transiting Planet Systems. , 197:8, November 2011. doi: 10.1088/0067-0049/197/1/8.

H. B. Liu, E. I. Vorobyov, R. Dong, M. M. Dunham, M. Takami, R. Galván-Madrid, J. Hashimoto, Á. Kóspál, T. Henning, M. Tamura, L. F. Rodríguez, N. Hirano, Y. Hasegawa, M. Fukagawa, C. Carrasco-Gonzalez, and M. Tazzari. A concordant scenario to explain FU Orionis from deep centimeter and millimeter interferometric observations. , 602:A19, June 2017. doi: 10.1051/0004-6361/201630263.

Liu, Hauyu Baobab, Vorobyov, Eduard I., Dong, Ruobing, Dunham, Michael M., Takami, Michihiro, GalvÃ¡n-Madrid, Roberto, Hashimoto, Jun, KÃ^3*spl*, *gnes*, $Henning, Thomas, Tamura, Moto$ $A19, 2017. doi : .$ URL `https://doi.org/10.1051/0004-6361/201630263`.

R. Luger, M. Sestovic, E. Kruse, S. L. Grimm, B.-O. Demory, E. Agol, E. Bolmont, D. Fab-

rycky, C. S. Fernandes, V. Van Grootel, A. Burgasser, M. Gillon, J. G. Ingalls, E. Jehin, S. N. Raymond, F. Selsis, A. H. M. J. Triaud, T. Barclay, G. Barentsen, S. B. Howell, L. Delrez, J. de Wit, D. Foreman-Mackey, D. L. Holdsworth, J. Leconte, S. Lederer, M. Turbet, Y. Almleaky, Z. Benkhaldoun, P. Magain, B. M. Morris, K. Heng, and D. Queloz. A seven-planet resonant chain in TRAPPIST-1. *Nature Astronomy*, 1:0129, June 2017. 10.1038/s41550-017-0129.

D. Lynden-Bell and J. E. Pringle. The evolution of viscous discs and the origin of the nebular variables. , 168:603–637, September 1974. 10.1093/mnras/168.3.603.

B. A. MacFarlane and D. Stamatellos. The structure of young embedded protostellar discs. , 472:3775–3788, December 2017. 10.1093/mnras/stx1973.

J. G. Mangum and Y. L. Shirley. How to Calculate Molecular Column Density. , 127:266, March 2015. 10.1086/680323.

M. Min, C. P. Dullemond, M. Kama, and C. Dominik. The thermal structure and the location of the snow line in the protosolar nebula: Axisymmetric models with full 3-D radiative transfer. , 212:416–426, March 2011. 10.1016/j.icarus.2010.12.002.

A. Miotello, M. Kama, and E. van Dishoeck. Disk mass determination through CO isotopologues. *IAU General Assembly*, 22:2245531, August 2015.

A. Miotello, E. F. van Dishoeck, M. Kama, and S. Bruderer. Determining protoplanetary disk gas masses from CO isotopologues line observations. , 594:A85, October 2016. 10.1051/0004-6361/201628159.

A. Miotello, E. F. van Dishoeck, J. P. Williams, M. Ansdell, G. Guidi, M. Hogerheijde, C. F. Manara, M. Tazzari, L. Testi, N. van der Marel, and S. van Terwisga. Lupus disks with faint CO isotopologues: low gas/dust or high carbon depletion? , 599:A113, March 2017. 10.1051/0004-6361/201629556.

T. Molyarova, V. Akimkin, D. Semenov, P. Ábrahám, T. Henning, Á. Kóspál, E. Vorobyov, and D. Wiebe. Chemical Signatures of the FU Ori Outbursts. , 866:46, October 2018. 10.3847/1538-4357/aadfd9.

Satoshi Okuzumi, Munetake Momose, Sin-iti Sirono, Hiroshi Kobayashi, and Hidekazu Tanaka. Sintering-induced Dust Ring Formation in Protoplanetary Disks: Application to the HL Tau Disk. , 821, April 2016. 10.3847/0004-637X/821/2/82.

C. H. Peñaloza, P. C. Clark, S. C. O. Glover, R. Shetty, and R. S. Klessen. Using CO line ratios to trace the physical properties of molecular clouds. , 465:2277–2285, February 2017. 10.1093/mnras/stw2892.

S. Perez, S. Casassus, F. Ménard, P. Roman, G. van der Plas, L. Cieza, C. Pinte, V. Christiaens, and A. S. Hales. CO Gas Inside the Protoplanetary Disk Cavity in HD 142527: Disk Structure from ALMA. , 798:85, January 2015a. 10.1088/0004-637X/798/2/85.

S. Perez, A. Dunhill, S. Casassus, P. Roman, J. Szulágyi, C. Flores, S. Marino, and M. Mon-

tesinos. Planet Formation Signposts: Observability of Circumplanetary Disks via Gas Kinematics. , 811:L5, September 2015b. 10.1088/2041-8205/811/1/L5.

S. Pérez, S. Casassus, and P. Benítez-Llambay. Observability of planet-disc interactions in CO kinematics. , 480:L12–L17, October 2018a. 10.1093/mnrasl/sly109.

Sebastián Pérez, S. Casassus, and P. Benítez- Llambay. Observability of planet-disc interactions in CO kinematics. , page L113, June 2018b. 10.1093/mnrasl/sly109.

C. Pinte, F. Ménard, G. Duchêne, T. Hill, W. R. F. Dent, P. Woitke, S. Maret, G. van der Plas, A. Hales, I. Kamp, W. F. Thi, I. de Gregorio-Monsalvo, C. Rab, S. P. Quanz, H. Avenhaus, A. Carmona, and S. Casassus. Direct mapping of the temperature and velocity gradients in discs. Imaging the vertical CO snow line around IM Lupi. , 609:A47, January 2018a. 10.1051/0004-6361/201731377.

C. Pinte, D. J. Price, F. Ménard, G. Duchêne, W. R. F. Dent, T. Hill, I. de Gregorio-Monsalvo, A. Hales, and D. Mentiplay. Kinematic Evidence for an Embedded Protoplanet in a Circumstellar Disk. , 860:L13, June 2018b. 10.3847/2041-8213/aac6dc.

J. E. Pringle. Accretion discs in astrophysics. *Annual Review of Astronomy and Astrophysics*, 19(1):137–160, 1981. 10.1146/annurev.aa.19.090181.001033. URL `https://doi.org/10.1146/annurev.aa.19.090181.001033`.

Z. Regály and E. Vorobyov. The circumstellar disk response to the motion of the host star. , 601:A24, May 2017. 10.1051/0004-6361/201629154.

Z. Regály, A. Juhász, Z. Sándor, and C. P. Dullemond. Possible planet-forming regions on submillimetre images. , 419:1701–1712, January 2012. 10.1111/j.1365-2966.2011.19834.x.

Z. Regály, S. Király, and L. L. Kiss. Asymmetric Fundamental Band CO Lines as a Sign of an Embedded Giant Planet. , 785:L31, April 2014. 10.1088/2041-8205/785/2/L31.

G. R. Ricker, J. N. Winn, R. Vanderspek, D. W. Latham, G. Á. Bakos, J. L. Bean, Z. K. Berta-Thompson, T. M. Brown, L. Buchhave, N. R. Butler, R. P. Butler, W. J. Chaplin, D. Charbonneau, J. Christensen-Dalsgaard, M. Clampin, D. Deming, J. Doty, N. De Lee, C. Dressing, E. W. Dunham, M. Endl, F. Fressin, J. Ge, T. Henning, M. J. Holman, A. W. Howard, S. Ida, J. M. Jenkins, G. Jernigan, J. A. Johnson, L. Kaltenegger, N. Kawai, H. Kjeldsen, G. Laughlin, A. M. Levine, D. Lin, J. J. Lissauer, P. MacQueen, G. Marcy, P. R. McCullough, T. D. Morton, N. Narita, M. Paegert, E. Palle, F. Pepe, J. Pepper, A. Quirrenbach, S. A. Rinehart, D. Sasselov, B. Sato, S. Seager, A. Sozzetti, K. G. Stassun, P. Sullivan, A. Szentgyorgyi, G. Torres, S. Udry, and J. Villasenor. Transiting Exoplanet Survey Satellite (TESS). *Journal of Astronomical Telescopes, Instruments, and Systems*, 1 (1):014003, January 2015. 10.1117/1.JATIS.1.1.014003.

G. P. Rosotti, C. J. Clarke, C. F. Manara, and S. Facchini. Constraining protoplanetary disc evolution using accretion rate and disc mass measurements: the usefulness of the dimensionless accretion parameter. , 468:1631–1638, June 2017. 10.1093/mnras/stx595.

K. R. Schwarz, E. A. Bergin, L. I. Cleeves, G. A. Blake, K. Zhang, K. I. Öberg, E. F. van

Dishoeck, and C. Qi. The Radial Distribution of H_2 and CO in TW Hya as Revealed by Resolved ALMA Observations of CO Isotopologues. , 823:91, June 2016. 10.3847/0004-637X/823/2/91.

N. I. Shakura and R. A. Sunyaev. Black holes in binary systems. Observational appearance. , 24:337–355, 1973a.

N. I. Shakura and R. A. Sunyaev. Black holes in binary systems. Observational appearance. , 24:337–355, 1973b.

Patrick D. Sheehan and Josh A. Eisner. Multiple Gaps in the Disk of the Class I Protostar GY 91. , 857:18, April 2018. 10.3847/1538-4357/aaae65.

Karen M. Strom and Stephen E. Strom. The Discovery of Two FU Orionis Objects in L1641. , 412:L63, August 1993. 10.1086/186941.

R. Teague, D. Semenov, U. Gorti, S. Guilloteau, T. Henning, T. Birnstiel, A. Dutrey, R. van Boekel, and E. Chapillon. A Surface Density Perturbation in the TW Hydrae Disk at 95 au Traced by Molecular Emission. , 835:228, February 2017. 10.3847/1538-4357/835/2/228.

Richard Teague, Jaehan Bae, Edwin A. Bergin, Tilman Birnstiel, and Daniel Foreman-Mackey. A Kinematical Detection of Two Embedded Jupiter-mass Planets in HD 163296. , 860:L12, June 2018. 10.3847/2041-8213/aac6d7.

StÃ©phane Udry and Nuno C. Santos. Statistical properties of exoplanets. *Annual Review of Astronomy and Astrophysics*, 45(1):397–439, 2007. 10.1146/annurev.astro.45.051806.110529. URL `https://doi.org/10.1146/annurev.astro.45.051806.110529`.

J. P. Williams and W. M. J. Best. A Parametric Modeling Approach to Measuring the Gas Masses of Circumstellar Disks. , 788:59, June 2014. 10.1088/0004-637X/788/1/59.

J. P. Williams and C. McPartland. Measuring Protoplanetary Disk Gas Surface Density Profiles with ALMA. , 830:32, October 2016. 10.3847/0004-637X/830/1/32.

Jonathan P. Williams and Lucas A. Cieza. Protoplanetary disks and their evolution. *Annual Review of Astronomy and Astrophysics*, 49(1):67–117, 2011. 10.1146/annurev-astro-081710-102548. URL `https://doi.org/10.1146/annurev-astro-081710-102548`.

Joshua N. Winn and Daniel C. Fabrycky. The occurrence and architecture of exoplanetary systems. *Annual Review of Astronomy and Astrophysics*, 53(1):409–447, 2015. 10.1146/annurev-astro-082214-122246. URL `https://doi.org/10.1146/annurev-astro-082214-122246`.

M. C. Wyatt, O. Panić, G. M. Kennedy, and L. Matrà. Five steps in the evolution from protoplanetary to debris disk. , 357:103, June 2015. 10.1007/s10509-015-2315-6.

M. Yu, K. Willacy, S. E. Dodson-Robinson, N. J. Turner, and N. J. Evans, II. Probing Planet Forming Zones with Rare CO Isotopologues. , 822:53, May 2016. 10.3847/0004-637X/822/1/53.

Z. Zhu, L. Hartmann, and C. Gammie. Nonsteady Accretion in Protostars. , 694:1045–1055, April 2009. 10.1088/0004-637X/694/2/1045.